REFERENCE COPY

[redacted]

UNCLASSIFIED

NATIONAL AERONAUTICS AND SPACE ADMINISTRATION

Space Programs Summary No. 37-41, Volume II

for the period July 1, 1966 to August 31, 1966

The Planetary–Interplanetary Program

(Title Unclassified)

LAB-C02117

Classification Changed to
UNCLASSIFIED
Letter from W. E. Hansen, Manager
Authority
GPI-Sec. & Plt Prot. Section, to NASA
11-4-1966 Date
By
Jan. 6, 1972 A. Castanier

471

Copy No.

JET PROPULSION LABORATORY
CALIFORNIA INSTITUTE OF TECHNOLOGY
PASADENA, CALIFORNIA

September 30, 1966

JET PROPULSION LABORATORY
LIBRARY
JAN 13 1967
CALIFORNIA INSTITUTE OF TECHNOLOGY

149975

[redacted]

GROUP [redacted] year intervals;
declassified after

UNCLASSIFIED

UNCLASSIFIED

Preface

The *Space Programs Summary* is a six-volume, bimonthly publication that documents the current project activities and supporting research and advanced development efforts conducted or managed by JPL for the NASA space exploration programs. The titles of all volumes of the *Space Programs Summary* are:

Vol. I. The Lunar Program (Confidential)

Vol. II. The Planetary–Interplanetary Program (Confidential)

Vol. III. The Deep Space Network (Unclassified)

Vol. IV. Supporting Research and Advanced Development (Unclassified)

Vol. V. Supporting Research and Advanced Development (Confidential)

Vol. VI. Space Exploration Programs and Space Sciences (Unclassified)

The *Space Programs Summary,* Vol. VI consists of an unclassified digest of appropriate material from Vols. I, II, and III; an original presentation of technical supporting activities, including engineering development of environmental-test facilities, and quality assurance and reliability; and a reprint of the space science instrumentation studies of Vols. I and II.

Approved by:

W. H. Pickering, *Director*
Jet Propulsion Laboratory

Space Programs Summary No. 37-41, Volume II

Copyright © 1966, Jet Propulsion Laboratory, California Institute of Technology

Prepared under Contract No. NAS 7-100, National Aeronautics & Space Administration

This document contains information affecting the national defense of the United States, within the meaning of the Espionage Laws, Title 18, U.S.C., Sections 793 and 794, the transmission or revelation of which in any manner to an unauthorized person is prohibited by law.

UNCLASSIFIED

UNCLASSIFIED

Contents

I. *Mariner* 1967 Project 1

A. Introduction 1

B. Systems 3

C. Engineering Mechanics 3

D. Guidance and Control 15

E. Space Sciences 22

F. Propulsion 27

II. *Mariner* Mars 1969 Project 31

A. Introduction 31

B. Project Engineering 32

C. Systems 39

D. Engineering Mechanics 40

E. Guidance and Control 50

References 51

III. *Voyager* Project 53

A. Introduction 53

B. Guidance and Control 54

C. Telecommunications 67

D. Propulsion 74

Reference 85

IV. Future Projects 86

A. Introduction 86

B. Science Planning for a Venus/Mercury Swingby Mission 86

References 91

UNCLASSIFIED

UNCLASSIFIED

I. *Mariner* 1967 Project

A. Introduction

The *Mariner* 1967 Project continues and extends the work of the previous *Mariner* Projects. Two elements of the Project are concerned with the *Mariner IV* spacecraft now in space, while a third is concerned with the Venus flyby mission in 1967.

1. Mariner Mars 1964 Project

Residual activity of the *Mariner* Mars 1964 Project consists primarily of continuing analysis of tracking data, publication of results by the principal investigators, and preparation of final reports. However, periodic detection, recording, and commanding activities involving the *Mariner IV* spacecraft have been assigned to the Deep Space Network (DSN). Using elements of the experimental facilities at Goldstone Station and advanced R&D techniques, attempts are being made to communicate with the spacecraft. Results are published in *SPS*, Vol. III.

2. Mariner IV Project

In the second half of 1967, *Mariner IV* will again be within the normal communication range of the DSN stations. At that time an attempt will be made to obtain additional telemetry data from *Mariner IV*. The *Mariner IV* Project comprises the preparation, support, and actual reacquisition of the spacecraft.

The objectives, authorized in December 1965, simultaneously with those for the Venus flight, have been established as follows:

> *The primary objective of the Mariner IV Project is to obtain scientific information on the interplanetary environment in a region of space further from the Sun than the orbit of Earth during a period of increasing solar activity in 1967, using the Mariner IV spacecraft still operating in orbit around the Sun.*
>
> *The secondary objectives are to obtain additional engineering knowledge about the consequences of*

UNCLASSIFIED

UNCLASSIFIED

extended exposure of spacecraft equipment in the interplanetary space environment and to acquire experience in the operation of a planetary spacecraft after a prolonged lifetime in deep space.

Flight operations on this project (providing that a functioning spacecraft allows this to occur) will overlap the *Mariner* Venus 67 Project flight activities.

3. Mariner Venus 67 Project

The major task of the *Mariner* 1967 Project is the Venus flyby mission, named the *Mariner* Venus 67 Project. The following mission objectives have been established:

The primary objective of the Mariner Venus 67 Project is to conduct a flyby mission to Venus in 1967 in order to obtain scientific information which will complement and extend the results obtained by Mariner II relevant to determining the origin and nature of Venus and its environment.

Secondary objectives are to acquire engineering experience in converting and operating a spacecraft designed for flight to Mars into one flown to Venus, and to obtain information on the interplanetary environment during a period of increasing solar activity.

With the authorizing of this project late in December of 1965, and the launch opportunity occurring in June 1967, the period available to the *Mariner* Venus 67 Project for planning, design, test, and other flight preparation is 18 mo. Because of this minimum length of time, application, to the fullest extent possible, must be made of techniques developed from the experience of prior missions, and existing hardware must be utilized.

The single flight spacecraft, designated M67-2, is currently being prepared by converting the spare spacecraft (MC-4) that was built for the *Mariner* Mars 1964 Project.[1] An *Atlas-Agena D* launch vehicle will inject the spacecraft into a 120-day transit trajectory. The launch readiness date has been set at June 10, 1967, with a 14-day launch period starting June 12. Ranging provisions have been authorized for this mission which will offer the possibility of considerably enhancing the celestial mechanics experiment. At encounter, an unusually sharp perturbation will occur.

[1]Portions of the proof test model (PTM) spacecraft and spares from the MM64 Project are also being prepared as a flight-support spacecraft (M67-1); there will be no PTM as such. The flight-support spacecraft will serve the double function of pseudo-PTM and backup spacecraft for qualifying spare subsystems.

Seven scientific experiments have been approved for the *Mariner* Venus 67 mission:

Experiment	*Principal investigator*
S-Band radio occultation	Arvydas J. Kliore, Jet Propulsion Laboratory
Ultraviolet photometer	Charles A. Barth, University of Colorado
Dual-frequency radio propagation	Von R. Eshleman, Stanford University
Helium magnetometer	Edward J. Smith, Jet Propulsion Laboratory
Solar plasma	Herbert S. Bridge, Massachusetts Institute of Technology
Trapped radiation	James A. Van Allen, State University of Iowa
Celestial mechanics	John D. Anderson, Jet Propulsion Laboratory

The first experiment requires the use of only the RF transmission subsystem on the spacecraft, and the last one utilizes only the tracking doppler data derived from the RF carrier. Of the remaining five experiments, four are to be accomplished with the existing instrumentation, with only minor modifications. Only the dual-frequency radio propagation experiment of Stanford requires the incorporation of a new scientific instrument into the payload.

Other changes to the basic spacecraft design are necessitated by the fact that the spacecraft will travel toward, rather than away from, the Sun and also because conversions must be made to accommodate revised encounter sequencing and science payload. In particular, modifications are needed in the following areas:

(1) Scientific data automation system

(2) Antenna pattern and orientation

(3) Thermal control

(4) Solar panel configuration

(5) Planetary sensors

UNCLASSIFIED

UNCLASSIFIED

As a result of exceptional performance by the DSN in extracting the telemetry from the *Mariner IV* signal, the NASA Particles and Fields Subcommittee has requested that additional telemetry data be regularly obtained for the purpose of comparison with other missions now in progress (e.g., *Pioneer VI* and *VII*). All of the telemetry data thus far reduced indicate that the spacecraft is performing as well as it was during the last acquisition phase in 1965.

The July–August reporting period essentially ended the spacecraft detail design phase, and emphasis is now shifting toward the actual testing and validation of the design.

Because launch pad 12, rather than launch pad 13, more closely provides the environment to meet the design criteria previously established, it has been designated as the pad to be used for the launch of *Mariner* Venus 67.

NASA headquarters has concurred with the JPL recommendation that the planetary quarantine constraint be no smaller than 5×10^{-4}. This figure was derived from the parametric analysis concerning the actual probability of contaminating the planet by impacting it with the vehicle or spacecraft, and by the ejecta from the spacecraft.

B. Systems

1. Systems-Test-Complex Data System

A computer-based systems-test-complex data system (STCDS) will be used in the analysis of the system test data from all *Mariner* Venus 67 system tests (*SPS 37-40*, Vol. II, p. 4). The STCDS will acquire telemetry data, all stimuli and response information relating to both spacecraft and operational support equipment (OSE), analog data such as power supply voltages, test facility ambient operating conditions, etc., and frequency data. All acquired data will be recorded, processed according to data type, and separated into categories suitable for display to specialists in the design and performance analysis of the various spacecraft subsystems.

The leased Control Data Corporation 3300 computer system, part of which is shown in Fig. 1, and some elements of the data display subsystem were delivered to JPL July 5, 1966. The computer system passed the required 30-day acceptance test August 19, and is now in use for program development and checkout of the data input subsystem (DIS) modules that are being provided by Astrodata, Inc.

The telemetry input module, the DIS controller module, and the cable interface units were delivered to JPL August 8, and these units are being integrated with the computer system (a block diagram is shown in *SPS 37-40*, Vol. II, p. 3). The junction-box module is now available for connecting input signals from the OSE to the DIS module circuits required for proper monitoring of the spacecraft signals.

The technical requirements and cost of the analog data acquisition module are now fully defined, and procurement action has started. Also, procurement of a second telemetry input module is being initiated to provide for the processing of two simultaneous telemetry data streams (derived from M67-1 and M67-2 spacecraft) by January 1967. Progress in development of the programming system and in hardware checkout and integration indicates that the milestone date of October 1, 1966 for telemetry data processing should be achieved.

C. Engineering Mechanics

1. Introduction

During the reporting period, the structural qualification tests on the structural test model (STM) have been successfully completed. The STM was subjected to torsional, lateral, and axial axes of vibrational excitation.

A modal vibration test was conducted on a dummy weighted solar panel structure. The experimentally determined mode shapes agreed reasonably well with the panel properties predicted by the analysis.

The temperature control model simulator test results are given. Various test modes were run at both Earth and Venus intensities. Results indicate that the thermal design of the spacecraft is adequate and that there is sufficient margin to cover any nonstandard operating modes during flight.

New upper and lower thermal blankets, redesigned because of the changes to the spacecraft configuration,

UNCLASSIFIED

UNCLASSIFIED

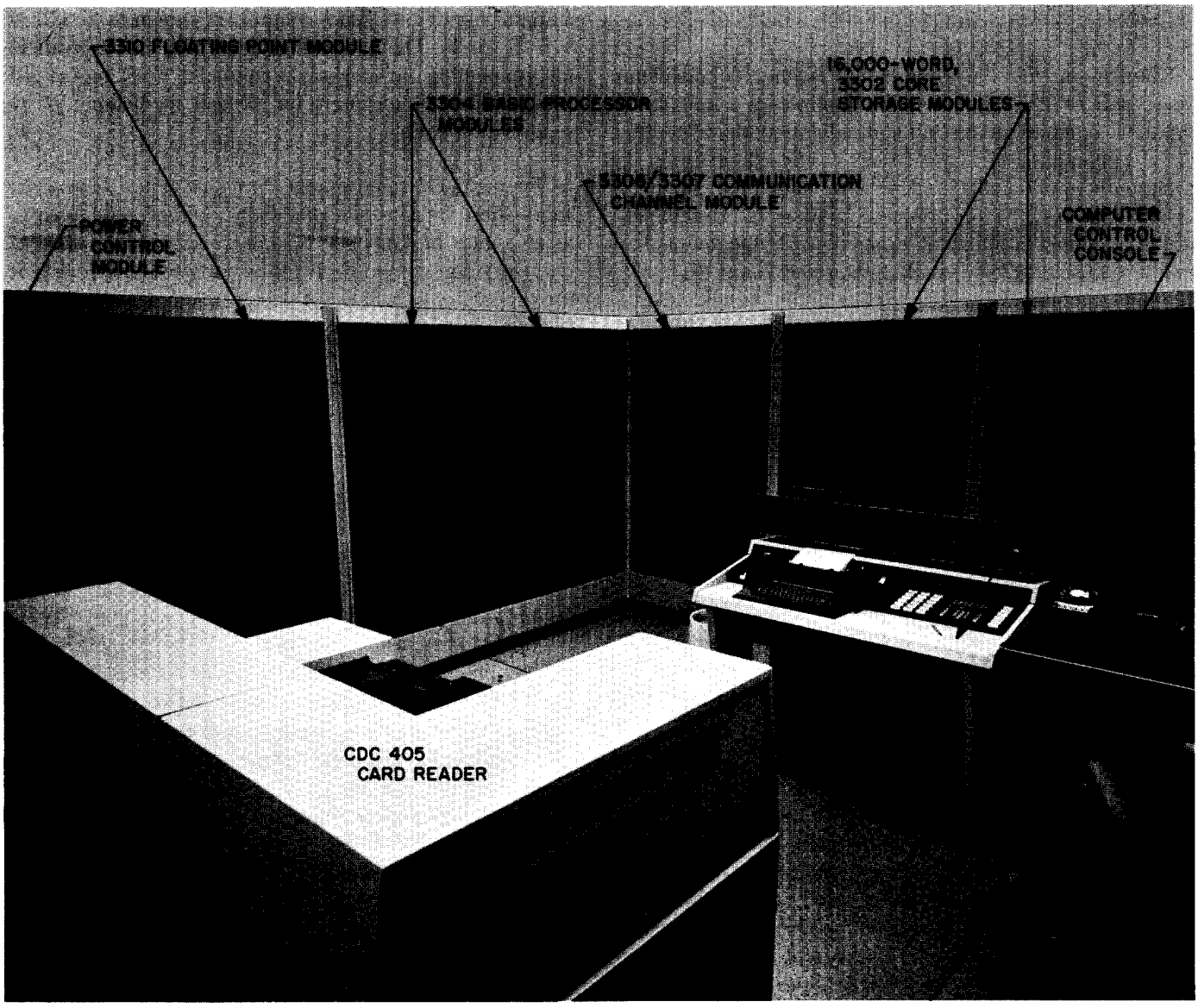

Fig. 1. Portion of CDC 3300 computer system

UNCLASSIFIED

UNCLASSIFIED

have been fabricated. The blanket fabrication techniques are the same as for *Mariner* Mars 1964.

A deployable Sun shade, mounted on the sunny side of the spacecraft, has been designed. During the boost phase it is retracted to clear the adapter and the interface hardware. At solar panel deployment it is released to shade the peripheral items on the spacecraft bus.

Ten of the *Mariner* Mars 1964 batteries have been reworked to salvage the battery chassis for use on *Mariner* Venus 67.

2. Structures and Dynamics

a. Structural and environmental vibration qualification test. The spacecraft composite vibration test of the *Mariner* Venus 67 structural test model has been completed. The STM successfully withstood design ultimate load and structural qualification dynamic loads defined in JPL specifications MVB-50587-TST and MVP-50602-TST. The full 3-wk period allocated was required for completion of the test. The STM underwent forced vibration excitation during the test program for a total of 3 hr, 28 min.

Low-frequency structural developmental and design ultimate load tests were conducted for torsional, lateral, and axial axes of excitation with a test structure containing four uncelled solar panels. Typical test setups for these axes, respectively, are illustrated by Figs. 2–4. Qualification level tests were performed to qualify one celled solar panel at the system level for low frequency and complex wave excitation along axial and lateral axes. Additional low-level runs were made to determine the dynamic response characteristics of the propulsion subsystem for fuel pressure/configurations along its most critical axis of response. For this portion of the test, the STM contained four uncelled solar panels.

Two modifications were made on the solar panel tip dampers during the testing program. The initial damper test hardware was found to have the incorrect dynamic properties. Improved damping characteristics were brought about by changing the size of the sealing O-rings and changing the viscosity of the damping fluid. Qualification and design ultimate load level testing was performed, without failure, with the modified hardware for torsional and x-axis excitation. During x-axis excitation, at design ultimate load level, large dynamic excursions of the dampers at 8 cps resulted in boundary contact between the end of the damper piston and the damper housing. Although the dynamic loads associated with this shock-type acceleration were not deleterious to the structure, the dampers were removed from the test structure and mechanically adjusted to provide for larger dynamic displacements. The boundary contact, which occurred only at design ultimate load level in lateral axes of excitation, was greatly reduced during the remainder of the test.

Three pieces of hardware were repaired during the testing program. The attitude control jet sun shade support brackets in Bays 1 and 7 were repaired for spot-weld failures. One lexan tube fitting on the high-gain antenna feed support structure developed a crack during design ultimate load level testing in the z-axis. After completion of the STM test, and prior to use of the STM as a test fixture for the solar panel system level qualification test, the fitting was preloaded in the hoop direction by using a wire wrapping that was potted with epoxy. A small hole was drilled at the apex of the crack to present a potential stress concentration. The crack appeared not to propagate during the remainder of the test program.

Table 1. Summary of modal test data and comparison with analysis

Analysis frequency, cps	Test frequency, cps	Damping ratio c/c_c from test	Comment
22.4	26.7	0.0048	In-plane mode; neither leg sliding in test
30.8	30.6	0.0045	Symmetric beam bending
39.1	40.6	0.0032	Antisymmetric beam bending
69.3	70 ± 2	>0.05	In-plane mode; impossible to excite due to high damping
87.0	80.9	0.008	Coupled beam and corrugation
94.8	73.9	0.0024	Symmetric corrugation mode analysis EI, 20% high

b. Modal test of single solar panel. The modal tests verified the solar panel properties, predicted by analysis to a reasonable degree, as shown in Table 1. The discrepancies that exist are at least partially explained by known differences between test parts and the analytic model. In addition to verification, the test measured values (also listed in Table 1) of the damping ratios at small amplitudes which are used in later analysis. The quality of the test is indicated by the degree to which the test mass matrix is diagonal, as shown in Table 2. The analytic mass matrix is also given, based on only those masses whose motion was measured in the test and, as can be seen, the discrepancy from a unit matrix is of the same order as the error of the test mass matrix.

UNCLASSIFIED

UNCLASSIFIED

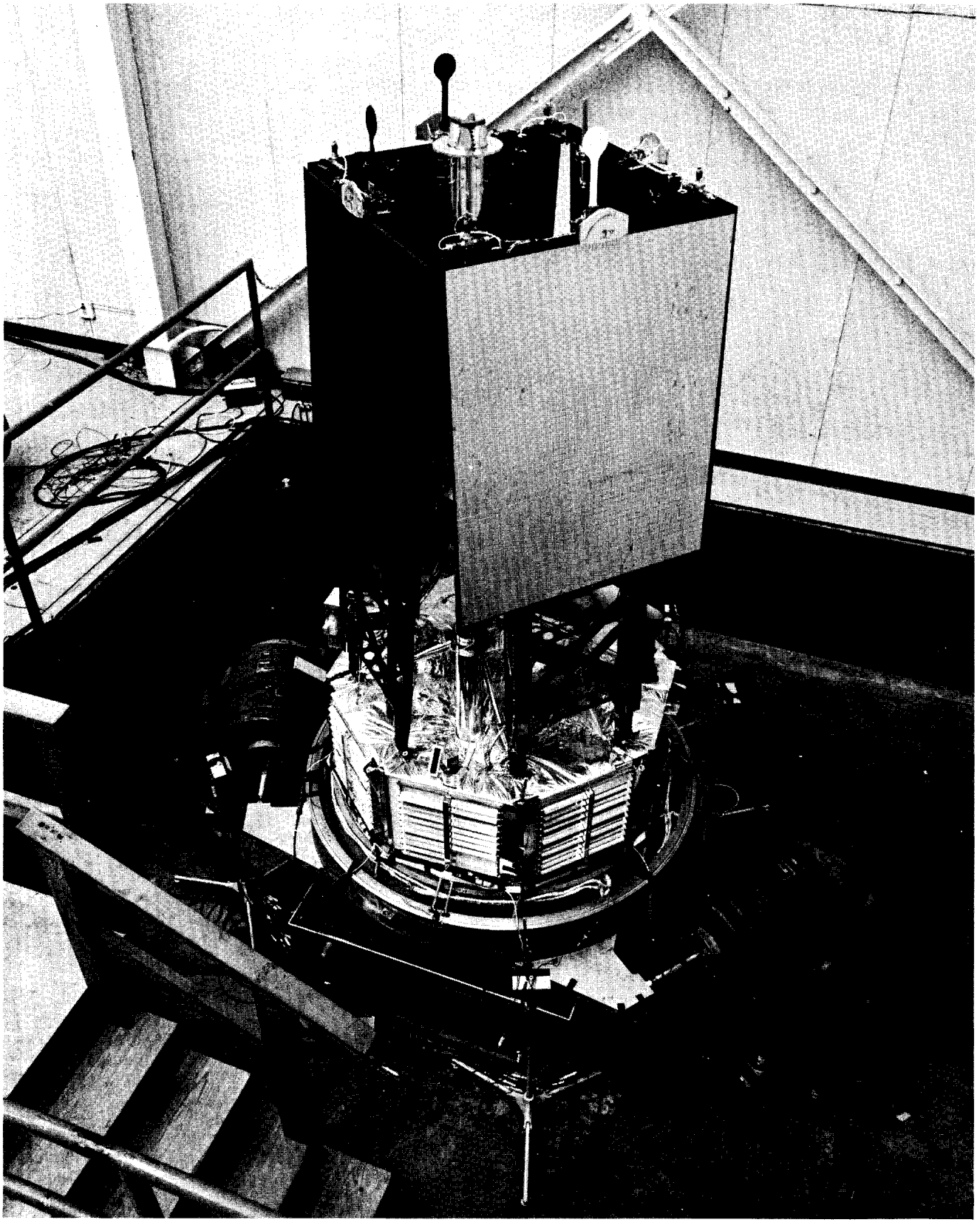

Fig. 2. STM torsional vibration test setup

UNCLASSIFIED

UNCLASSIFIED

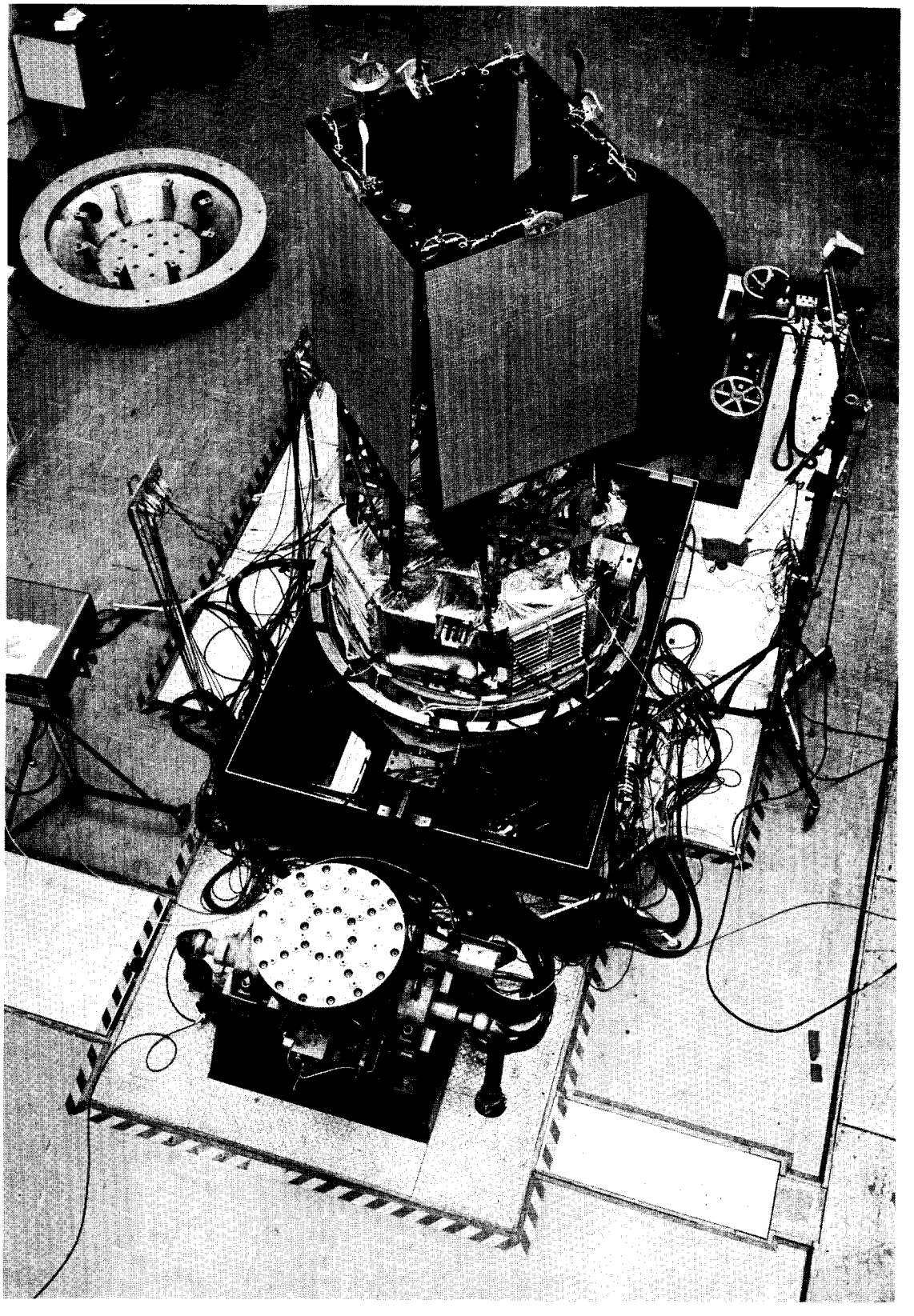

Fig. 3. STM lateral axis vibration test setup

UNCLASSIFIED

UNCLASSIFIED

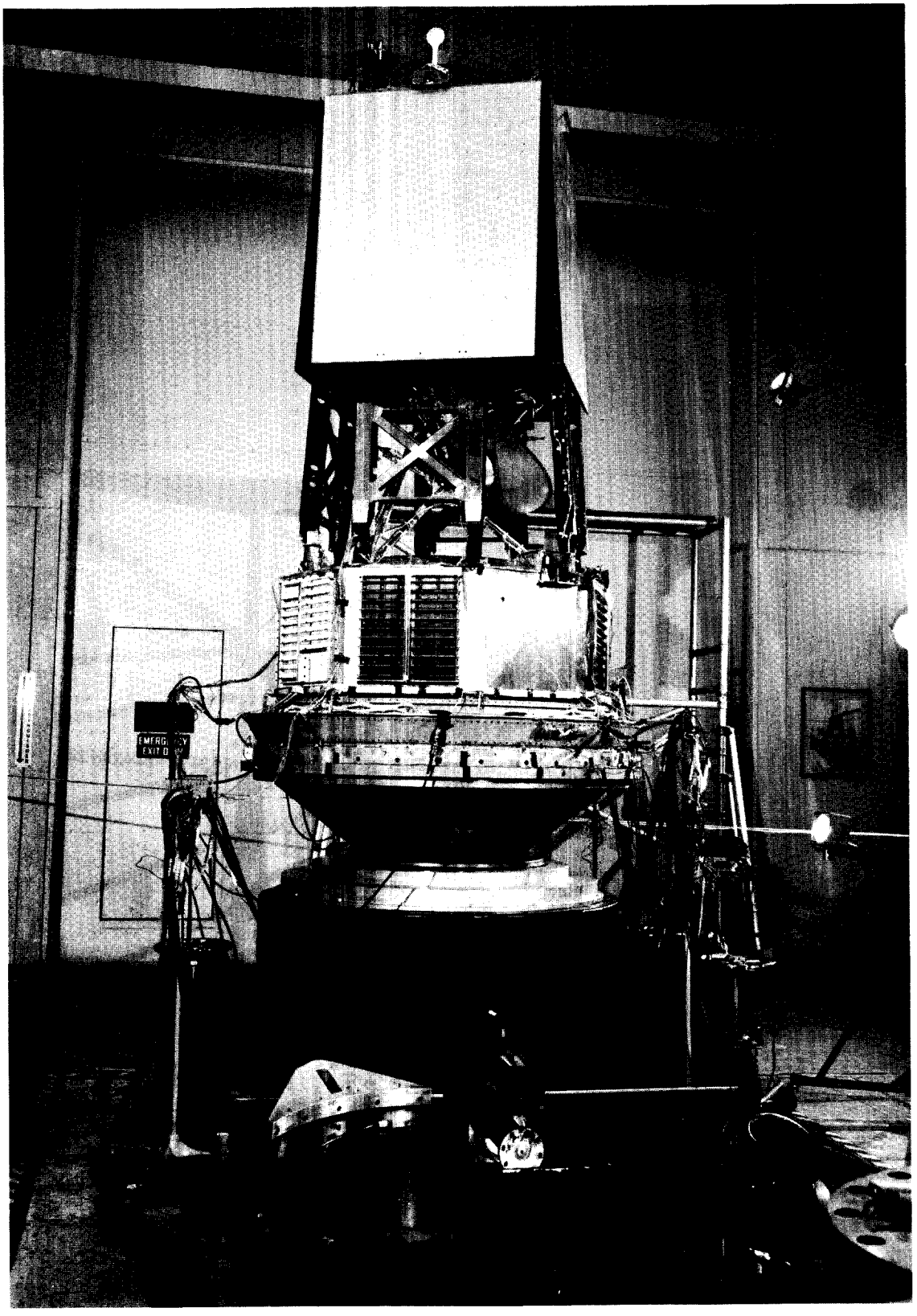

Fig. 4. STM axial axis vibration test setup

UNCLASSIFIED

UNCLASSIFIED

Table 2. Mass matrix

	Test						Analysis					
Test	1.0	0.07	−0.08		0.07	0.01	0.96	0.11	0.07	−0.05	0.11	0.06
	0.07	1.0	0.04		0.08	0.08	−0.07	0.98	0.11	0.05	−0.04	−0.01
	−0.08	0.04	1.0		0.08	0.02	−0.03	0.14	−0.94	0.04	−0.01	−0.03
	0.07	0.08	0.08		1.0	0.18	0.03	−0.02	−0.14	−0.08	−0.71	0.16
	0.01	0.08	0.02		0.18	1.0	−0.03	0.08	0.03	0.01	−0.15	0.91
Analysis	0.96	−0.07	−0.03		0.03	−0.03	0.97	−0.01	0.01	0.02	0.10	0.05
	0.11	0.98	0.14		−0.02	0.08	−0.01	1.00	0.00	0.01	0.00	0.00
	0.07	0.11	−0.94		−0.14	0.03	0.01	0.00	1.00	0.02	−0.01	−0.00
	−0.05	0.05	0.04		−0.08	0.01	0.02	0.01	0.02	0.80	−0.08	−0.04
	0.11	−0.04	−0.01		−0.71	−0.15	0.10	0.00	−0.01	−0.08	0.96	−0.02
	0.06	−0.01	−0.03		0.16	0.91	0.05	0.00	−0.00	−0.04	−0.02	0.99

Another measure of the comparison of the test to analysis is the degree to which the test analytic coupling partition of the mass matrix approaches a unit matrix, as can be seen in Table 2 (negative values on the diagonal only imply negative normalization). The decoupling exhibited by the analytic fourth mode and the test modes is an excellent indication of the existence of a highly damped mode that was impossible to excite with two shakers during the modal test (the test setup is illustrated in Fig. 5).

Fig. 5. Solar panel modal test setup

c. Static test of single solar panel. Static tests verified the location of the shear center of the panel and the torsional stiffness. The in-plane test stiffness was high compared to analysis, as it should be, since both beams were prevented from in-plane sliding in the test setup.

3. Temperature Control

a. Solar panel cutouts. The radiant flux falling on an electronic bay face from the corresponding solar panel is directly proportional to the bay-to-panel form factor and to the solar intensity. For *Mariner* Venus 67 the solar intensity at encounter is approximately twice the maximum *Mariner* Mars 1964 level, and the irradiation of the bay face would have scaled up proportionately, had the 1964 panel design been retained. The removal of side shielding to cool the bay would have aggravated the problem by exposing more area to the variable radiation from the panels. In order to reduce the bay face-to-panel form factor, the celled area of the solar panel was cut back from the bus. The effect of such a cutback is shown in Fig. 6. With the present solar panel design, the irradiation of the near-bay from each solar panel is only approximately 4 w/ft^2 at encounter.

b. Power profile. A comparison of the power levels and distributions of *Mariner* Mars 1964 and *Mariner* Venus 67 is given in Table 3 for typical flight modes. *Mariner* Venus 67 has the advantage of a higher power level and more power on the "cold side" (Bay 2 side) of the bus. The decision to leave cruise science on during playback also alleviates the uneven power distribution problems.

UNCLASSIFIED

UNCLASSIFIED

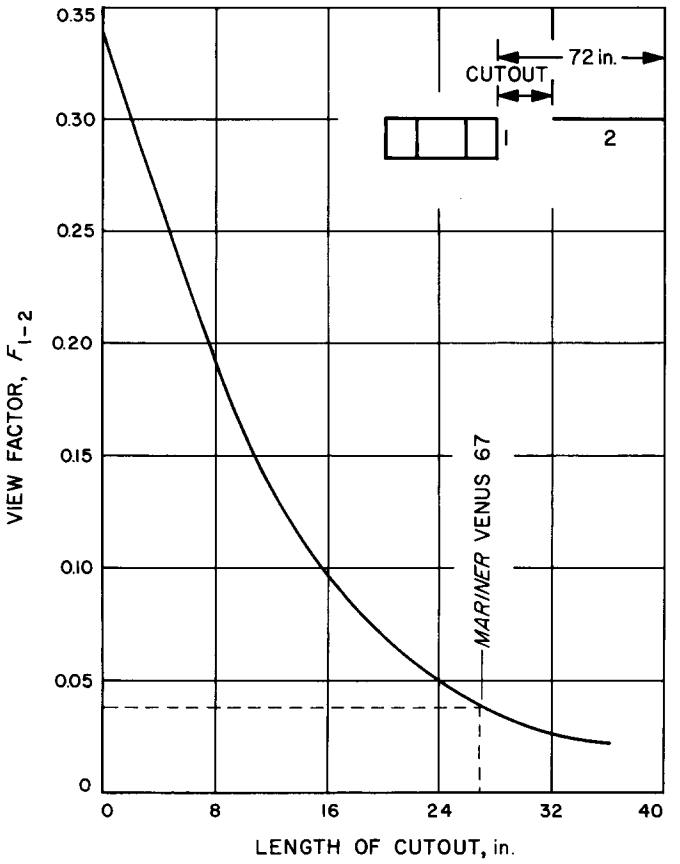

Fig. 6. View factor, bay face to solar panel

c. Temperature control model (TCM): test results. The TCM tests were conducted in the JPL 10-ft Space Simulator from June 24 to July 6, 1966. Table 4 is a summary of the test results for the bus. *Mariner IV* flight data and allowable temperature ranges are shown for comparison. The *Mariner* Venus 67 TCM and *Mariner IV* data are for different modes of internal power dissipation, but provide a "mean operating temperature" comparison.

Preflight temperature predictions for both *Mariner II* and *IV* were incorrect, because of solar heating test inputs which differed from flight. For the Venus probe, this error was nearly disastrous. For *Mariner* Venus 67 every effort has been made to minimize this input and to understand its effects. During the TCM testing, two modes were run in which the solar simulator lights were turned off and the TCM heater power was increased to reproduce the temperature profiles for the Earth cruise mode and the gyros on encounter mode (TCM Test II, Modes 7 and 6). The difference in internal power with the lights off is equivalent to the solar heating input. Excluding the conductive input from the sun sensors and the radiative input from solar panels, the solar input at Earth was found to be 18.5 w and at Venus 36 w. These inputs are small compared to the 150–250-w bus internal power dissipation and should produce correspondingly small test errors.

Table 3. Bus power dissipation, w

Mariner Venus 67 TCM			
Case	Earth cruise (cavity amplifier, battery charger off)	Venus cruise (TWT, battery charger on)	Encounter (gyros on, battery charger off)
I	21.7	35.7	31.9
II	0	0	0
III	22.9	22.9	22.9
IV	12.8	12.8	12.8
V	7.7	7.7	13.6
VI	38.0	66.4	66.4
VII	9.3	9.3	36.9
VIII	41.0	41.0	69.1
Total	153.4	195.8	253.6
Mariner Mars 1964 Estimate			
Case	Earth cruise (cavity amplifier, battery charger on)	Mars cruise (TWT, battery charger off)	Playback (TWT, battery charger off)
I	32.2	18.2	14.8
II	0	0	0
III	12.3	12.3	0
IV	10.9	10.9	10.9
V	7.5	7.5	11.6
VI	38.0	66.4	66.4
VII	9.6	9.6	9.6
VIII	30.0	30.0	30.0
Total	140.5	154.7	143.3

Assumed power dissipation for DAS was 12.5 w.

With no solar input and the spacecraft's lowest cruise mode power, the midcourse propellant tank had just dropped to freezing (TCM Test II, Mode 8). A solar intensity increase from 250 to 286 w/ft² caused only a 1.3°F average increase in bus temperature at Venus (TCM Test I, Modes 2 and 3). An extrapolation to perihelion has not yet been performed, but bus survival does not appear to be a problem.

The thermal effects of a Sun shade failure were investigated in TCM Test III. The shade was completely stowed, and Earth cruise and encounter modes were run. Analysis of the test data indicates that the bus absorbs an incremental 150 w at Venus with the shade stowed. This heat input raised the bus temperature 32.5°F at encounter and

UNCLASSIFIED

UNCLASSIFIED

UNCLASSIFIED

Table 4. TCM test results summary, °F

Mariner IV					TCM Test I			TCM Test II									TCM Test III	
Bay	Earth cruise (cavity, battery charger on)	Mars cruise (TWT, battery charger off)	Playback (TWT, battery charger off)	Temperature limits	Mode 1 Earth cruise (cavity, battery charger off)	Mode 2, gyros on encounter	Mode 3, gyros on encounter at 286 w/ft^2	Mode 1 cruise (TWT, battery charger on)	Mode 2 cruise, no panel power	Mode 3, parametric	Mode 4 Venus cruise, 120% power	Mode 5, louvers open	Mode 6, encounter temperature match	Mode 7 Earth cruise, temperature match	Mode 8 Earth cruise, lights off	Mode 9 Earth cruise, 80% power	Mode 1 Earth cruise, shade stowed	Mode 2, gyros on encounter, shade stowed
I	76	60	54	14 to 167	64.4	80.4	81.8	77.4	75.2	77.8	80.8	104.0	80.4	63.6	53.2	47.4	75.0	111.8
II	72	41	33	35 to 125	48.0	64.5	67.5	62.5	61.0	63.5	65.5	89.5	63.5	46.0	32.0	30.5	74.0	119.0
III	70	51	34	14 to 122	63.8	74.8	75.6	74.8	73.0	75.2	75.4	97.2	75.8	63.0	45.4	41.2	75.2	103.8
IV	72	54	47	14 to 167	60.6	77.8	79.4	74.4	72.6	76.2	78.2	105.4	78.2	60.2	41.4	37.4	77.6	114.8
V	66	60	60	14 to 149	56.4	73.8	74.0	71.0	70.6	72.0	72.0	91.6	74.6	55.4	38.2	35.2	67.6	99.0
VI	71	70	69	14 to 167	64.4	86.0	86.8	83.0	82.2	84.0	88.8	110.4	86.0	63.4	47.8	41.8	72.4	110.0
VII	64	58	57	30 to 131	57.6	77.4	79.0	65.2	63.8	65.0	65.8	87.8	77.4	56.8	44.4	40.6	63.2	106.4
VIII	88[a]	81[a]	77[a]	14 to 167	67.5	85.3	86.5	73.8	72.3	72.5	76.3	99.5	84.8	66.5	63.0	57.5	72.0	115.8
Average	72.4	59.4	53.9		60.3	77.5	78.8	72.8	71.3	73.3	75.4	98.2	77.6	59.4	45.7	41.5	72.1	110.1

[a]Estimate, by correlation with battery temperature.

UNCLASSIFIED

UNCLASSIFIED

caused an undesirably high, but probably tolerable, temperature level.

Since flight spacecraft undergo thermal testing in the space simulator prior to flight, there is little cause to expect errors due to large internal power changes in flight. However, *Mariner* Venus 67 is thermally a power-dependent spacecraft, so this parameter is of interest in design studies and in evaluating the effect of simulator error sources. For these reasons, tests were performed in which internal power was reduced 20% at Earth and increased 20% at Venus (TCM Test II, Modes 9 and 4). The power variation produced a negligible effect for the Venus power-up case, but brought the midcourse propellant near freezing for the Earth power-down mode. Thus, the power margin at the cold end is approximately 30 w. The hot-end margin was deduced by a "louvers open" mode in which internal power was increased to force all louvers open and drive temperatures near the upper limits (TCM Test II, Mode 5). The power increment above the gyros on encounter level was approximately 125 w. The spacecraft is operating near its lower power limit in order to provide margin for midcourse heating and to provide more nearly optimum operating levels for the various subsystems. The timely upgrading of the solar simulator to produce a Venus Sun for this test, combined with the demonstrated thermal margins, satisfied most of the test objectives which were to have been met in a second TCM test in August, which was therefore cancelled. A short radiometer calibration test has been scheduled to resolve a 15% discrepancy in the readings of the two test radiometers at Venus intensity. The resolution of this anomaly is significant but not crucial to the use and interpretation of test data.

d. Temperature control hardware

Shields. The *Mariner* upper and lower shield blanket configuration has been modified for consistency with the

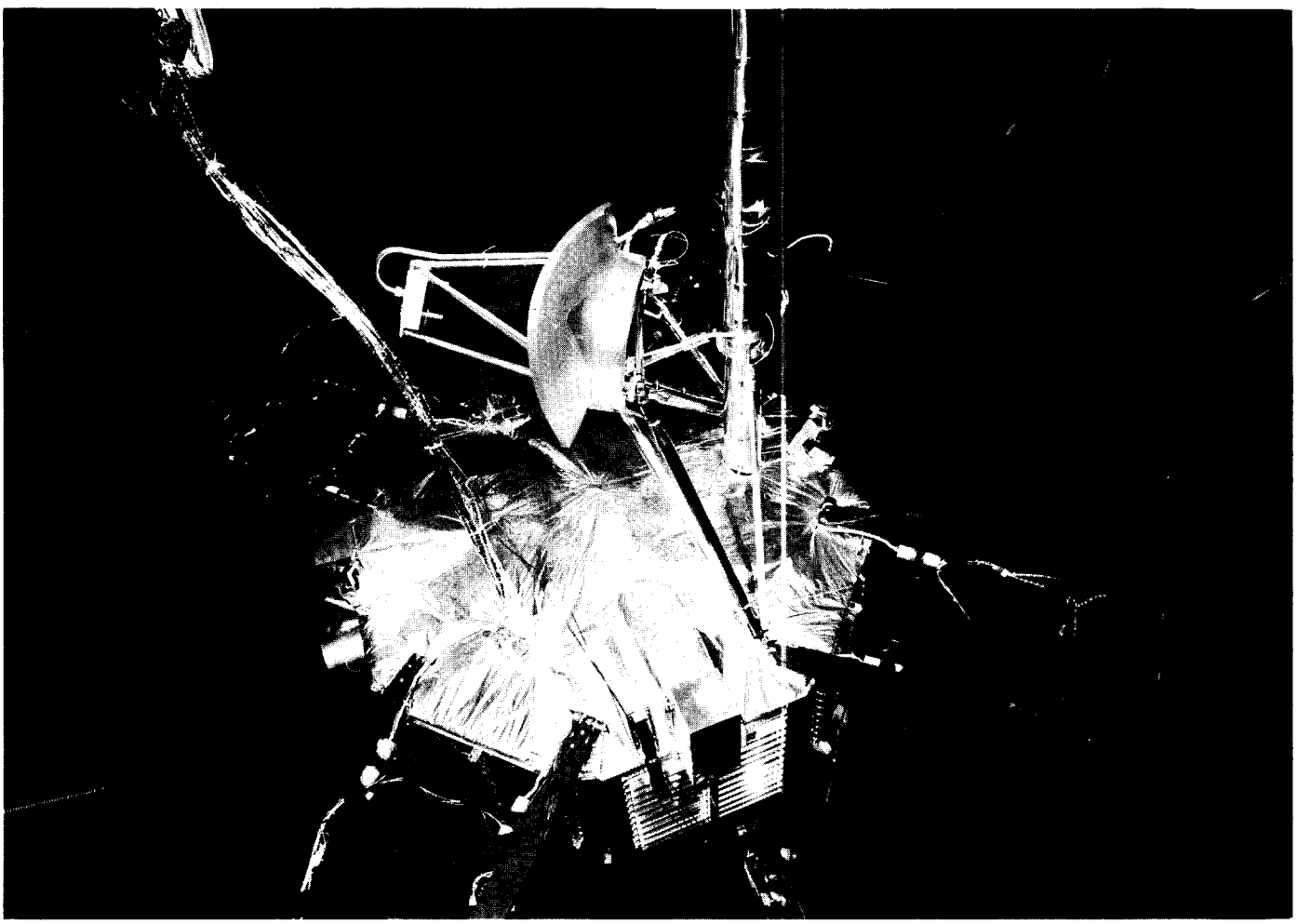

Fig. 7. Upper (shady side) thermal shield blanket

UNCLASSIFIED

UNCLASSIFIED

Mariner Venus 67 design (Figs. 7 and 8). However, the construction and attachment to the spacecraft are similar to *Mariner* Mars 1964. The *Mariner* Venus 67 multilayer super insulation blankets are fabricated from predimpled 0.0005-in.-thick Mylar; *Mariner* Mars 1964 used hand-crinkled 0.00025-in.-thick Mylar. The new blanket material is expected to have a lower effective thermal conductivity because of the retention of thickness in known thermally-shorted areas on the spacecraft.

Although the material is twice as thick as that used on *Mariner* Mars 1964, only half as many layers are used, thus no weight increase and improved venting capabilities are realized. This new type of construction has been successfully demonstrated on the recently completed *Mariner* Venus 67 TCM and STM tests.

The polished aluminum peripheral shields will be used as they were on *Mariner* Mars 1964, with the exception of a small shield below the louvers on Bays 3, 5, 7, and 8, which will be omitted.

Two additional shield designs for *Mariner* Venus 67 are the attitude control jet shield and the trapped radiation detector shield. These shields consist of sheet metal support structures and small multilayer blankets attached to the sunny side of the support structures. The attitude control jet shields located on the tips of all four solar panels are similar in design to the Sun shades used on two of the panels on *Mariner* Mars 1964.

Deployable Sun shade. The Sun shade design and concept is new to the *Mariner* Venus 67 temperature control

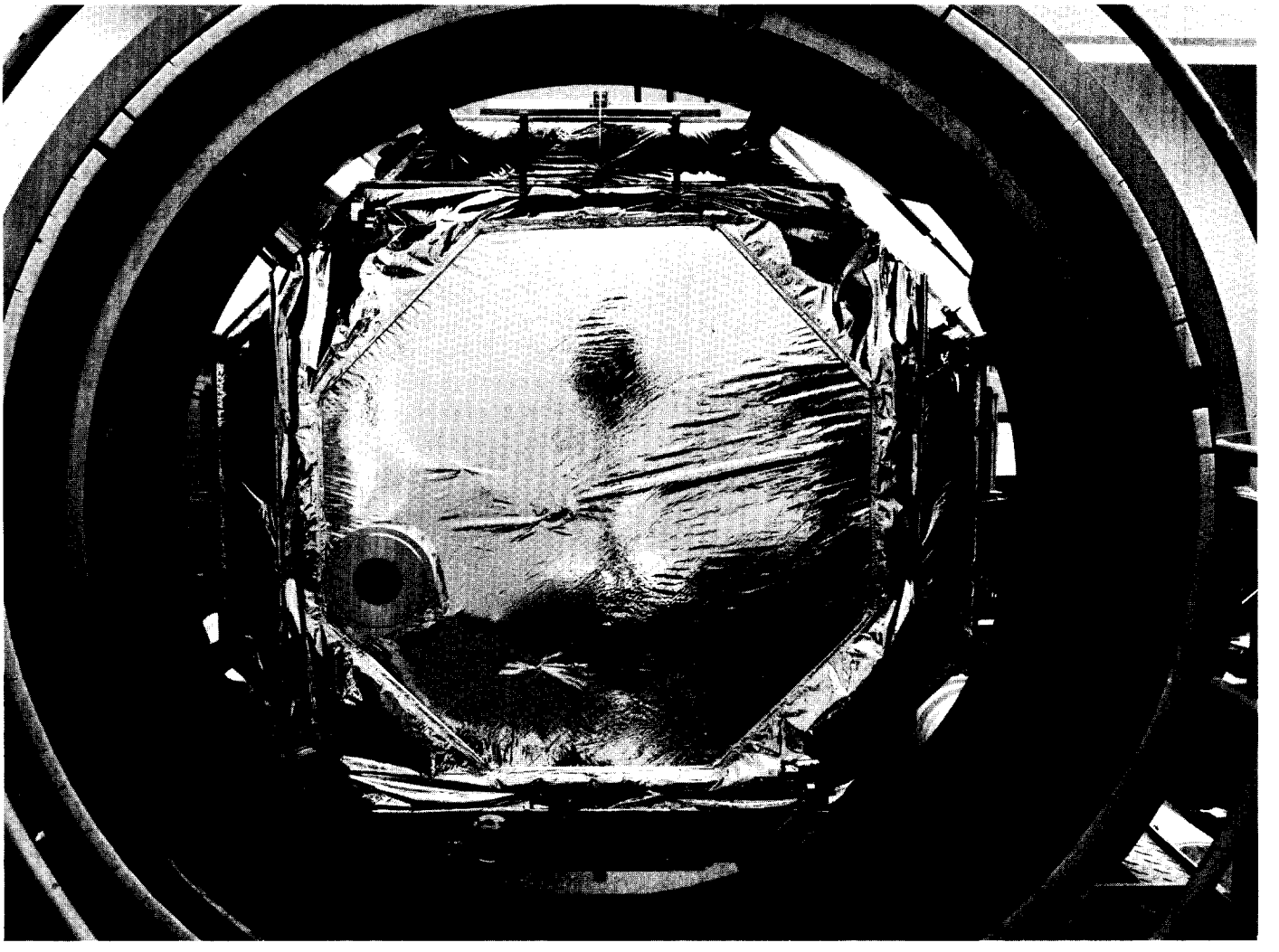

Fig. 8. Lower (sunny side) thermal shield blanket

UNCLASSIFIED

UNCLASSIFIED

subsystem. It is designed to reduce the solar input to the bus by protecting peripheral hardware on the spacecraft from direct sunlight. The shade material is a single sheet of 1-mil Teflon aluminized on one side, with the Teflon side toward the Sun.

During the boost phase it is retracted (Fig. 9) to clear the *Agena* adapter and spacecraft interface hardware. When deployed, the shade forms an octagonal-shaped awning, approximately 10 in. wide, about the periphery of the spacecraft on the sunlit side (Fig. 10).

The deployment and support of the shade is performed by eight spiral-wound spring assemblies located in pairs on Bays 1, 3, 5, and 7. A dacron lanyard is attached to a rod between the pairs of springs, and in turn through a series of eyelets to the solar panel in that bay. Each of these four sections of the shade is deployed independently by the solar panel deployment in that bay. The direct tie between the shade and the panel results in the shade deploying at the same rate as the solar panel. The shade is fully deployed when the panel has reached approximately 75% of its travel. The shade reaches its fully deployed position when the material becomes tight, as limited by a dacron cord sewed in the periphery of the shade.

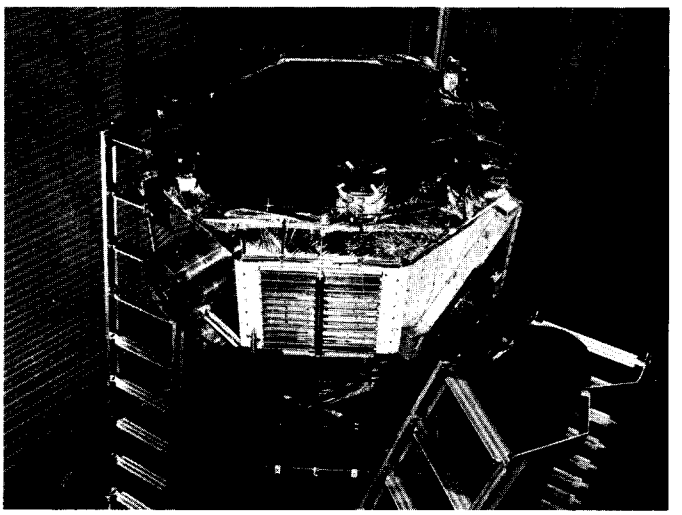

Fig. 9. Deployable Sun shade in stowed position

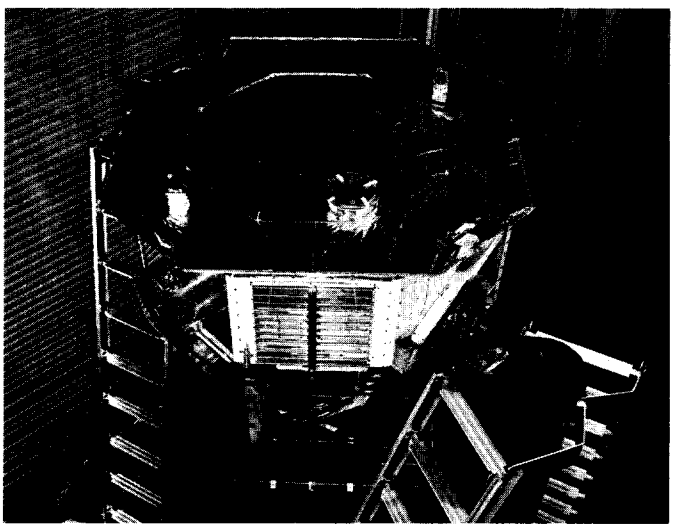

Fig. 10. Deployable Sun shade in deployed position

The shade has completed thermal TA testing on the TCM in the deployed and stowed positions. In each case the shade was subjected to Venus solar intensity (250 w/ft^2). After the simulator test, the shade and associated hardware were checked for solar degradation. Other than an expected discoloration of the white dacron tie cord no other effects of solar irradiation were noted. Particular attention was given to deployment after solar exposure in the stowed position. A possible problem of material fusion hindering deployment or operation did not exist.

The shade has completed structural TA level tests on the *Mariner* Venus 67 STM spacecraft. The possibility of a partial predeployment while on the *Agena* adapter was a major concern. This type of failure which might have been caused by deployment mechanism damage or stowing technique did not occur. A complete inspection of the shade after the test revealed no structural damage. The shade was then deployed on all four bays simultaneously at a rate of approximately 20 deg/sec. Full deployment was achieved in 8 sec and the shade was again inspected for damage and correct configuration. Although a successful shade deployment test was conducted on the STM

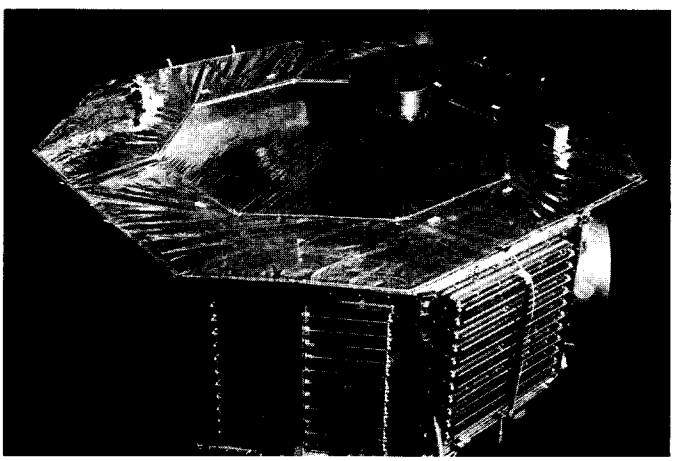

Fig. 11. Deployable Sun shade after successful deployment on STM

UNCLASSIFIED

UNCLASSIFIED

(Fig. 11), a further design effort is being made on a more reliable mechanical retainer for the shade "shirt tail" in Bays 2, 4, 6, and 8 while in the stowed position.

Thus far the deployable Sun shade has achieved the thermal control and structural vibration design objectives. Further development efforts planned include: shade deployment, sensor stray light interference, RF pattern, solar panel deployment (effect of additional energy from shade), interface, failure modes (predeployment on adapter), handling and installation problems.

4. Electronic Packaging

a. Battery chassis rework. At the outset of the *Mariner* Venus 67 Program a study was made to determine what hardware used on *Mariner* Mars 1964 could be used on *Mariner* Venus 67.

One such long lead item with no change from *Mariner* Mars 1964 was the billets for the battery chassis and cover. Eleven batteries were required for *Mariner* Venus 67. Ten old *Mariner* Mars 1964 batteries were available. Previous attempts to salvage battery chassis had been unsuccessful; the silver content was saved, however.

To reduce costs and meet the schedule, reworking the *Mariner* Mars 1964 batteries was proposed. After careful consideration of the expected problems, it was concluded that there was a good chance for success.

The following sequence was used when reworking the battery. Each battery assembly was discharged at not more than 15 amp. Cell terminals were made available through a breakout box, care being taken not to reverse any cell. Each cell was shorted when its voltage became 0.3 v or below.

The batteries contain potassium hydroxide (KOH) solution, a very caustic material, so a handling and rework fixture was made for safety purposes.

The removal of the cells was a heating and machining process. The first step was to remove all cover screws and place the battery on the fixture. Then the battery was heated in a calibrated oven for 3.5 hr at 265°F ±5°F. The bond strength of Epon 815, used to secure the cells to the chassis and cover is reduced at 265°F. The cover was then pried open and removed.

The second step, removal of the cells from the chassis, was the critical phase of the operation. After the battery had cooled to room temperature, a ¼-in. end mill with a 1.5-in. cutting depth was used to remove the Epon 815 which was holding the sides of the cells to the chassis. The battery was again placed on the fixture with cells facing down so that any KOH would be trapped by a steel pan on the fixture. The unit was placed in an oven and heated for a second time at 265°F ±5°F for 4 hr to reduce the strength of the adhesive. The cells were then removed with no damage to the chassis.

The removal of all excess epoxy was accomplished by heating the cover and chassis to 350°F and scraping off all remaining Epon 815.

This procedure proved satisfactory, allowing salvage of the chassis and covers without sacrificing recovery of silver from the cells.

D. Guidance and Control

1. Gyro Control Assembly

The gyro control assembly (GCA) for the *Mariner* Venus 67 Project will be one of the two existing flight spare units from the *Mariner* Mars 1964 Project. No modifications were necessary in the design of this unit since system constraints applicable to the GCA were not changed and only the replacement of out-of-spec components or those now considered unreliable would necessitate any changes. Extensive testing has shown that no components are out of spec, and those which no longer are considered preferred parts have been reviewed and waived due to their inaccessibility and the noncritical effect of their failure modes. The most serious component problem was with a HA 7694 transistor, six of which exist in the hardware. Significant reduction of beta and increase of leakage current in these components would not cause serious system problems since three are used in the forward path of a feedback amplifier and all are used in the forward path of a closed-loop gyro servo. Approval was received June 6, 1966 from the *Mariner* Venus 67 Project Office to leave this component in the unit.

Testing to date on the GCA is nearly complete, with approximately 8 hr of tests remaining. Comparison of today's data with 1964 data shows remarkable gyro stability and no significant change in any area of the GCA tested.

UNCLASSIFIED

UNCLASSIFIED

a. Capacitor leakage. The capacitors of interest here are the twelve 1020 μf integrating capacitors used to derive angular information from the closed-loop high-gain gyros.

Parameter	Previous test	Present test	Test value	Spec allowable value	Agreement
Leakage current	September 17, 1964	June 8, 1966	All less than 5 μa	10 μa_{max}	All capacitors agree within ± 2 μa of previous values

b. Gyro reaction torque (compensated). The gyro reaction torque drift is the g-insensitive drift of the gyro which, in a zero-g field, represents the nominal rate drift of the device.

Gyro	July 23, 1964 drift	July 19, 1966 drift	Allowable drift
Pitch	-0.046 deg/hr	-0.129 deg/hr	± 0.200 deg/hr
Yaw	$+0.012$	$+0.047$	± 0.200
Roll	-0.006	-0.068	± 0.200

c. Forward loop amplifier gain. The loop amplifier gain is the total gain of the AC amplifier, demodulator, and DC amplifier employed in the gyro loop closure electronics.

Amplifier	September 17, 1964 gain	June 15, 1966 gain	Specified gain
Pitch	632	632	600 ± 50
Yaw	632	634	600 ± 50
Roll	610	614	600 ± 50

d. Incremental roll angle. The incremental roll angle is the ground-commanded angle about the roll axis through which the GCA commands the spacecraft during a roll search maneuver. This is a back-up mode for the automatic roll search Canopus acquisition maneuver. The driving element is either one of two roll one-shot monostable multivibrators which command the roll gyro torquer current on for a fixed length of time in either the positive or negative direction.

Direction	August 1964 angular step	July 1966 angular step
Positive command current	2.21 deg	2.25 deg
Negative command current	2.32	2.37

e. Position scale factor. The GCA position scale factor represents the over-all gain of the system while in the position mode. It is used to indicate to the spacecraft attitude control system the amount of angular motion that has occurred as the result of a maneuver or outside force while under inertial control. Variations in this value are the result of variations in the gyros, capacitors, and electronics combined.

Axis	July 1964 scale factor	July 1966 scale factor
Pitch	5.99 v/deg	6.66 v/deg
Yaw	6.68	6.11
Roll	5.57	5.94

f. Commanded turn rates. The commanded turn rate is a fixed rate value which is set before launch and which the GCA commands to the spacecraft for a determined length of time to accomplish an angular maneuver.

The variation in the present data from the 1964 data shows an average reduction of 1.0 deg/hr out of a nominal 648 deg/hr.

g. Demagnetization. An additional constraint on the *Mariner* Venus 67 gyro control assembly was the desire to demagnetize it to reduce its interaction with the on-board magnetometers, since determination of the Venus magnetic fields is one of the primary science requirements. Some reservations exist in the demagnetization of a gyro since these devices contain permanent magnet torquers. Variations in this magnet would affect the gyro torquer scale factor, thus degrading the command rate calibration of the GCA and affecting midcourse maneuver accuracy. On July 20, 1966, the *Mariner* Mars 1964 proof test model GCA was demagnetized to a level of 40, 80, and then 25 gauss. The flight spec is 40 gauss. No significant degradation of gyro performance was noticed as a result

UNCLASSIFIED

UNCLASSIFIED

of this test. It has been determined, then, that the demagnetization of the *Mariner* Venus 67 spacecraft to the level specified will not affect gyro performance.

A voltage heading test requiring approximately 8 hr will be performed, and after its completion the GCA will be delivered to the attitude control group for system integration tests. Following this, it is planned that delivery will be made around September 1, 1966, to the Spacecraft Assembly Facility (SAF) where the GCA will be assembled and tested as a part of the spacecraft.

2. Modifications of Jet Actuator Valves for Reliable Attitude Control at High Temperatures

a. Introduction. After nearly 2 yr of spaceflight operation, the mass-expulsion thrusters of the *Mariner IV* spacecraft are still providing satisfactory attitude control and may continue to function for another year. Torquing moments are obtained with cold nitrogen gas jets at 15 psi manifold pressure as the working fluid. During the forthcoming *Mariner* Venus 67 mission, the solenoid-operated valves are expected to encounter relatively higher temperatures than did *Mariner IV*. In the vicinity of Venus, the jet valve portions of the spacecraft may reach temperatures of 215°F (100°C). Later on, at the orbit path's perihelion or closest approach to the Sun, the temperature may rise to 300°F (150°C). Laboratory tests have indicated marginal operation of the present *Mariner*-type solenoid valves at these temperatures.

To assure reliable performance during the *Mariner* Venus 67 spaceflight, two typical valves manufactured by the Sterer Engineering and Manufacturing Company have been reworked at this Laboratory. Subsequent tests have demonstrated that the modified valves will function satisfactorily with less than half the available current, even at a temperature of 300°F.

b. Mariner thruster valves. The solenoid-operated ball valves and nozzles are flange-mounted on manifolds located at the ends of the solar panels [external configuration and manifold end are shown in Fig. 12(a) and (b)]. A cross-sectional view of the valve with nozzle and manifold is shown in Fig. 13(a) along with a view of one of the disassembled reworked valves [Fig. 13(b)]. A structural drawing of the original thruster is presented in Fig. 14. Modifications that have enabled reliable operation at temperatures up to 300°F are indicated on Fig. 15.

The coil resistance at 70°F room temperature is 305 ±10 Ω. The resistance at 300°F is approximately 160 Ω.

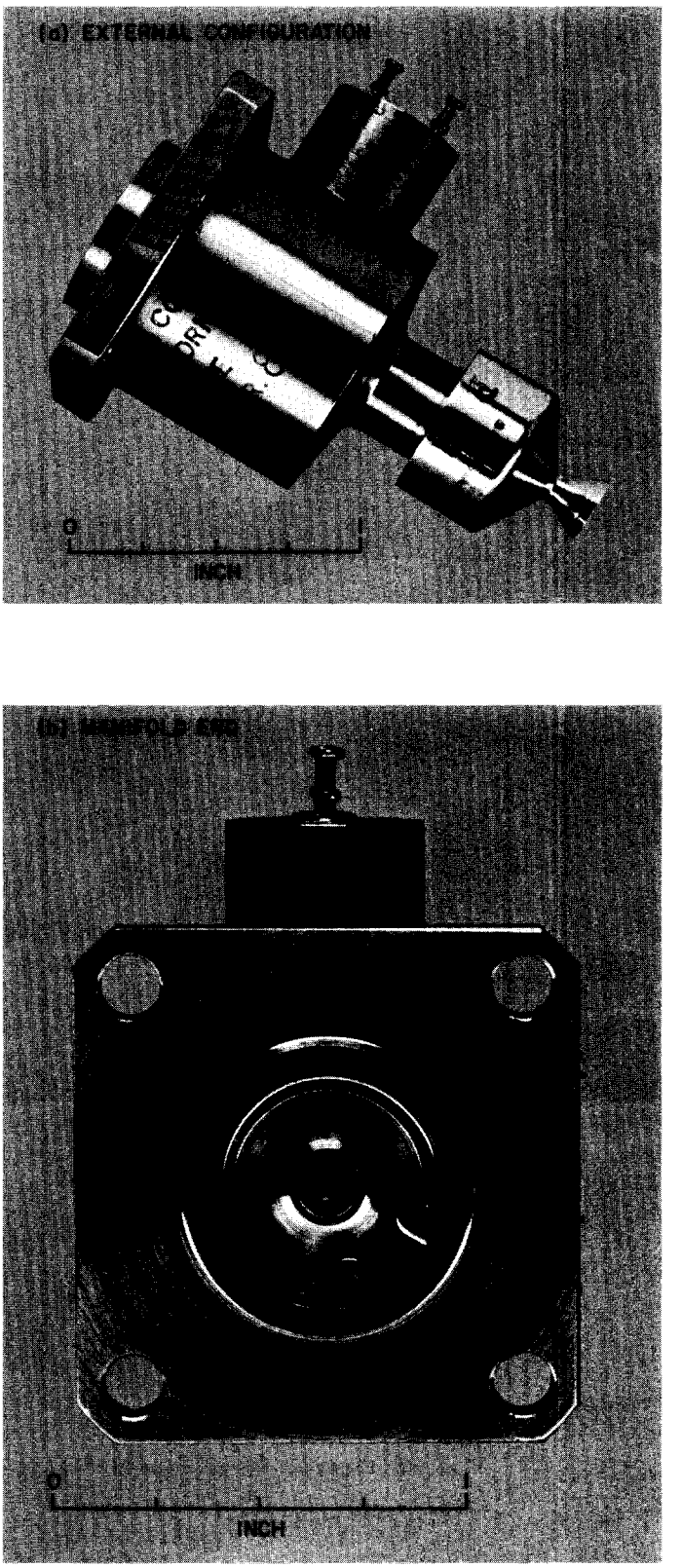

Fig. 12. *Mariner* Mars 1964 and *Mariner* Venus 67 thruster

UNCLASSIFIED

UNCLASSIFIED

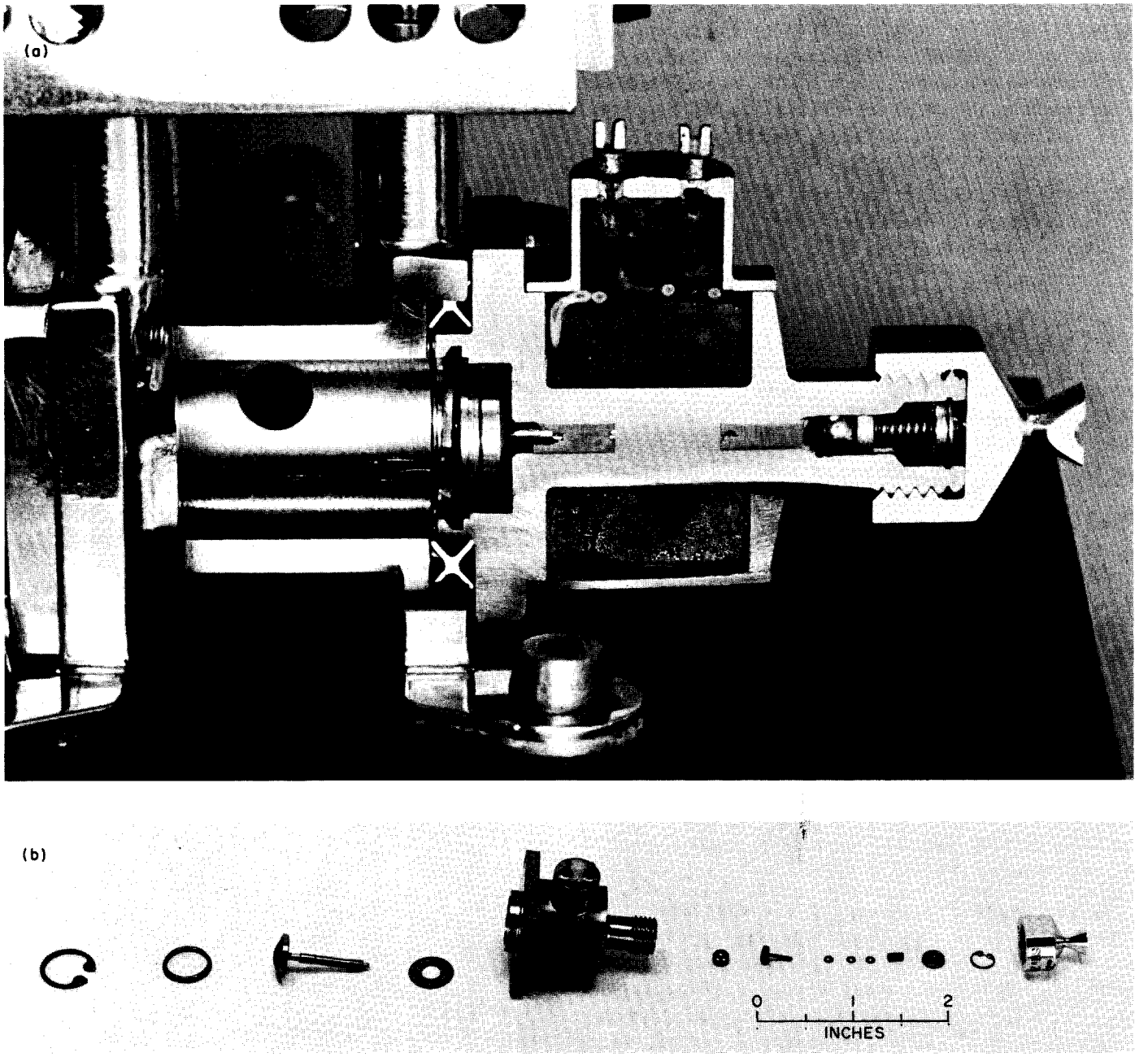

Fig. 13. Cross-sectional view of thruster on manifold, and disassembled components

UNCLASSIFIED

UNCLASSIFIED
CONFIDENTIAL

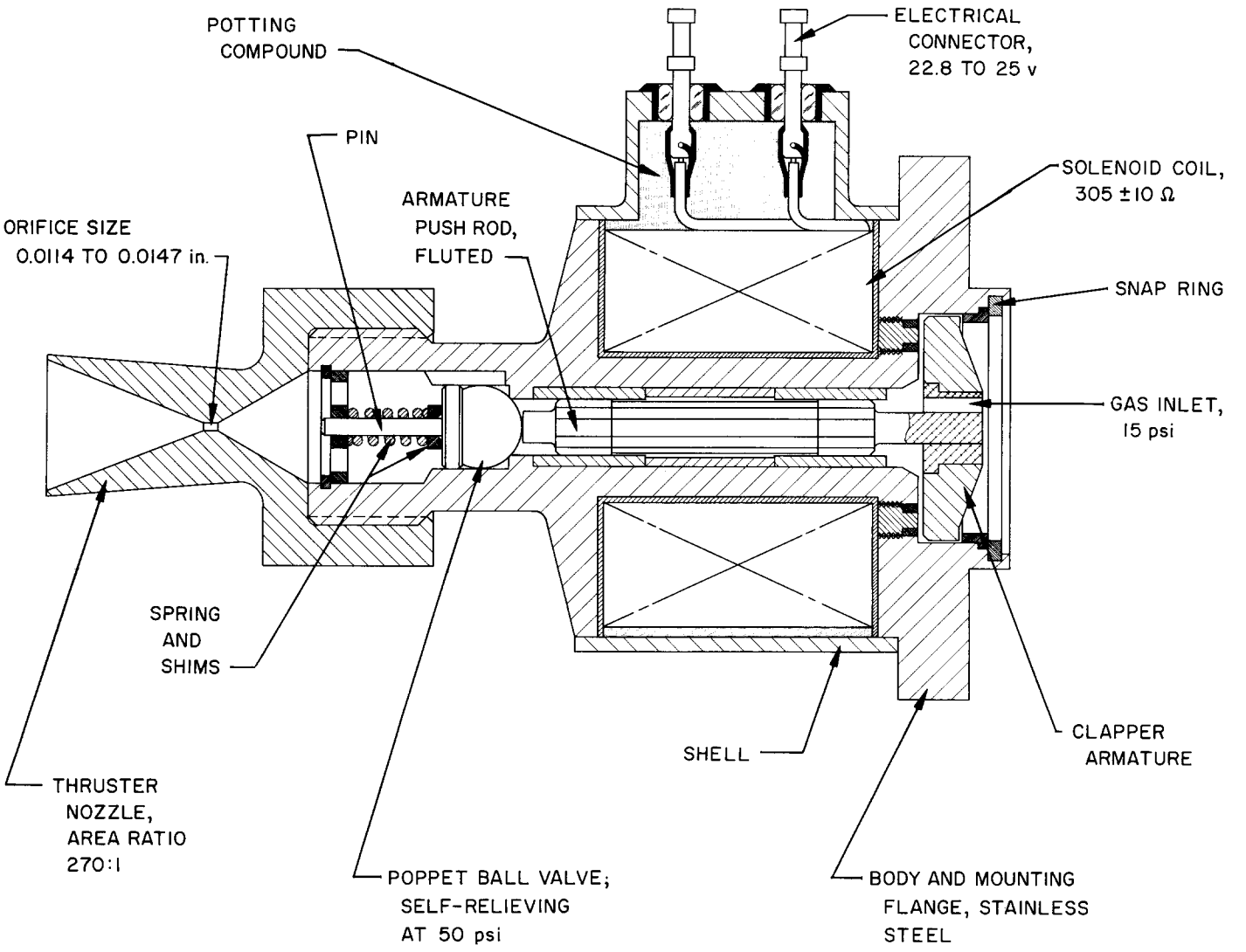

Fig. 14. *Mariner* Mars 1964 solenoid-operated thruster

UNCLASSIFIED
CONFIDENTIAL

UNCLASSIFIED

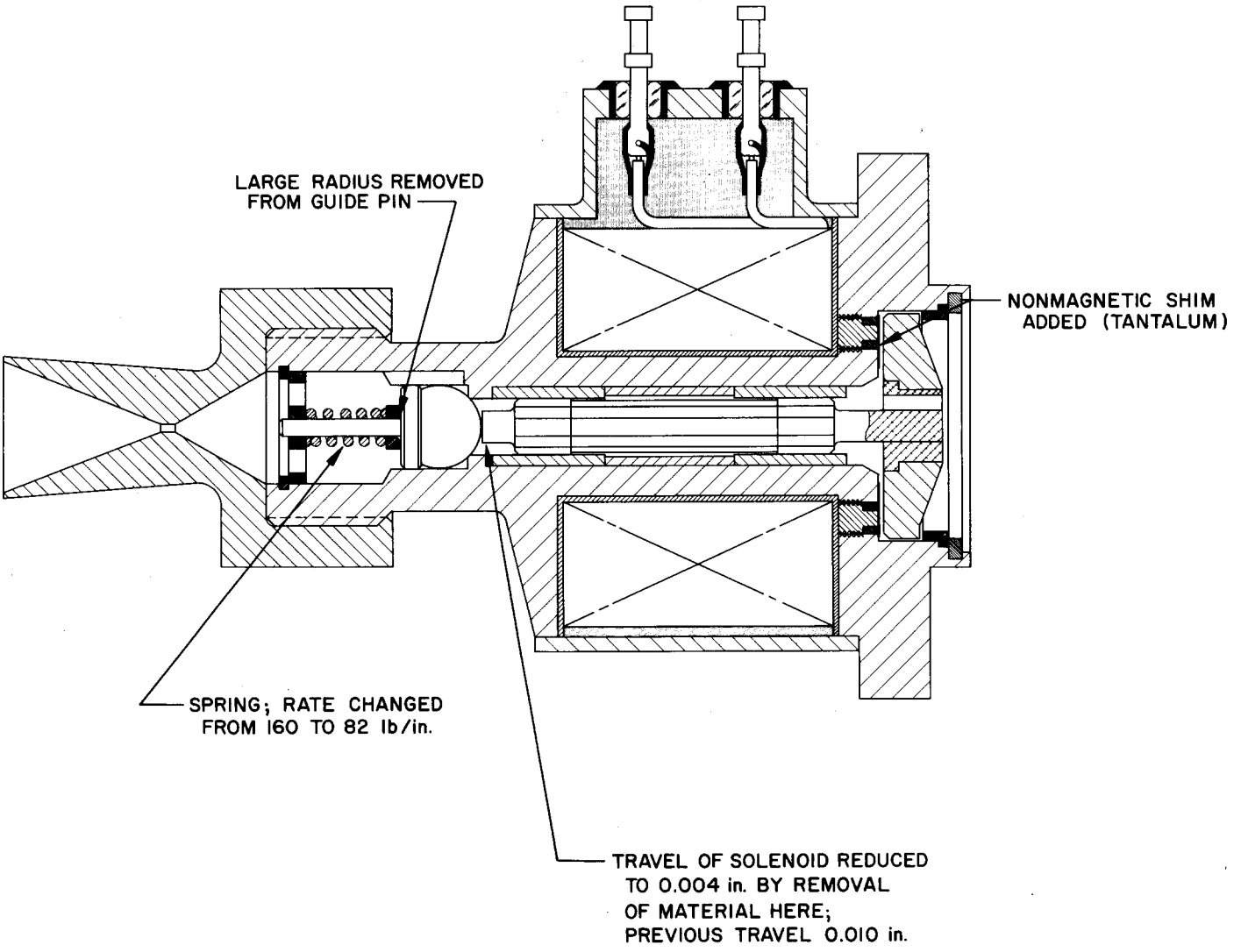

Fig. 15. Modifications to solenoid-operated thruster for *Mariner* Venus 67

The armature pull-in actuation current is 40 to 44 ma. In the original valve, the opening response time at 70°F is 12 msec at 22.8 v dc, which is the specified worst-case situation relative to spacecraft available voltage. Shims are used to adjust the self-relieving pressure to between 30 and 50 psi. Normal leakage rates vary between 0.3 and 3 cm^3/hr STP. An oscilloscope was used to monitor the current flowing through the solenoid coil during valve actuation relative to the current available at various temperatures. From the drawings of typical traces in Fig. 16, it is evident that at 300°F approximately 90% of the current available with a voltage of 22.8 v was needed to actuate the valves.

c. Valve modifications. Gas flow rate was found to be unchanged when the original valve armature travel of 0.010 in. was reduced to 0.003 in. It was decided to reduce the travel to 0.004 in., as shown in Fig. 15.

During tests of valve-response time versus relief pressure setting, it was noticed that valve actuation with increasing current was not a clean sharp break. This appeared to indicate that the spring rate of increasing force with travel might be too high relative to the solenoid rate of increasing force with decreasing air gap. The original valve spring rate was 164 lb/in. travel. New springs, with a rate of 82 lb/in., were obtained from Sterer Engineering. To provide proper seating for the shims used to adjust the self-relieving pressure of the new springs, a large radius on the valve spring guide pin was machined off. With the new spring installed and the relief pressure adjusted to 40 psi, the valves had a pull-in current of

UNCLASSIFIED

UNCLASSIFIED

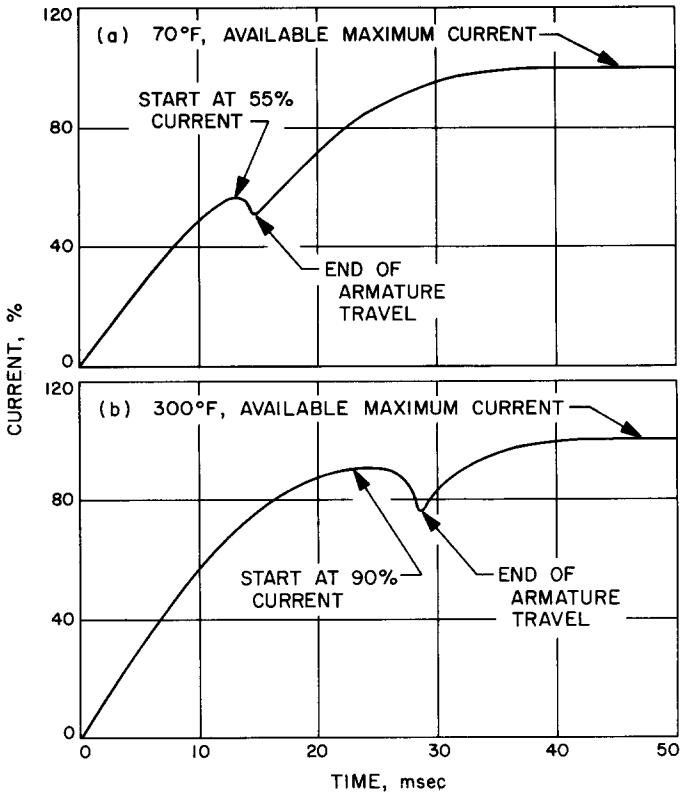

Fig. 16. Typical oscilloscope patterns obtained with original *Mariner*-type valve during actuation with 22.8 v dc, showing marginal operation at 300°F

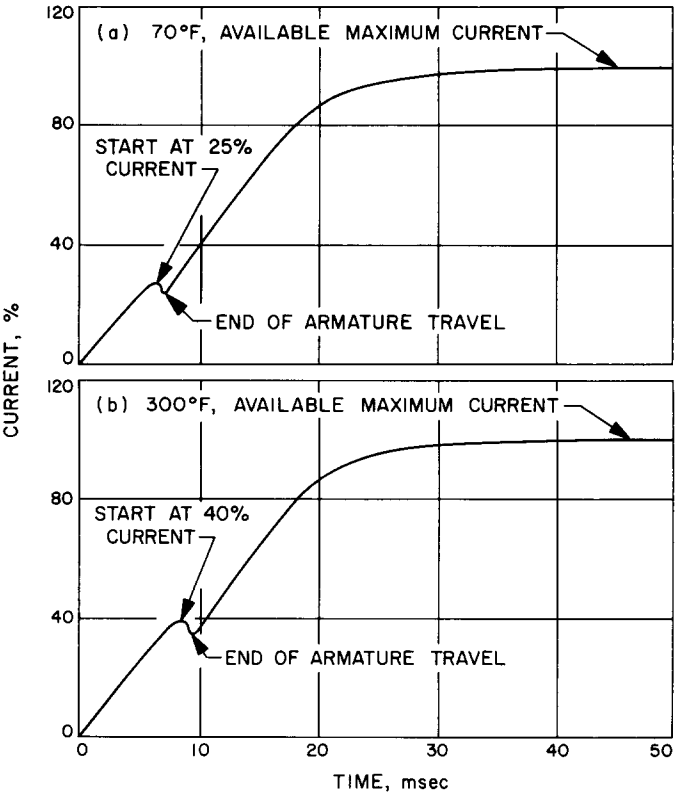

Fig. 17. Typical oscilloscope patterns obtained with reworked *Mariner*-type valve during actuation with 22.8 v dc, showing reliable operation at 300°F

approximately 20 ma and an opening time of 4 to 6 msec when actuated by 22.8 v dc with a 15-psi pressure drop. With the shorter valve travel, the closing time now was 3 or 4 msec. Residual magnetism in the clapper armature caused the drop-out time and amperage to be in excess of specifications. This deficiency was corrected by inserting an 0.001-in. shim of nonmagnetic tantalum in the solenoid air gap. Oscilloscope patterns obtained after the rework are illustrated by Fig. 17. When compared with those of Fig. 16 the improvement, especially at 300°F, is evident.

To check for uniformity of valve operation, the oscilloscope traces for repeated actuations were superimposed. At 300°F, the original *Mariner*-type valves appeared to function erratically, as shown by Fig. 18. At the same temperature, the reworked valve actuation traces all superposed precisely, as seen in Fig. 19. In these tests, the oscilloscope vertical deflection was adjusted so that the maximum current available through the coils at 22.8 v dc coincided with the fifth horizontal line. While the reworked valve operated almost perfectly with 40% of the

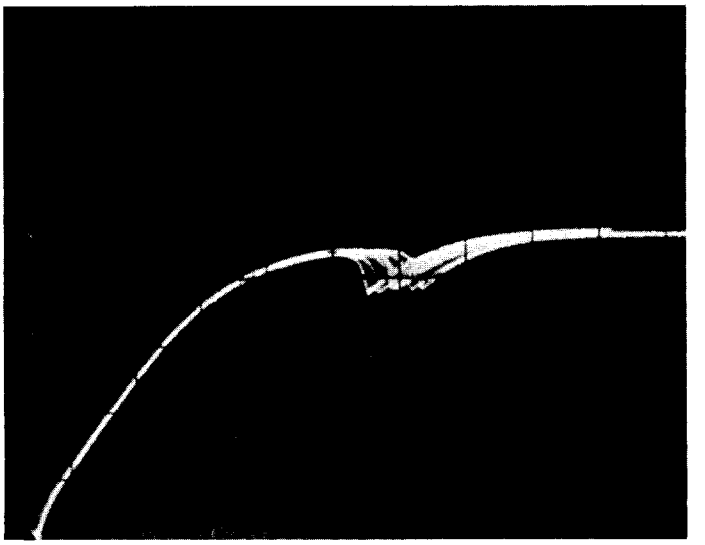

Fig. 18. Erratic operation of original *Mariner*-type valve at 300°F shown by 10 superimposed actuation traces, using 22.8 v dc and 5 msec/division

UNCLASSIFIED

UNCLASSIFIED

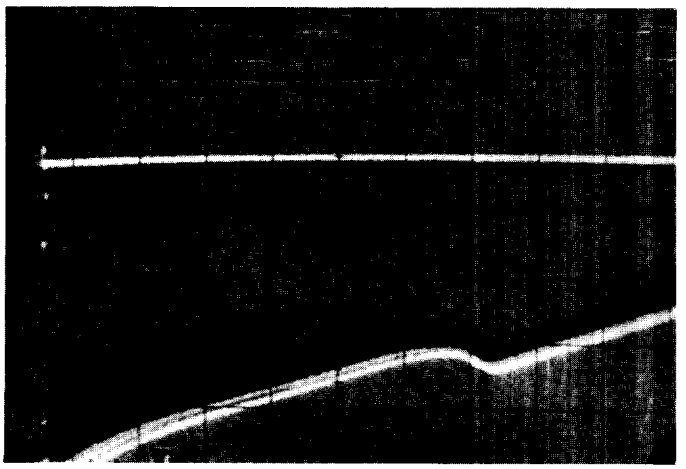

Fig. 19. Reliable operation of reworked *Mariner* valve at 300°F shown by 20 superimposed actuation traces, using 22.8 v dc and 1 msec/division

available current, the original valve had required nearly 95% of the available current. High temperature operation had no aftereffect on subsequent room temperature operation. The effect of applied voltage on the reworked *Mariner* Venus 67 valve response time at 70°F is shown in Fig. 20.

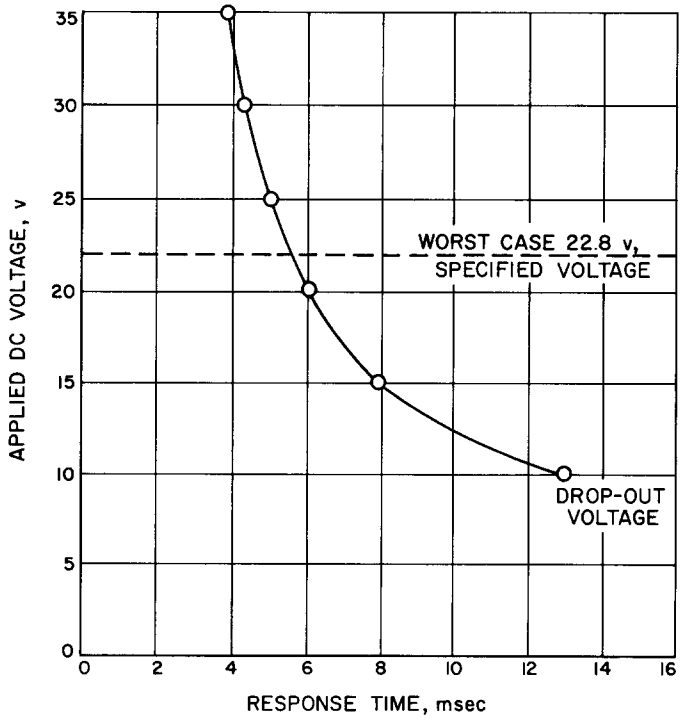

Fig. 20. Response time versus voltage for reworked *Mariner* Venus 67 thruster valve

E. Space Sciences

1. Mariner Mars 1964 Project: Mars Cartography From the Mariner IV TV Pictures

To determine the nominal locations of the 22 TV pictures taken of Mars by *Mariner IV*, information concerning the approach trajectory was combined in a computer program with information on the relative pointing direction of the TV camera, as well as the ephemerides for planet orbit position and axial rotation. This TV constraints program had been successfully used to compute the *Ranger* TV picture coverage of the Moon. The estimated locations have been mapped on the best available charts of Mars depicting the regions that had been photographed. One of the resulting maps is presented in Fig. 21.

If the ephemeris-derived latitude and longitude coordinate grids of Mars are to be considered as an absolute reference system, then four significant error sources affect estimates of picture locations. These are:

(1) Spacecraft trajectory uncertainties.

(2) Mars radius uncertainty.

(3) Camera misalignment with respect to the nominal Sun and Canopus sensor pointing directions measured from the spacecraft.

(4) Spacecraft attitude uncertainty within the control limit cycles.

The accuracies of the encounter trajectory and camera alignment have been well documented. An improved value for the Mars radius is not expected in the immediate future. Therefore, the attitude uncertainty remains as a major error source since attitude control data were not sent back during the TV picture-taking and recording sequence, Mode 3.

Map location uncertainties relative to the nominal values were estimated with the help of the *Ranger* constraints program and also the *Mariner* camera/Mars trajectory (MARCAM) program. The one-sigma uncertainty values were determined from the RMS contributions of the various error sources listed earlier. From these computations, the Picture 11 center location may be considered correct within 2 deg in latitude and 2.5 deg in longitude. For other pictures near the ends of the picture-taking sequence, the uncertainties are larger.

At first it was assumed that spacecraft attitude at the time each picture was taken could be determined by

UNCLASSIFIED

UNCLASSIFIED

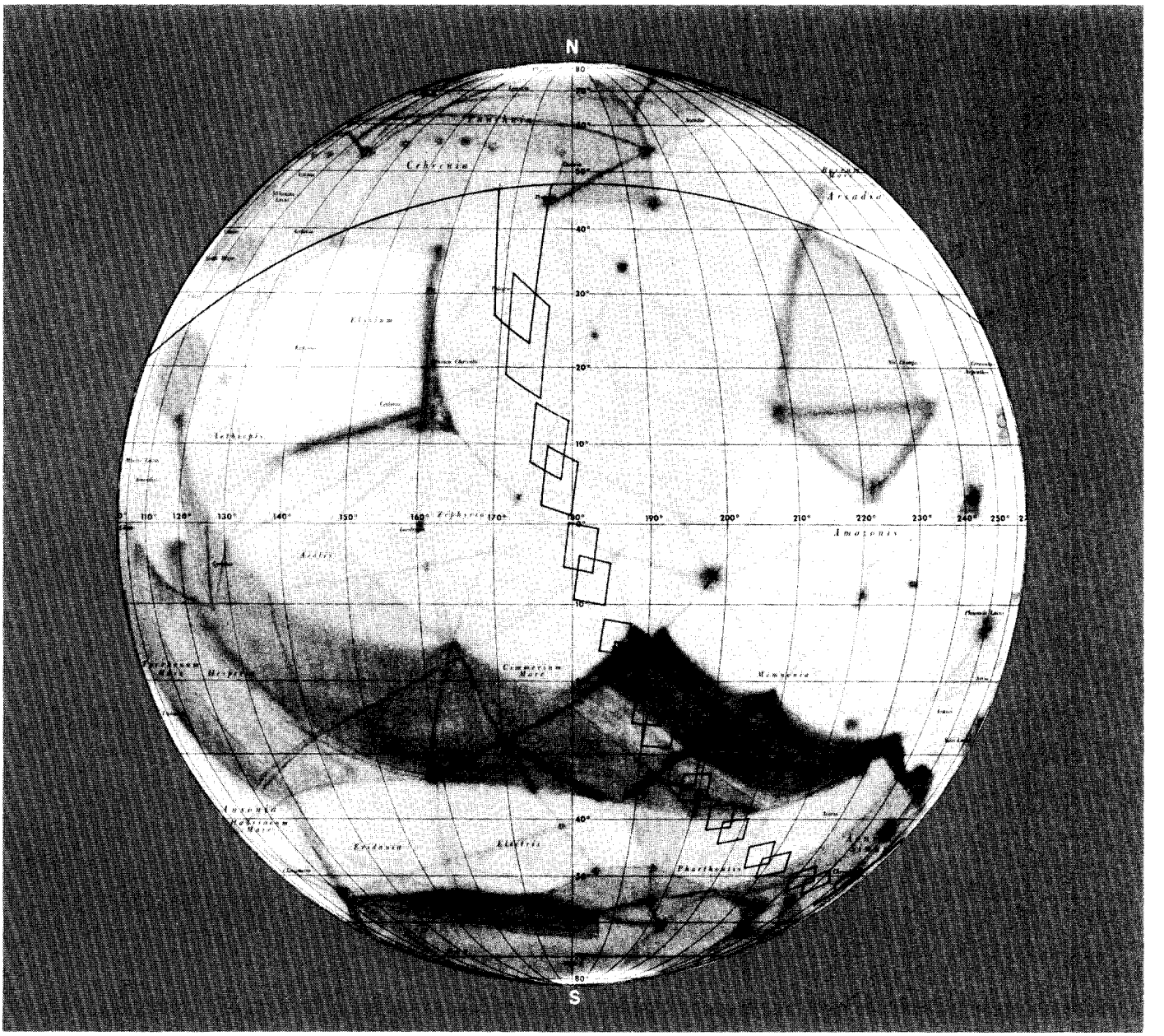

Fig. 21. Map of Mars showing nominal locations of *Mariner IV* TV pictures

UNCLASSIFIED

UNCLASSIFIED

backward extrapolation of telemetered data received within 15 min after TV encounter. However, the irregularities in the data curves are evident in Fig. 22. It is seen that the acceleration during the first pitch loop was approximately 30% lower than that for the remaining loops. In the yaw and roll channels, few data points were available since it was common for the roll and yaw jets to fire twice rather than once at the attitude limits. One checkpoint was available: the planet limb shown in Picture 1. Deceptively, it seemed reasonable that extrapolations could be based on the mean values of the measured leakage accelerations (from the shapes of the curves) and also on the rate increments measured at the turnaround points. When the most-probable extrapolated pitch, yaw, and roll values were input into the computer program, however, the planet limb came out in the wrong place.

Next, the picture overlap regions were examined to see in what direction the spacecraft was rotating during the interval between overlapping exposures. The resultant vectors (shown in Fig. 23) indicate the amount of change in position during the time between exposures and can serve as measures of rotation rates. For comparison, the position changes are also shown which would have resulted from a spacecraft rotation of 1 mrad in pitch, yaw, and roll during the same time interval. It appeared feasible to resolve the rotation vectors in terms of the respective unit vectors, and then these rates might be used to carry

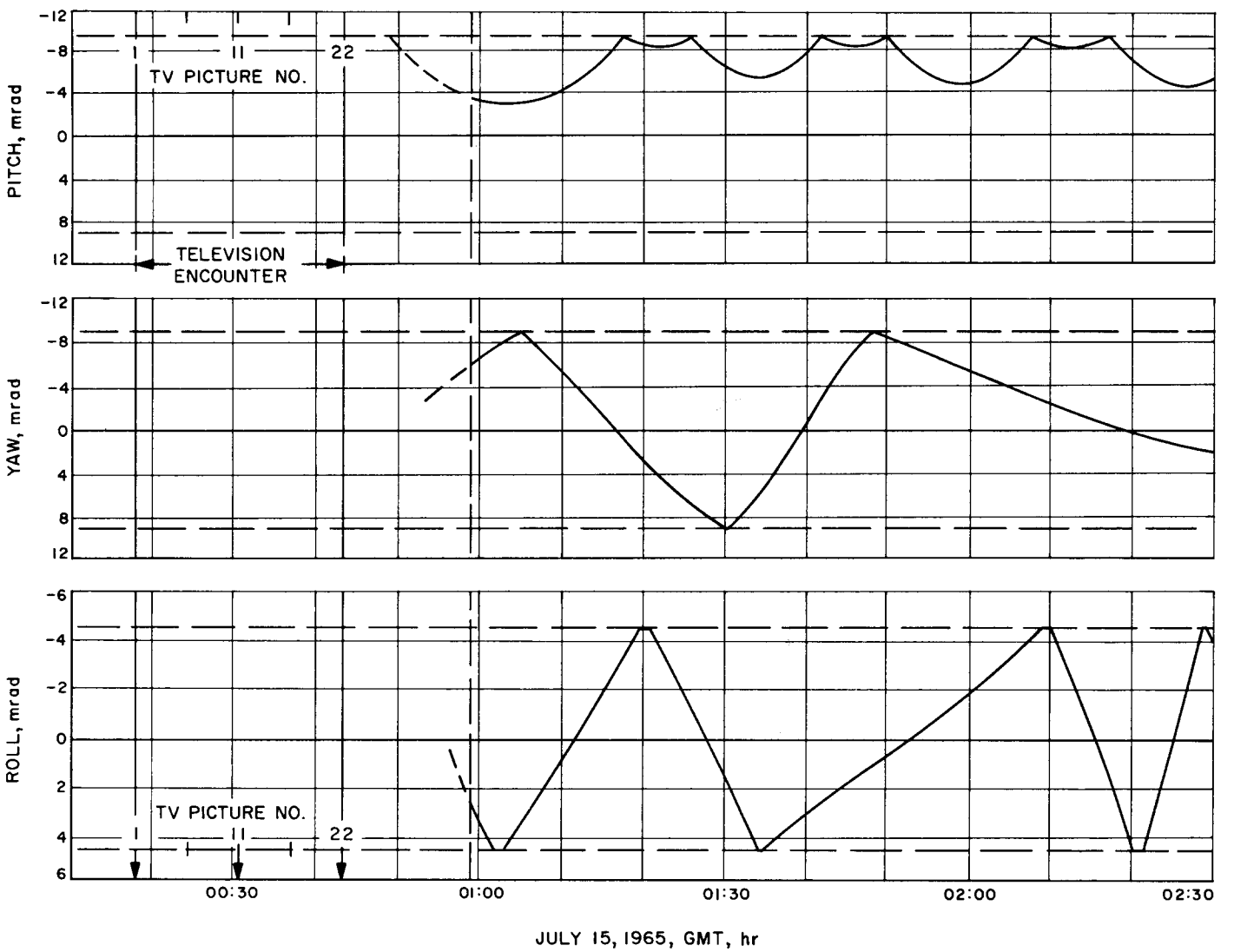

Fig. 22. *Mariner IV* postencounter attitude control data

UNCLASSIFIED

UNCLASSIFIED
CONFIDENTIAL

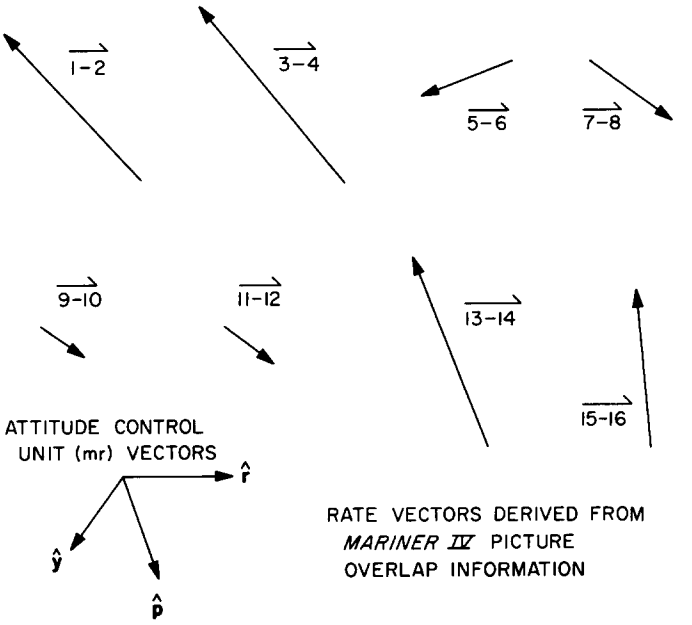

Fig. 23. Rotation rate vectors between overlapping TV pictures

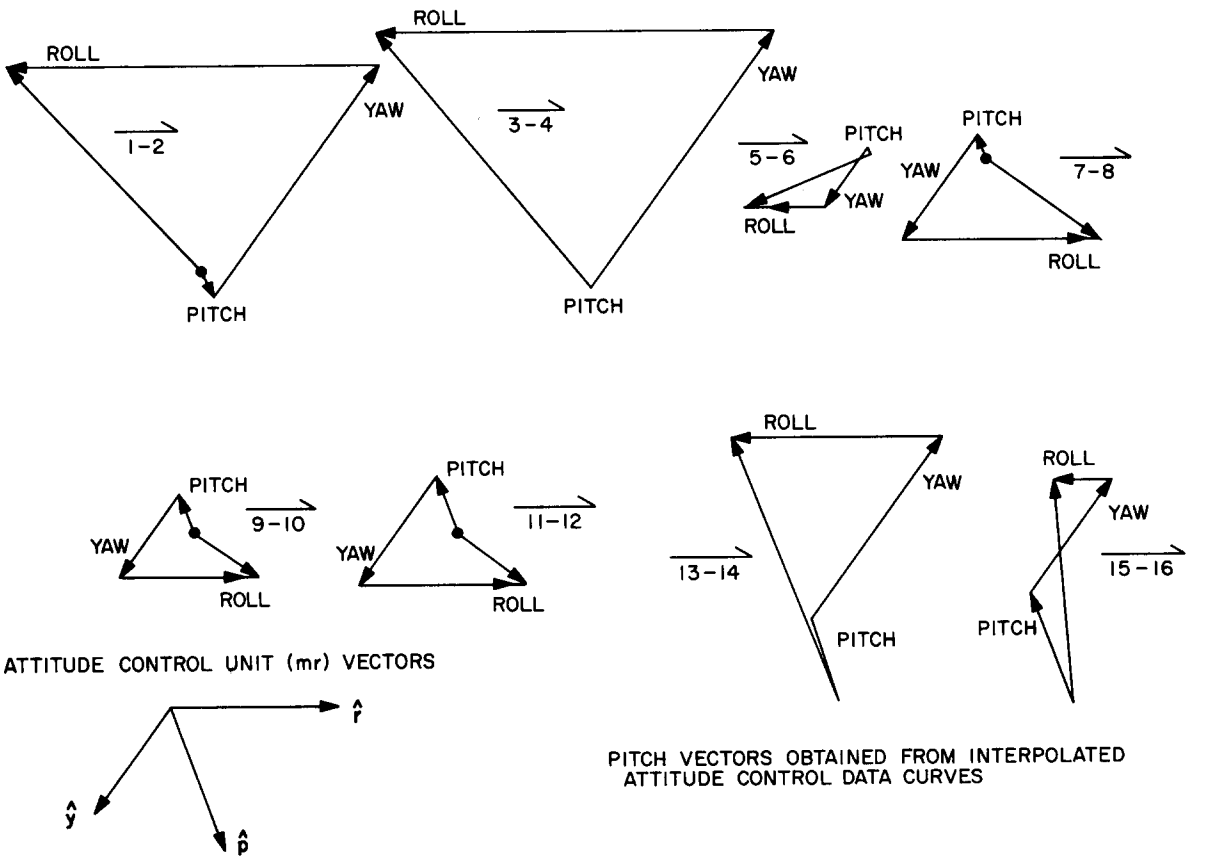

Fig. 24. Resolution of rotation vectors

UNCLASSIFIED
CONFIDENTIAL

out the position extrapolations which had been attempted earlier. Since there were three unit vectors, however, it was not immediately possible to obtain unique solutions for the rate vectors.

At this point, the preencounter attitude control data, which had ended approximately 2.5 hr before encounter, were also examined. It was found that the pitch-loop pairs, i.e., the large-plus-small loop, prior to encounter had periods of 40 ±2 min. When these data were extended forward through the time of encounter by adding approximately 3.5 of these 40-min loop pairs, it was found that the last loop merged with the first postencounter pitch loop. This successfully defined the behavior of one of the three channels, making it possible to resolve the rotation vectors in terms of the other two unit vectors. The results are shown in Fig. 24. Some significantly large changes are obvious. First, the yaw component changed from negative to positive between Pictures 4 and 5. Second, the roll rate changed from negative to positive between Pictures 4 and 7 (apparently between 5 and 6). Third, both the yaw and roll rates went from positive to negative between Pictures 12 and 13.

The hypothetical behavior of the limit cycles was used to fill in the attitude control data that had not been telemetered during encounter (Fig. 25). With this scheme, the planet limb in Picture 1 is placed in nearly the correct

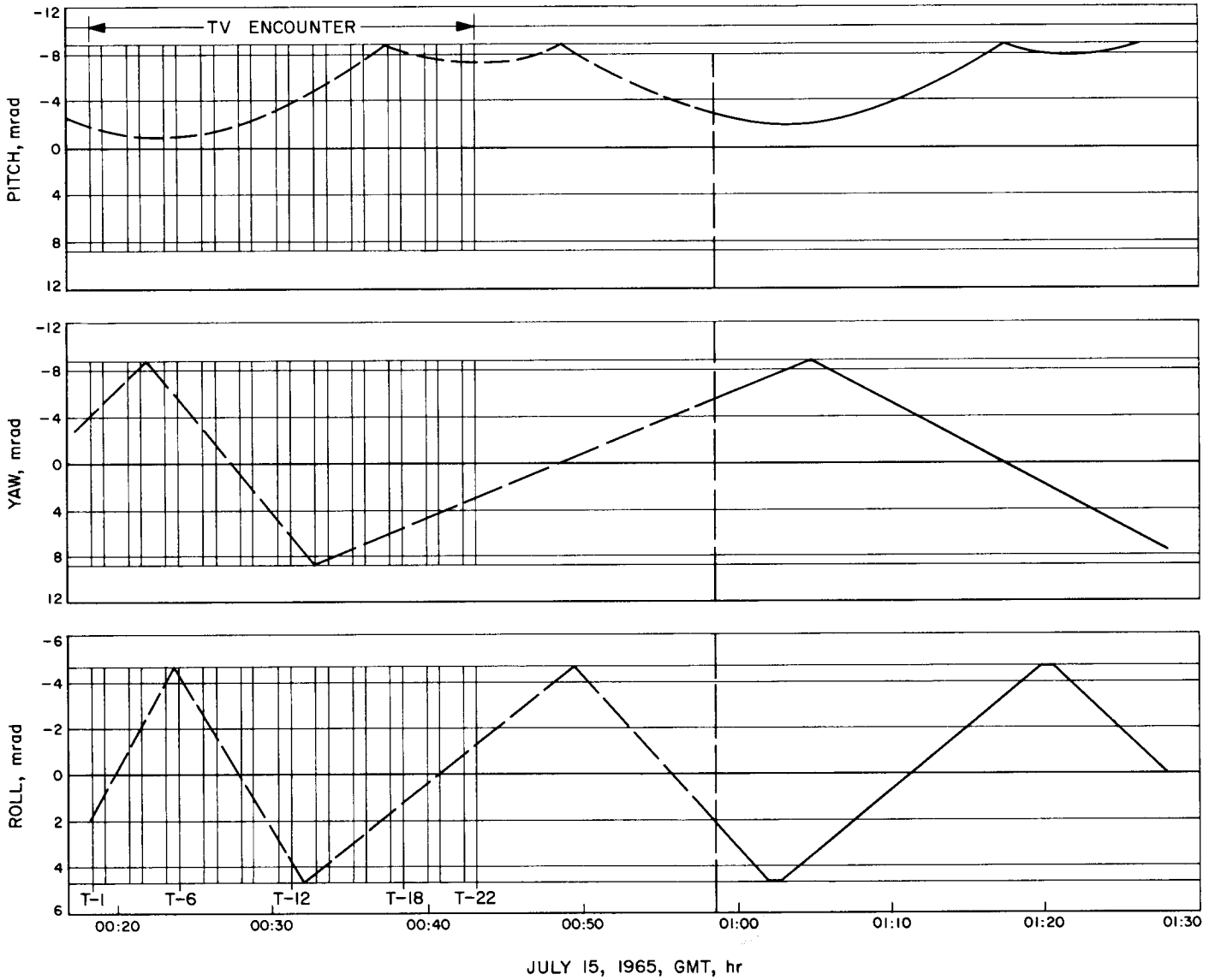

Fig. 25. Attitude control data extrapolated through the picture-taking period

UNCLASSIFIED

position. It now appears that the locations of many of the other pictures may now be determined to better than 2-deg one-sigma uncertainty, corresponding to 120-km distance, or approximately one-half the frame size.

F. Propulsion

1. Spacecraft Propulsion System

a. Introduction. The primary function of the *Mariner* Venus 67 postinjection propulsion system is to remove or reduce *Agena* injection dispersion errors so that a Venus flyby with a sufficiently small miss distance can be reasonably assured. This function is performed during the two possible spacecraft midcourse maneuvers, during which the spacecraft is directed to turn to a prescribed position in space and to impart a corrective impulse via the postinjection propulsion system.

2. System Description

A schematic of the propulsion system is shown in Fig. 26. The system design is identical to the *Mariner* Mars 1964 system except for a modification of the pyrotechnic cable harness. The system utilizes a liquid monopropellant, anhydrous hydrazine, as the propellant. It is functionally a regulated-gas-pressure-fed constant-thrust rocket. Principal system components consist of a high-pressure gas reservoir, pneumatic pressure regulator, propellant tank and propellant bladder, and a rocket engine containing a quantity of catalyst to accelerate the decomposition of hydrazine.

The system concept, shown in Fig. 26, is predicated on the basis that it satisfy the long-term space-storage (maximum of 250 days) and multiple start (maximum of two) requirements imposed by the *Mariner* Mars 1964 mission. Since the Venus mission is of shorter duration (approximately 130 days) and the operating temperature range is similar to that of the *Mariner* Mars 1964 mission, the propulsion system requires no major changes.

In order to meet the long-term storage requirements, pressurization by gaseous nitrogen is used in lieu of gaseous helium, the latter being more prone to leakage. In a like manner, welded and brazed tubing and fittings are used wherever possible to minimize the number of potential leak sources. Also, metal seals are used (where welding and brazing are impracticable) in place of elastomeric seals to alleviate the effects of radiation, hard vacuum, and long-term storage on the critical system seals. Multiple start capability is realized by the inclusion of "ganged" explosive valves with two parallel branches of normally-closed (start) and normally-open (shutoff) valve groups in the nitrogen and fuel circuits and two normally-closed valves in parallel in the oxidizer circuit. Individual oxidizer cartridges (15 cm^3 of nitrogen tetroxide, N_2O_4, each) are used for each of the two starts, both cartridges being pressurized by a common source.

The design and operational philosophy of the system shown in Fig. 26 are directed toward maximizing system reliability and reproducibility, minimizing preflight handling and spacecraft interactions, minimizing in-flight electrical signals and sequencing, and minimizing the number of system components. The propulsion system can be fueled, pressurized, and monitored for several weeks prior to emplacement within the spacecraft and the actual launch. In the pressurized and fueled condition, the system is safe for personnel to work around within a temperature range of 35 to 125°F (burst pressures of the pressure vessels are a factor of 2.2 greater than maximum working pressures at 125°F). No spacecraft umbilicals or hardlines are required to maintain the propulsion system in the "ready" condition.

3. Pyrotechnic Subsystem

The pyrotechnic subsystem has the same degree of redundancy as previous subsystems. It uses dual power supplies, dual firing switches, and dual squibs. Where dual squibs are not feasible, devices with dual bridge wires are employed. Command inputs are nonredundant except for the first command (*erect solar panels*), which uses a delayed separation switch as a backup and for the antenna position angle change (APAC), which has three backup alternatives.

The requirement for repositioning the high-gain antenna just before planet encounter resulted in some rework. The repositioning will be accomplished with a pinpuller identical to those used on the solar panel latches. Circuitry required for the added function has been designed and documented. Presently, two prototype units are being reworked to prove the feasibility of the modification and to gain experience in refabrication of flight-quality units.

The squib initiation circuitry of the *Mariner* Venus 67 spacecraft pyrotechnic subsystem is essentially the same as that used for *Mariner* Mars 1964. In fact, firing units from that program will be reworked, retested, and used.

UNCLASSIFIED

UNCLASSIFIED

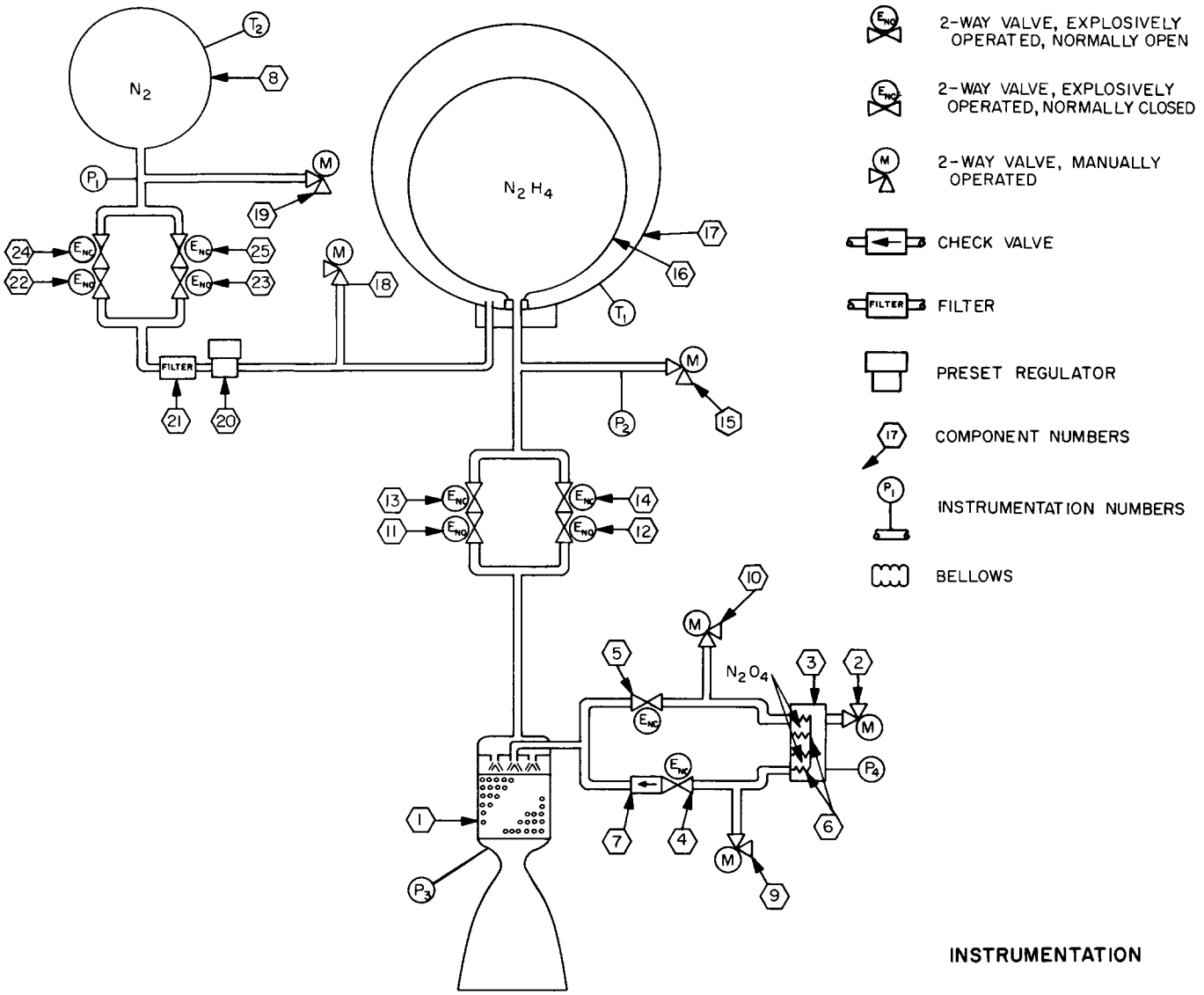

COMPONENTS

No.	DESCRIPTION
1	ROCKET ENGINE
2	N_2 FILL VALVE, IGNITION CARTRIDGE
3	N_2 RESERVOIR, IGNITION CARTRIDGE
4	OXIDIZER VALVE, START 1
5	OXIDIZER VALVE, START 2
6	OXIDIZER RESERVOIR, IGNITION CARTRIDGE
7	CHECK VALVE
8	NITROGEN TANK
9	OXIDIZER FILL VALVE 1, IGNITION CARTRIDGE
10	OXIDIZER FILL VALVE 2, IGNITION CARTRIDGE
11	PROPELLANT VALVE, START 1
12	PROPELLANT VALVE, START 2
13	PROPELLANT VALVE, SHUTOFF 1
14	PROPELLANT VALVE, SHUTOFF 2
15	FILL VALVE, PROPELLANT
16	PROPELLANT BLADDER
17	PROPELLANT TANK
18	PREPRESSURIZATION VALVE, NITROGEN
19	FILL VALVE, NITROGEN TANK
20	PRESSURE REGULATOR, NITROGEN
21	NITROGEN FILTER
22	NITROGEN VALVE, START 1
23	NITROGEN VALVE, START 2
24	NITROGEN VALVE, SHUTOFF 1
25	NITROGEN VALVE, SHUTOFF 2

INSTRUMENTATION

PRESSURE TRANSDUCERS

- P_1 NITROGEN TANK
- P_2 PROPELLANT TANK
- P_3 THRUST CHAMBER
- P_4 IGNITION CARTRIDGE N_2 RESERVOIR

TEMPERATURE TRANSDUCERS

- T_1 PROPELLANT TANK
- T_2 NITROGEN TANK

NOTE:
EVENT REGISTER DATA (BLIP DATA) ON EXPLOSIVE VALVE START AND SHUTOFF CURRENT

Fig. 26. *Mariner* Venus 67 postinjection propulsion system

UNCLASSIFIED

UNCLASSIFIED

The firing units contain switching circuitry which, upon command, will inhibit firing of the midcourse motor, release the inhibit, and transfer the command to fire the motor to either of the two groups of *on–off* squibs.

In the design of the spacecraft pyrotechnic firing units, the following spacecraft functions were considered:

(1) Pin retraction of four solar panel latches

(2) Pin retraction of one high-gain antenna latch

(3) First start, midcourse motor

(4) First stop, midcourse motor

(5) Second start, midcourse motor

(6) Second stop, midcourse motor

UNCLASSIFIED

UNCLASSIFIED

II. *Mariner* Mars 1969 Project

A. Introduction

The *Mariner* Mars 1969 Project was initiated in late-December 1965 and formally tasked on February 1, 1966. The primary objective is to conduct two Mars flyby missions in 1969 to make exploratory investigations of the planet which will set the basis for future experiments—particularly those relevant to the search for extraterrestrial life. The secondary objective is to develop the technology needed for succeeding Mars missions.

The spacecraft design concept will be based on the configuration of the successful *Mariner IV* spacecraft, with considerable modifications to meet the 1969 mission requirements and to enhance mission reliability.

The launch vehicle will be the *Atlas/Centaur* SLV-3C. This vehicle, developed under contract for and direction by the Lewis Research Center by General Dynamics/Convair, has a single- or double-burn capability in its second stage and a considerably increased performance rating over the *Atlas D/Agena D* used in the *Mariner IV* mission.

Mariner Mars 1969 missions will be supported by the Eastern Test Range launch facilities at Cape Kennedy, the tracking and data acquisition facilities of the Deep Space Network, and other NASA facilities.

Six planetary-science experiments have been tentatively selected by NASA (subject to integration capability) for the *Mariner* Mars 1969 missions; they are listed in Table 1. Additionally, a planetary-approach-guidance engineering experiment will be incorporated to test the feasibility and flight-readiness of on-board optical sensors and associated data processing techniques necessary for optical approach guidance.

Table 1. *Mariner* Mars 1969 scientific investigations

Experiment	Scientific investigator	Affiliation
Television	R. B. Leighton[a]	California Institute of Technology (CIT)
	B. C. Murray	CIT
	R. P. Sharp	CIT
	N. H. Horowitz	CIT
	J. D. Allen	Jet Propulsion Laboratory (JPL)
	A. G. Herriman	JPL
	L. R. Malling	JPL
	R. K. Sloan	JPL
	N. Davies	Rand Corporation
	C. Leovy	Rand Corporation
Infrared spectrometer	G. C. Pimentel[a]	University of California, Berkeley (UCB)
	K. C. Herr	UCB
Ultraviolet airglow spectrometer	C. A. Barth[a]	University of Colorado
	W. G. Fastie	Johns Hopkins University
Infrared radiometer	G. Neugebauer[a]	CIT
	G. Munch	CIT
	S. C. Chase	Santa Barbara Research Center
S-band occultation	A. J. Kliore[a]	JPL
	D. L. Cain	JPL
	G. S. Levy	JPL
Celestial mechanics	J. D. Anderson[a]	JPL

[a]Principal investigator.

UNCLASSIFIED

UNCLASSIFIED

Contractor selection activities for spacecraft subsystems continued during the reporting period. Contractors were put to work on two contracts, and selected for five more. For the engineering mechanics subsystems (structure, mechanical devices, packaging and cabling, and temperature control), Northrop Corporation's Space Laboratories, and for the radio subsystem, Philco Corporation's Western Development Laboratory, are at work both at the Laboratory and in the contractors' plants. Selection and negotiations were carried out for the following subsystems: telemetry and data storage (Texas Instruments), command and CC&S (Motorola, Inc.), and attitude control (Honeywell, Inc.). Contractual arrangements were also undertaken with the University of California for the infrared spectrometer.

System design of the spacecraft is still under way. Most of the functional requirements were written during this period and will be completed and released in the next reporting period. A number of problems still exist in evolving a mission and spacecraft design that will satisfy the various experiment requirements.

B. Project Engineering

1. Estimates of Proton Fluxes Expected in the Solar Flare Radiation Environment During Mariner Mars 1969 Missions

a. Introduction. Estimates of the proton fluxes expected in the solar flare proton radiation environment which the *Mariner* Mars 1969 spacecraft might encounter during flight to Mars are presented here. The estimates are based on the solar flare proton event flux measurements (and interpolation and extrapolation of the measured data) made during the past solar cycle (Cycle 19).

Predictions of solar activity (sunspot number) indicate that the current solar cycle will be less active than the past one, but with a one-sigma deviation that it will be almost as active. These predictions, however, are not totally supported; recent indications based on X-ray emissions from the Sun are that the current solar cycle might be more active than the past one. A reasonable conservative assumption, based on the present analyses, is that the current solar cycle will be similar to the past one. As a result, the estimates actually represent the maximum fluxes that occurred during the past solar cycle. These maximum fluxes represent estimates of the fluxes expected during 1969, which is the period of predicted maximum solar activity.

The results presented include estimates of:

(1) The time-history of a single event, yielding both peak flux and the flux behavior with time.

(2) The time-integrated flux of a single event.

(3) The time-integrated flux for a 6-mo mission.

(4) The time-integrated flux for 1 yr.

(5) The cumulative probability associated with a 6-mo mission having a mission flux greater than a prescribed flux.

No attempt is made to statistically predict future solar flare proton events, their occurrence dates or proton fluxes, because the data available are not an adequate statistical sample. Also, no attempt is made to establish environmental requirements, the quantities associated with the estimates, statistically or through uncertainty limits, from which test specifications and design requirements can be established. Finally, the fluxes presented do not include any estimates of uncertainty associated with the levels for future times because of the inherent uncertainties present when only one set of data on proton event fluxes is known.

b. Selection of a model solar flare proton event. The solar flare proton events and the proton radiation environment during an event have been studied in detail since 1956; therefore, the characteristic parameters are known for only a major part of the past solar cycle. Solar activity, however, has been well recorded, in particular by the relative sunspot number [Wolf number observed at the Zurich Observatory[1] (Ref. 1)] which goes back approximately 215 yr, covering 19 cycles. Because of the extensiveness of the data on sunspot numbers, statistical predictions of sunspot numbers for the current solar cycle (which began in late 1964) apparently are probable, with a reasonable range of uncertainty on time of occurrence and magnitude. The reasons for considering the prediction of solar activity, and the use of sunspot number in selecting the model solar flare proton event are:

(1) A large sample of quasi-periodic data is available to derive a prediction of an indicator of solar activity.

(2) A good correlation exists between the annual sunspot number and yearly flux from proton events.

[1]Final relative sunspot numbers made at the Zurich Observatory, Switzerland, are published in the *Journal of Geophysical Research* as a running compilation.

UNCLASSIFIED

UNCLASSIFIED

(3) A probable relationship exists between solar activity and the occurrence of solar proton events (i.e., as the solar activity indicator increases toward the peak, the proton event sizes and numbers increase; and, as the activity indicator decreases from the peak, the proton event sizes and numbers decrease).

Several statistical predictions of sunspot numbers for the current solar cycle have been made (Refs. 2–5). A rough average of the predictions is that the maximum sunspot number will be approximately ⅔ of that of the past solar cycle, which had a maximum during the 1957–58 period (maximum monthly smoothed Wolf number[2] of 190.2 occurred in 1957.5). The maximum sunspot number for the current solar cycle is expected in the 1968–69 period (which is approximately the time of the *Mariner* Mars 1969 flights). The method used in Ref. 2 predicts a maximum sunspot number of 135 ±54 (one-sigma deviation) to occur in 1969.8 ±0.7 yr. Of the several other referenced predictions, the maximum sunspot number is estimated to be 140 in 1968.1 (Ref. 3); 135 in 1968 with a probability of 0.75 that the maximum is in the range of 110 to 160 (Ref. 4); and approximately 130 in 1967 (Ref. 5). All techniques employed have inherent shortcomings which are not discussed in this report. The one-sigma upper limit estimate in Ref. 2 gives a maximum sunspot number for the current solar cycle which is approximately the same as the maximum for the past solar cycle.

A statistical approach has some basis, at least in predicting yearly fluxes, because a correlation between annual sunspot number and yearly flux has been demonstrated (Refs. 2 and 6). More importantly, however, is the indication that the activity of the current solar cycle will be less, but as an upper limit case it might be very similar to the past cycle. This assumption, however, cannot be totally supported because there is still a relatively large probability that it might be higher. Recent observations[3] of the X-ray emissions from the Sun during the current solar cycle indicate that the activity of the Sun will be even greater than that of the past solar cycle, provided the trend currently exhibited [the activity is approximately 25–30% greater now (1966) than for the corresponding period in the past cycle] is continued.

The assumption made, however, is that as a worst-case the activity of the current solar cycle will be the same as for the past one. A further assumption is that a linear correspondence exists between event yearly flux and sunspot number, which leads to the assumption that the occurrence of proton events and their fluxes would be about the same as that in the past solar cycle. A shortcoming of this last assumption is that the time of occurrence of the events and event size are practically impossible to predict. The most intense in size and the largest number of solar flare proton events, however, occurred 1 to 2 yr before and after solar maximum. When selecting a single event to be expected during maximum activity, the only choice was that of selecting one of the largest proton events that occurred during the near-peak period of solar activity in the past solar cycle. A large range in time, however, was provided to allow consideration of events that occurred up to 2 or 3 yr before or after solar maximum. This margin, of course, allows consideration of all of the large events of the past cycle.

Of the several largest events (i.e., February 23, 1956, July 14, 1959, and November 12, 1960 (Refs. 2, 6–8), the November 12, 1960 and July 14, 1959 events most nearly satisfy the conditions placed on time of occurrence and size of event. The results of a detailed study of the measured data on the November 12, 1960 event indicate that this was possibly the largest of any of the proton events having integral fluxes with energy $E > 30$ Mev. Furthermore, the upper limit obtained from the various measurements reported on this event (Refs. 9 and 10), including models obtained from the measured data through extrapolation and interpolation (Refs. 11 and 12), makes this the largest of all events having integral fluxes with $E > 10$ Mev. The uncertainties in the measurements and models of the other large proton events have not been considered in the same detail, but a preliminary study of tabulations (Refs. 2 and 7) indicates that the fluxes are consistently reported and accurate within a factor of 2 to 3. Therefore, any discrepancies which may arise owing to uncertainties in any of the other large solar proton events are expected to result in fluxes which are still less, or at the most no higher, than those of the November 12, 1960 event.

c. Event time-history. The November 12, 1960 solar flare proton event which began about 1320 UT was one of the best recorded and lasted approximately 50–60 hr. During this time, measurements were made with ground-based neutron monitors and riometers, emulsions and detectors flown in rockets, emulsions and counters carried aloft in balloons, and detectors carried in the *Explorer VII* satellite—all during the significant part of the solar flare event. Inconsistencies in the reduced measured data may be partially attributed to the variety of measuring techniques and the position of the instruments relative to the

[2]Monthly smoothed Wolf number is the average of two successive 12-mo running means.

[3]Preliminary information from Naval Research Laboratory, Washington, D.C.

UNCLASSIFIED

UNCLASSIFIED

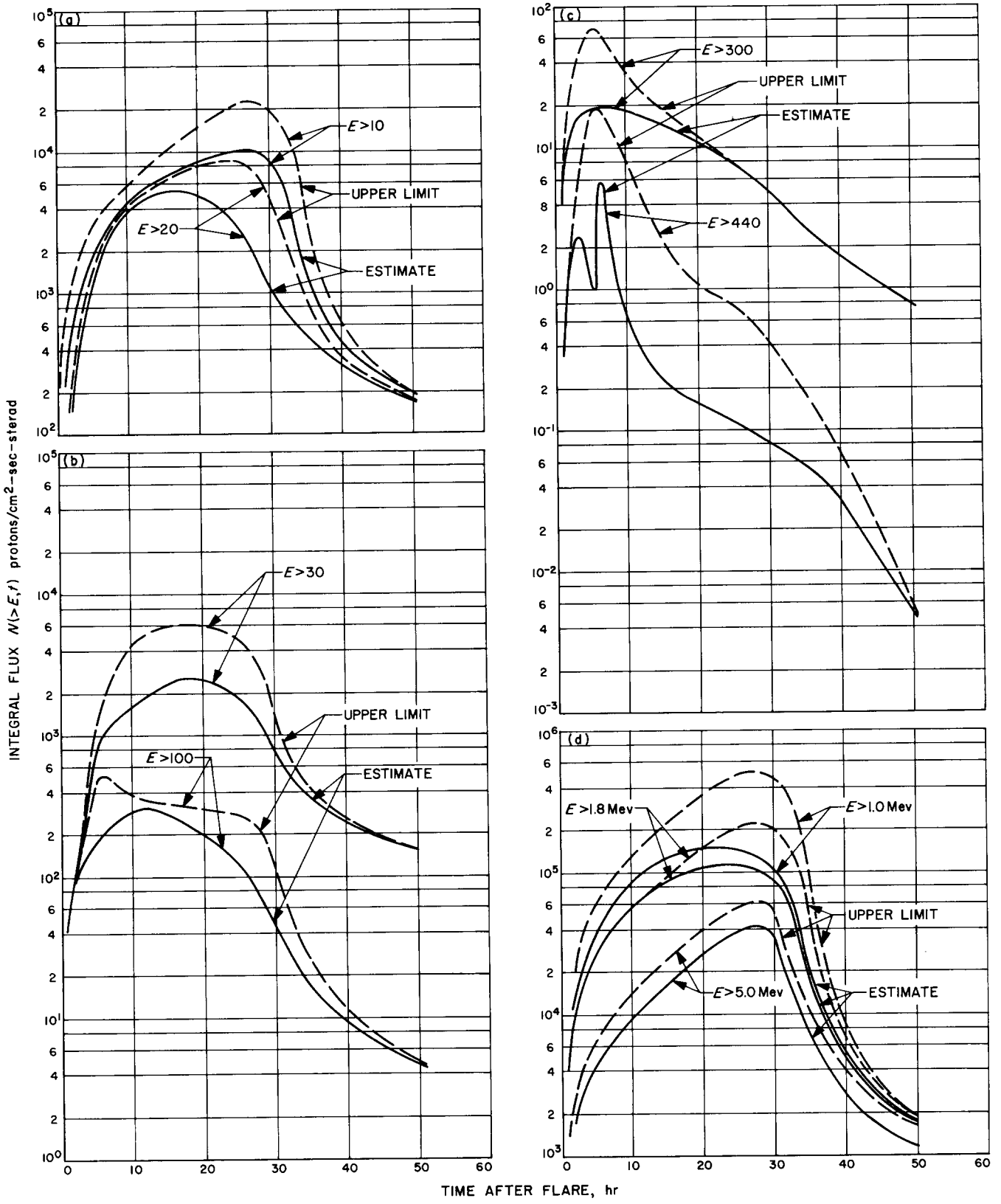

Fig. 1. Time-history of November 12, 1960 solar flare event representing an estimate of flux expected from a single event

UNCLASSIFIED

UNCLASSIFIED

Sun and Earth, thus involving instrument corrections and corrections for Earth-influencing environments.

For example, most of the data are consistent with the measurements made by the instruments carried in the rockets; that which disagrees may be attributed to (1) uncertainties in extrapolating balloon data to the top of the atmosphere; (2) uncertainty (or range of uncertainty) in the fluxes obtained from the satellite detector which had saturation problems; and (3) interpretation of the experimental observations into complete models of the time-history. The most probable time-history of the flux was determined by passing a curve through the data which was most consistent at a given point in time with the rocket data. The resulting curves are labeled "estimate" in Fig. 1 (a–c). The upper limits obtained by passing a curve through the highest fluxes reported are also indicated on Fig. 1 (a–c) by the curves labeled "upper limit." These curves represent both the interpolations and extrapolations of the referenced material as well as that necessary to construct the flux in the important region of time. Estimates of the fluxes representing the above "upper limit" and "estimate" cases, corresponding to the times at which the rocket instrumentation measurements were made, are presented in Table 2.

Table 2. Estimate and upper limit high-energy fluxes of the November 12, 1960 solar flare proton event

Energy, Mev	Integral flux $N(>E)$, protons/cm^2-sec-sterad		
	Time after flare		
	5 hr, 27 min	10 hr, 19 min	26 hr, 50 min
	Estimates		
30	8.5×10^2	1.6×10^3	1.6×10^3
100	1.9×10^2	2.9×10^2	9.0×10^1
	Upper limits		
30	1.4×10^3	4.5×10^3	3.7×10^3
100	5.0×10^2	3.8×10^2	2.4×10^2

The low-energy ($E < 5$ to 10 Mev) proton flux measurements presented were also made during the three different rocket flights since the emulsions and detectors were designed to give the energy spectrum of solar protons with energies between 200 kev and about 200 Mev (Ref. 9). The integral proton energy spectra found by analysis of the flight records indicated that the data at $E > 1.8$ Mev, taken at 5 hr, 27 min and 10 hr, 19 min, and at $E > 5$ Mev, taken at 26 hr, 50 min, is consistent with the more reliable high energy measurements and displays an approximate straight-line extrapolation back from 10- to 30-Mev data. Fluxes at energies below the 1.8 and 5 Mev data for the corresponding times (stated above) are highly questionable for several reasons (Ref. 13): (1) It is not clear that the data measured represents a simple extension of the spectrum of particles from the Sun or a separate phenomenon (e.g., it might represent the high-energy tail of the distribution of protons responsible for the magnetic disturbances which occurred prior to the November 12, 1960 event); and (2) The effects of magnetic cutoffs, which are indicated in the data, are difficult to determine because of the large uncertainties expected in cutoff values during magnetic disturbances.

The behavior indicated by the measured data below 1.8 and 5 Mev is a corresponding absence of particles between 0.35 and 1.8 Mev for the 1.8-Mev cases and between 1.8 and 5 Mev for the 5-Mev case. The approach used was to extrapolate the data down to 1 Mev by using a straight-line extrapolation back to the lowest data point (i.e., 0.2 Mev) and reading the flux estimate at 1 Mev for the three stated times. Fig. 1(d) gives the time-history of these low-energy particles, including both estimates and upper limits. Table 3 lists the estimates of integral fluxes at the lower energies and also lists the upper limits of the integral fluxes at the same energies and times. The upper limits were determined by extrapolating back to 1 Mev from the underlined data points (see Table 3) using a straight-line extrapolation having the same slope as that of the two next higher energy data points. The uncertainty in these estimates is impossible to assess; but the estimates and upper limits are expected to be conservative based on the known data.

d. Time-integrated flux

Single-event flux. The time-integrated fluxes for the November 12, 1960 event were determined by numerically

Table 3. Estimate and upper limit low-energy fluxes of the November 12, 1960 solar flare proton event

Energy, Mev	Integral flux $N(>E)$, protons/cm^2-sec-sterad		
	Time after flare		
	5 hr, 27 min	10 hr, 19 min	26 hr, 50 min
	Estimates		
1.0	4×10^4	9×10^4	1.3×10^5
1.8	3×10^4	6×10^4	1×10^5
5.0	7×10^3	1.5×10^4	6×10^4
10.0	2.3×10^3	4.5×10^3	1×10^4
	Upper limits		
1.0	7×10^4	1.3×10^5	5.0×10^5
1.8	$\underline{3 \times 10^4}$	$\underline{6 \times 10^4}$	2.2×10^5
5.0	$\underline{7 \times 10^3}$	$\underline{1.5 \times 10^4}$	$\underline{6 \times 10^4}$
10.0	3.6×10^3	5.9×10^3	$\underline{2.2 \times 10^4}$

UNCLASSIFIED

UNCLASSIFIED

integrating over the curves given in Fig. 1 (a–d). The factor 4π was factored into the results on the basis that 4π isotropy is consistent with the reported data. The results are presented in Fig. 2. A comparison of the two curves shows that the estimate is smaller than the upper limit by less than a factor of 2 for energies between 5 and 400 Mev. The results represent the fluxes of this event more accurately around 10 to 100 Mev than at lower energies because the higher energy band was the one in which most of the measurements were made and more consistency was displayed. One model (Ref. 11), however, which was based on extrapolation of balloon data to the top of the atmosphere indicates the $N(>E = 30$ Mev) should be about 9×10^9 protons/cm^2. The upper limit given in Fig. 2 is 4.5×10^9 protons/cm^2. The larger value

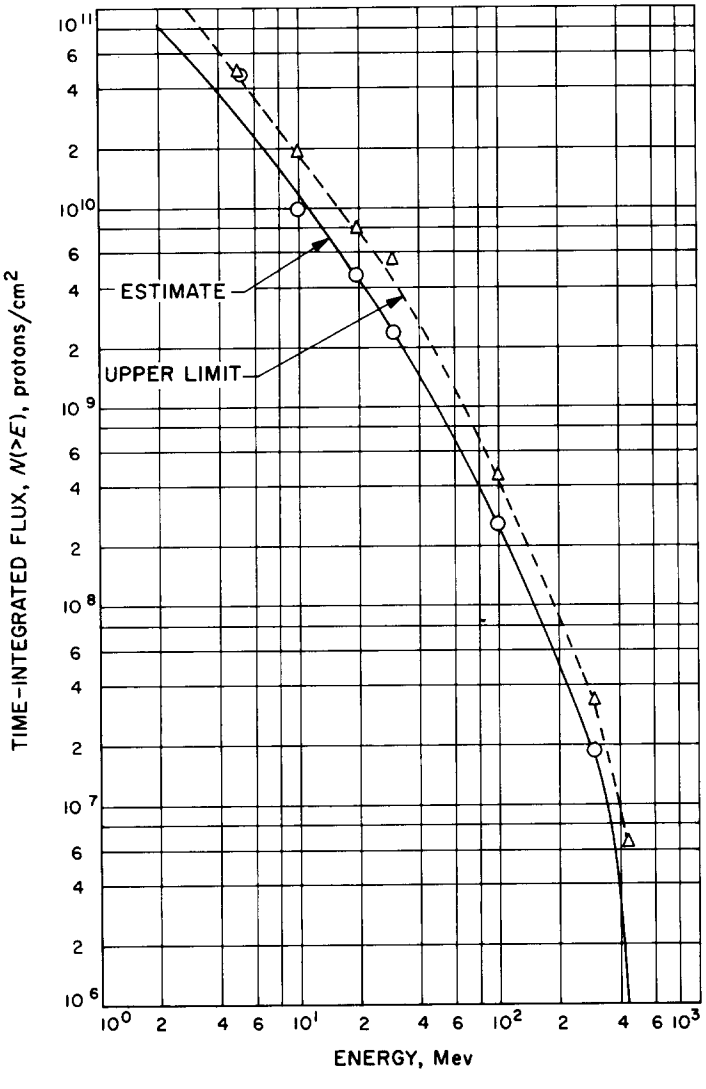

Fig. 2. Model solar flare proton event of November 12, 1960 representing an estimate of flux expected from a single event

is not disregarded because the 30-Mev region is the one in which a knee is usually present in the distributions of protons from solar flare events; therefore, the data points on either side could still be reasonably correct, but at 30 Mev the knee would simply be more pronounced if a larger flux were used. Nevertheless, the results and estimates below 10 to 30 Mev should carry with them a larger uncertainty than the higher energy fluxes; especially for the reasons discussed in Section c.

Six-month mission flux. During 1969, the spacecraft is expected to encounter several solar flare proton events, based on an approximate average of four per year, obtained from all of the known data on the past solar cycle (1956–1963). Also, the average number per year increases if the individual years around the time of solar maximum are considered. The mission-integrated proton flux expected during the 6-mo flight period in 1969, therefore, should be greater than the average flux. First, because the time of flight roughly corresponds to the time period at, or within approximately 1 yr of, the expected maximum solar activity (based on the predicted maximum sunspot number and its occurrence data for the current solar cycle). Second, assuming that the solar flare events in the current solar cycle will occur roughly in the same pattern as those of the past solar cycle, then the corresponding time period in the past cycle is between 1956–1960, which is the time when the events that were largest in size and greatest in number occurred.

During the 1956–1960 period, there were several extremely large solar flare proton events: February 23, 1956; July 1959; and November 1960. The integral fluxes of

Table 4. The two largest time-integrated fluxes accumulated over 6-mo periods in the past solar cycle

Time period	Integral flux $N(>E)$, protons/cm^2			
	$E > 5$ Mev	$E > 10$ Mev	$E > 30$ Mev	$E > 100$ Mev
February–July 1959	5×10^{10}[a]	2.2×10^{10}	4.1×10^9	3.7×10^8
June–November 1960				
Estimate of November 12, 1960				
Event included in sum	3.5×10^{10}[a]	1.5×10^{10}	3.2×10^9	3.9×10^8
Upper limit of November 12, 1960				
Event included in sum	5×10^{10}[a]	2.1×10^{10}	5.2×10^9	5.8×10^8

[a]Extrapolated to 5 Mev using slope of November 12, 1960 event.

UNCLASSIFIED

UNCLASSIFIED

the flares in two different 6-mo periods are listed in Table 4. The July 1959 events occurred in one period, the November 1960 events in the other.

The magnitudes of the fluxes for the two time periods listed in Table 4 are all roughly the same for corresponding energies. As evidenced by these results, within a period of less than 2 yr, there were two 6-mo periods which exhibited the largest accumulated fluxes during the past solar cycle. More importantly, both of these periods occurred near, and just after, the time of maximum solar activity for the past cycle. Thus, a reasonable assumption is that the mission-integrated fluxes for the *Mariner* Mars 1969 spacecraft should be reasonably represented by the estimates given in Table 4. This assumption implies that the current solar cycle will have the same frequency of flare occurrence and the same event sizes, which is not at all possible to support.

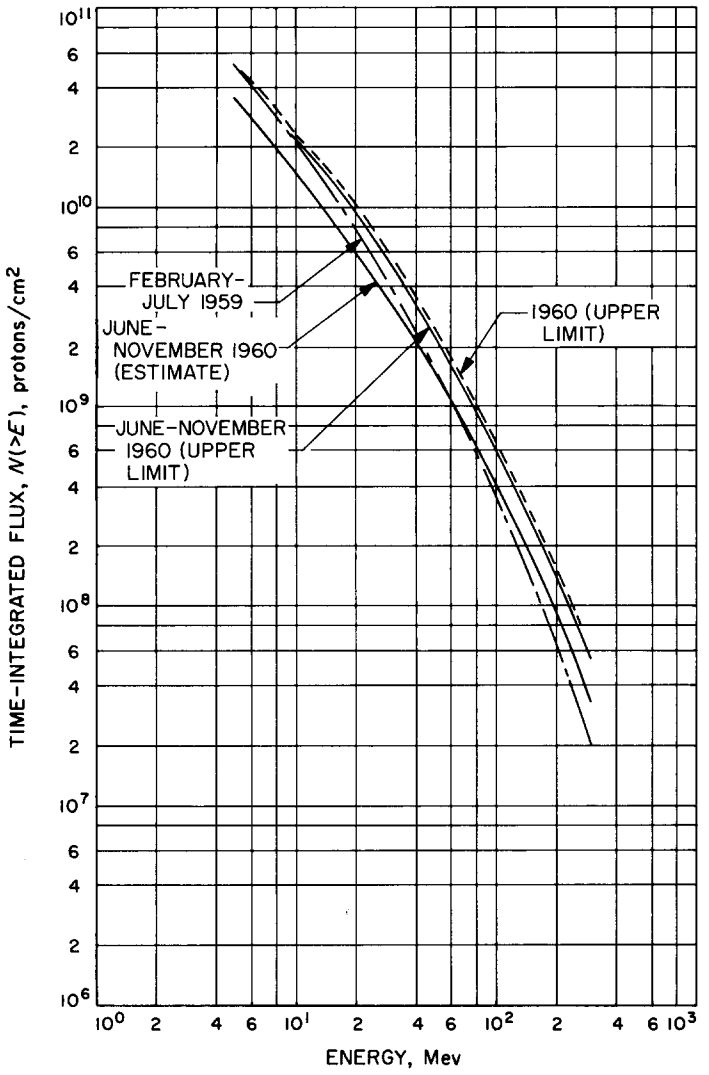

Fig. 3. Model solar flare proton flux representing an estimate of flux expected during a 6-mo period

For comparison purposes, the above data are plotted in Fig. 3 along with the maximum yearly integrated flux. The maximum presented represents the data reported for 1960, including the upper limit fluxes of the November 12, 1960 solar flare event determined in this report. This comparison strongly indicates the dominance of the single event, which is also exhibited in 1959 by the single July event.

Six-month mission flux probability. The questions which generally arise when one is predicting estimates of fluxes in the solar flare proton environment for spacecraft missions are: What is the probability that the spacecraft will encounter one or more solar flare proton events, and, what is the probability that the spacecraft will encounter a given flux or greater? Because the mission is relatively long with respect to the time between event occurrences, a reasonable assumption is that several events will be encountered and the assumption is especially applicable since the flight is during or near the time of the next solar maximum. The remaining question is: What is the probability of encountering a given flux or greater during the flight period? Fig. 4 (a–c) gives estimates of the probability of encountering a total 6-mo mission-integrated proton flux $N(>E)$, or greater for particle energies greater than 5 Mev [Fig. 4 (a)], 10 Mev [Fig. 4 (b)], and 30 Mev [Fig. 4 (c)], based on 1956–63 and 1958–1960 integrated data. The individual 6-mo fluxes were determined by summing up the integrated fluxes of all flares during consecutive 6-mo periods taken at 1-mo intervals. The two sets of event data were considered because: (1) The data from 1956–1963 yields average probabilities over total solar cycle and, (2) The data from 1958–1960 yields probabilities which are more representative of the flight time period. Probabilities were calculated using the approximation that $P_i\ (\geqq N) = i/(n+1)$ where i is the number 1, 2, 3, . . . n, associated with the 6-mo integrated fluxes listed in descending order of magnitude of flux. The value of i, therefore, is related to flux through: $i = 1$ for largest flux, $i = 2$ for next largest, etc. The cumulative probability distributions for the various cases were constructed using the Kolmogorov-Smirnov method of drawing a confidence band for cumulative frequency distributions (Ref. 14). The probabilities, labeled estimates and upper limits, simply mean that the estimate of the November 12, 1960 event was used in the one case and the upper limit of the November 12, 1960 event was used in the other case when determining the 6-mo integrated fluxes. Also listed on the figures is the differential probability ΔP, which

UNCLASSIFIED

UNCLASSIFIED

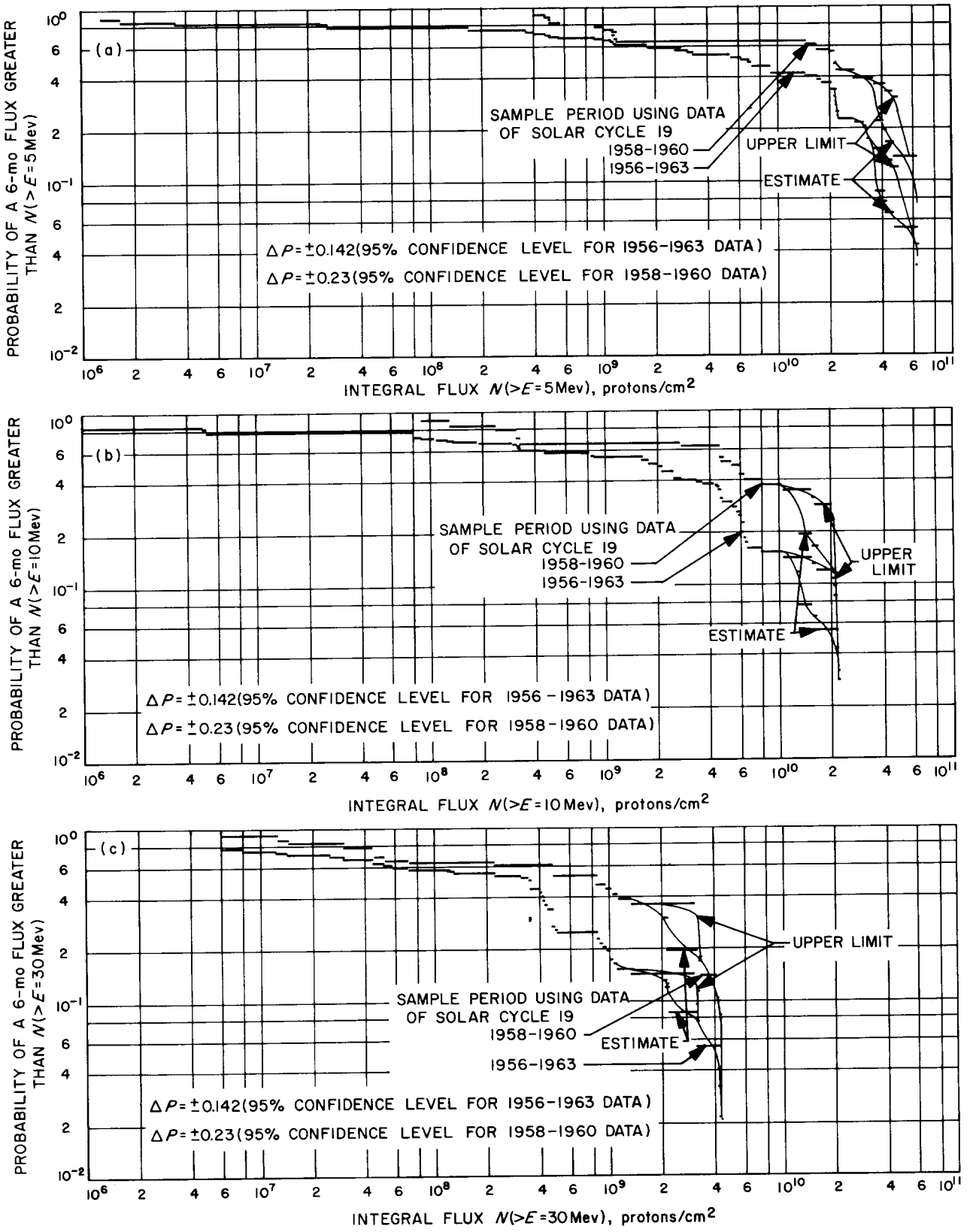
(a)
PROBABILITY OF A 6-mo FLUX GREATER THAN $N(>E=5\text{Mev})$
SAMPLE PERIOD USING DATA OF SOLAR CYCLE 19
1958-1960
1956-1963
UPPER LIMIT
ESTIMATE
$\Delta P = \pm 0.142$ (95% CONFIDENCE LEVEL FOR 1956-1963 DATA)
$\Delta P = \pm 0.23$ (95% CONFIDENCE LEVEL FOR 1958-1960 DATA)
INTEGRAL FLUX $N(>E=5\text{Mev})$, protons/cm^2
(b)
PROBABILITY OF A 6-mo FLUX GREATER THAN $N(>E=10\text{Mev})$
SAMPLE PERIOD USING DATA OF SOLAR CYCLE 19
1958-1960
1956-1963
UPPER LIMIT
ESTIMATE
$\Delta P = \pm 0.142$ (95% CONFIDENCE LEVEL FOR 1956-1963 DATA)
$\Delta P = \pm 0.23$ (95% CONFIDENCE LEVEL FOR 1958-1960 DATA)
INTEGRAL FLUX $N(>E=10\text{Mev})$, protons/cm^2
(c)
PROBABILITY OF A 6-mo FLUX GREATER THAN $N(>E=30\text{Mev})$
UPPER LIMIT
SAMPLE PERIOD USING DATA OF SOLAR CYCLE 19
1958-1960
ESTIMATE
1956-1963
$\Delta P = \pm 0.142$ (95% CONFIDENCE LEVEL FOR 1956-1963 DATA)
$\Delta P = \pm 0.23$ (95% CONFIDENCE LEVEL FOR 1958-1960 DATA)
INTEGRAL FLUX $N(>E=30\text{Mev})$, protons/cm^2

Fig. 4. Six-month probability of flux occurrence based on data for solar Cycle 19, taken near Earth (1.0 AU)

CONFIDENTIAL
UNCLASSIFIED

UNCLASSIFIED

must be added and subtracted to the plotted probability to obtain the 95% confidence band. The confidence band is directly dependent on sample size, thus the band is wider for the 1958–1960 set of data. Estimates of the cumulative probabilities are given in Table 5 for selected 6-mo integrated flux levels.

Table 5. Cumulative probabilities for a 6-mo flux greater than $N(>E)$ based on data[a] in 1958–1960 period during the past solar cycle

Integral flux $N(>E)$, protons/cm^2	Cumulative probability for 6-mo flux greater than $N(>E)$		
	$E > 5$ Mev	$E > 10$ Mev	$E > 30$ Mev
1.0×10^9	0.75	0.65	0.45
1.5×10^9	0.63	0.65	0.36
2.0×10^9	0.63	0.65	0.36
3.0×10^9	0.63	0.63	0.36
4.0×10^9	0.63	0.63	0.14
1.0×10^{10}	0.63	0.37	—
1.5×10^{10}	0.61	0.34	—
2.0×10^{10}	0.57	0.28	—
3.0×10^{10}	0.39	—	—
5.0×10^{10}	0.14	—	—

[a]Upper limit data on November 12, 1960 solar flare proton event included.

e. Conclusions. Predictions of the maximum sunspot number for the current solar cycle were used, in part, to justify the use of past solar cycle flux data to estimate the proton fluxes expected from a single event and during a 6-mo period during the *Mariner* Mars 1969 mission. The justification, based on the predicted maximum sunspot number indicating that the solar activity of the current solar cycle is expected to be less than the past solar cycle, and a correlation between sunspot number and annual flux from solar flare proton events, leads to the conservative conclusion that the solar activity and the size and number of solar flare proton events might be roughly similar to those of the past solar cycle. The assumptions made, however, cannot be supported statistically because of a lack of a representative statistical sample. Thus, the uncertainty present in the estimates may be large. However, it seems that when the largest events of the past solar cycle are considered and the largest 6-mo time-integrated fluxes are used to represent estimates of fluxes expected in the current solar cycle during the *Mariner* Mars 1969 mission, the probability of larger fluxes occurring during a single event or 6-mo period would be small. That is, the estimates do not represent most probable fluxes, but, the largest fluxes which may be expected to occur during the 1969 period. The 6-mo cumulative probabilities of having fluxes greater than $N(>E)$ are evidence of this point [Fig. 4(a–c)]. For example, the cumulative probability that the spacecraft would be exposed to a 6-mo flux greater than $N(>E = 10 \text{ Mev}) = 2 \times 10^{10}$ [upper limit case from Fig. 4(b)] is approximately 0.28 $\pm$0.142 (95% confidence band).

Because the November 12, 1960 event has a large uncertainty associated with the low-energy fluxes, the estimates of fluxes $E >$ (10 Mev) may be grossly incorrect due to extensive extrapolations back to low energies on the basis of only the low-energy data for the November 12, 1960 solar flare event.

All estimates presented pertain to the near-Earth region of space. Thus, the levels expected at encounter would be reduced approximately according to the inverse square of the distance law (roughly a factor of 2 provided the distance between Mars and the Sun is approximately 1.5 AU). This point was not elaborated upon because the time of event occurrence is unknown and the near-Earth estimates are upper limits.

Finally, considering the assumptions made, the uncertainties associated with the solar flare proton event data of the past solar cycle (probably within a factor of 2 to 3) and the inherent uncertainties associated with making predictions and estimates of proton fluxes from solar flare events (where the event fluxes vary over 5 to 6 orders of magnitude) make it extremely difficult to bracket the uncertainty associated with the estimates.

C. Systems

1. Mission Analysis

a. Arrival dates. In *SPS* 37-39, Vol. II, p. 11, it was pointed out that only Type I trajectories would be used for the *Mariner* Mars 1969 missions. The exact trajectories had not been narrowed down at that time. Currently, the desirable arrival dates for the missions lie between August 1 and 10, 1969. Two fixed arrival dates will be utilized over the launch period for the two spacecraft. In order to simplify encounter operations, the arrival dates will be separated by several days. A tentative selection of the arrival dates is August 1 and 7, 1969. The communication distances at encounter are 97 and 101 million km, respectively.

b. Aiming points. Two aiming points are also being considered for the two spacecraft. One point is located so

UNCLASSIFIED

UNCLASSIFIED

that the scan traces of the TV and infrared will pass approximately 5 deg below the northern edge of the south polar cap near closest approach. The other is located so that the scan traces will reach a maximum south latitude of approximately 30 deg. Both aiming points are located so that the spacecraft will pass on the illuminated side of Mars at a nominal periapsis altitude of approximately 3000 km, and both points will result in the spacecraft passing behind Mars so that Earth occultation will result.

c. Launch period. A minimum 1-mo launch period is a project requirement for the *Mariner* Mars 1969 mission. The launch period is restricted primarily by the declination of the outgoing asymptote *DLA* at the beginning of the launch period, and by energy requirement C_3 at the end of the launch period. The earliest possible day of the launch period will correspond to that for which $DLA = -45$ deg because of deep space tracking coverage requirements. For an August 1 and 7 arrival, the earliest possible days of the launch period are February 16 and 24, 1969, respectively. The maximum C_3 for a 750- to 850-lb spacecraft is estimated to be 30 to 34 km^2/sec^2. This will enable the launch period to continue until about mid-April for the August 7 arrival. The precise end of the launch period will ultimately be determined by the final launch vehicle performance capability.

A project decision on which launch mode (either direct ascent or parking orbit) to use will be made in a few weeks. For the parking orbit mode, the desirable launch azimuth corridor is 45 to 115 deg east of north. For the direct ascent mode, the corridor will extend from approximately 80 to 115 deg. The earliest possible launch date for the direct ascent mode (with dog-leg maneuver) is about February 16, 1969 for the August 1 arrival.

D. Engineering Mechanics

1. Introduction

The *Mariner* Mars 1969 Project requires the support of the following Engineering Mechanics flight subsystems:

Structure subsystem: includes the basic octagonal structure, scan platform support structure, basic electronic chassis and subchassis, superstructure, high- and low-gain antenna structure, solar panel structures, and the forward half of the launch vehicle spacecraft adapter.

Cabling subsystem: includes all spacecraft cabling.

Temperature control subsystem: includes hardware such as temperature control louvers, thermal shields, miscellaneous Sun shades, and the temperature control flux monitor.

Mechanical devices subsystem: includes scan platform, solar panel dampers, antenna dampers, solar panel deployment and latching equipment, the separation initiated timer (SIT), and the pyrotechnic arming switch (PAS).

Support is also provided for systems test and operations involving the spacecraft system. These areas are:

Ground handling equipment: includes all supporting, hoisting, positioning, and shipping hardware.

Weight and center-of-mass hardware: used to experimentally determine the spacecraft center-of-mass position, and to position the propulsion motor thrust axis through the spacecraft center of mass.

Additional support is provided the Project in the following Engineering Mechanics areas:

(1) Spacecraft materials and applications

(2) Spacecraft temperature control support

(3) Spacecraft structural and dynamic analysis and test

(4) Electronic component procurement and screening

(5) Design, drafting, and specification support

(6) Launch vehicle mechanical interface design, test, and hardware

Subsequent volumes of *SPS* will contain reports of the significant developments on the *Mariner* Mars 1969 Project in the above areas. This report contains a current description of the spacecraft mechanical configuration and brief summaries of the current status of the four flight subsystems.

2. Mechanical Configuration

The *Mariner* Mars 1969 configuration (Fig. 5) draws heavily on the *Mariner* Mars 1964 design and operational experience. Principal changes are because of: (1) the use of the *Atlas/Centaur* launch vehicle (*Mariner* Mars 1964 used the *Atlas/Agena*); (2) the scientific payload; and (3) the spacecraft trajectory during the preencounter and postencounter period. Items (2) and (3) are aspects of the scientific mission but are separated here to differentiate the instrument physical characteristics from trajectory considerations.

UNCLASSIFIED
CONFIDENTIAL

UNCLASSIFIED

: includes hardware
, thermal shields, mis-
mperature control flux

ncludes scan platform,
npers, solar panel de-
he separation initiated
rming switch (PAS).

ms test and operations
ese areas are:

cludes all supporting,
hardware.

ware: used to experi-
: center-of-mass posi-
ion motor thrust axis
ss.

e Project in the follow-

lications
ol support
amic analysis and test
ement and screening
tion support
interface design, test,

contain reports of the
iner Mars 1969 Project
ains a current descrip-
onfiguration and brief
f the four flight sub-

ration (Fig. 5) draws
lesign and operational
ecause of: (1) the use
e (*Mariner* Mars 1964
ientific payload; and
the preencounter and
nd (3) are aspects of
ted here to differenti-
eristics from trajectory

LASSIFIED
NFIDENTIAL

UNCLASSIFIED

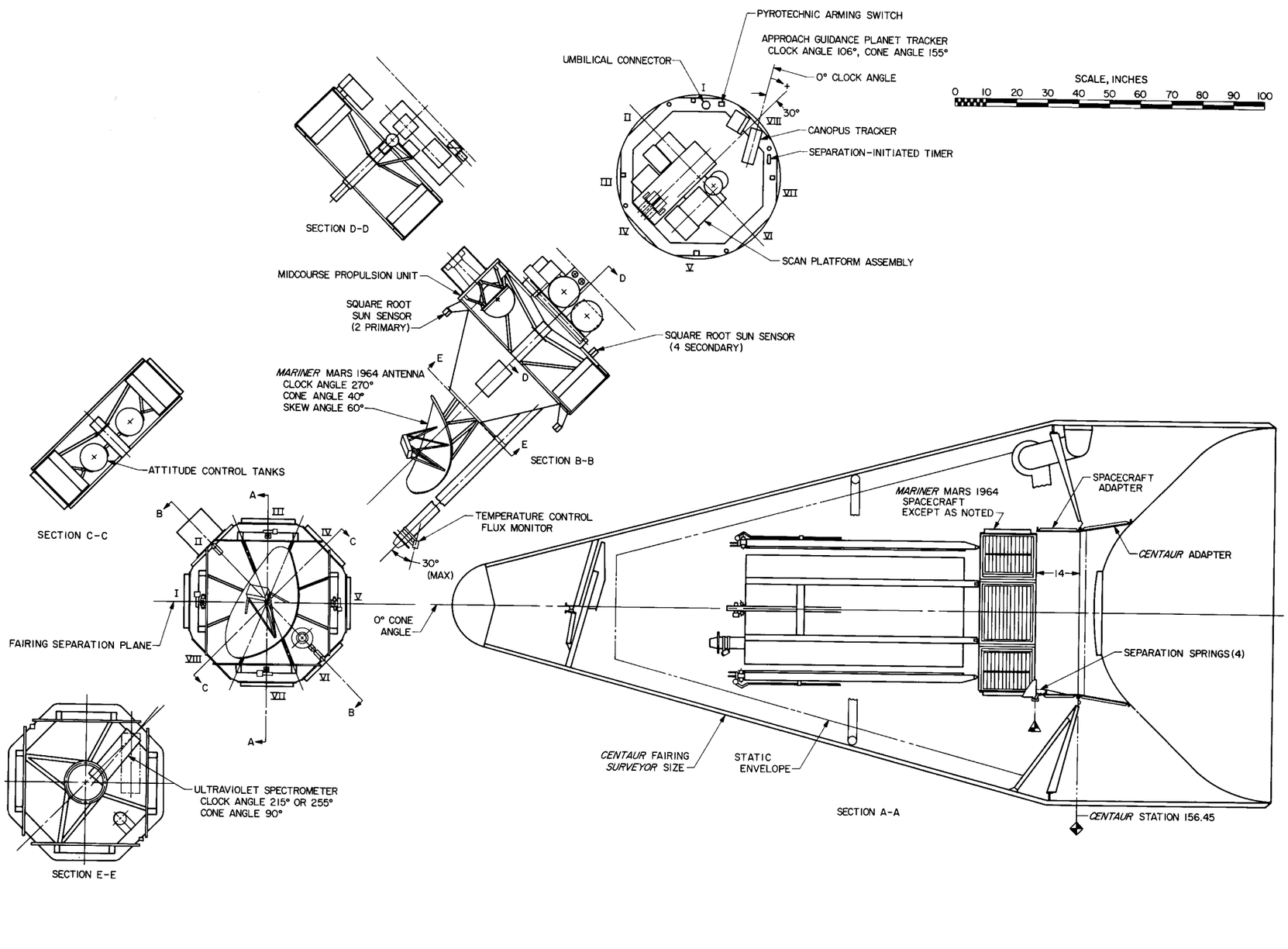

UNCLASSIFIED

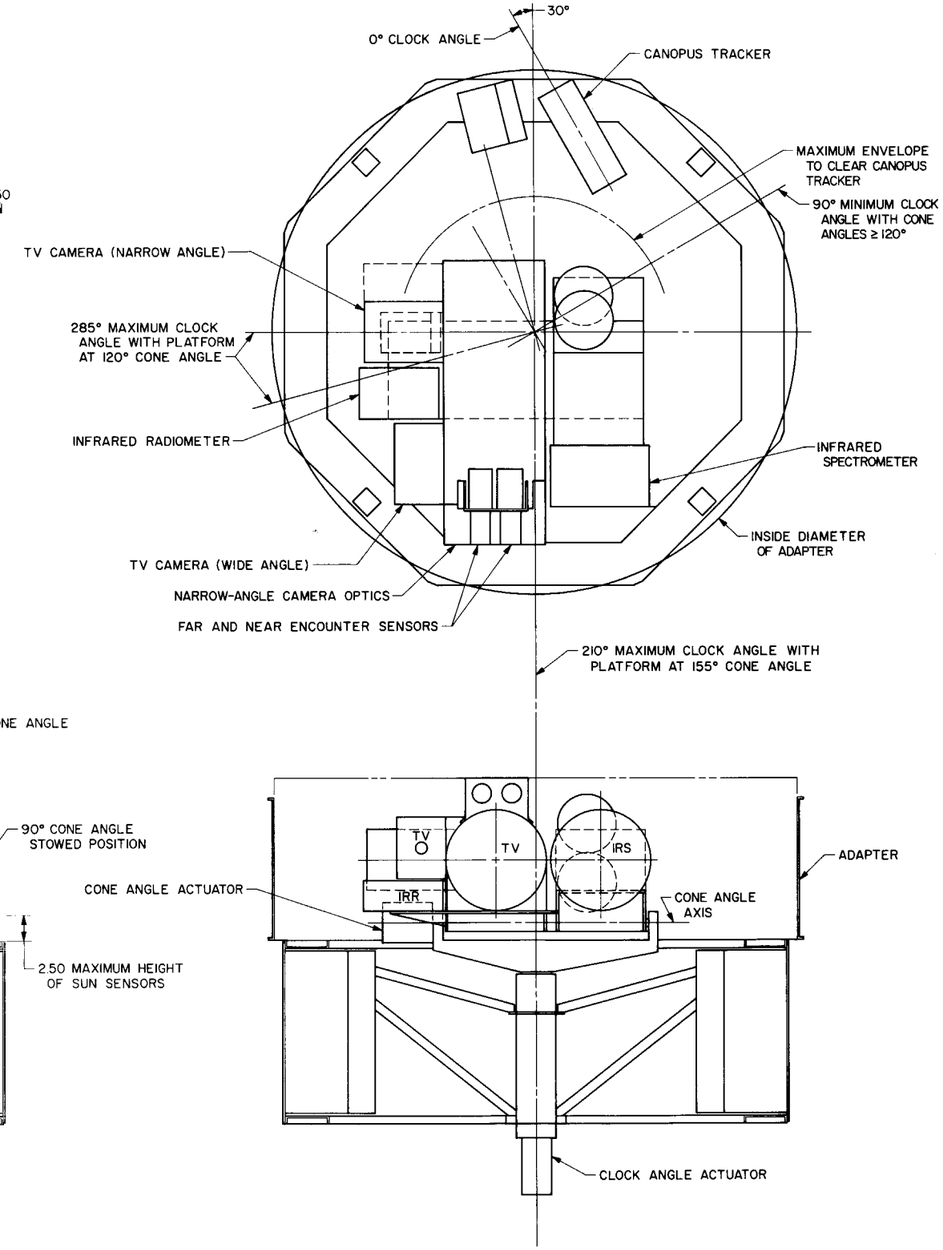

Fig. 5. *Mariner* Mars 1969 spacecraft configuration study

UNCLASSIFIED

UNCLASSIFIED

The *Mariner* Mars
as four distinct seg
compartment, which
for the spacecraft,
craft engineering su
the attitude referer
temperature control
which provides mou
port for the scientifi
actuators to provide
equipment area, wh
spacecraft antennas;
provides the primary
tween the spacecraft
separation devices, a

a. The octagon.

Structure and elec
tronics are housed in
18 in. high and 54
octagon bays contain
tains the propulsion
correction maneuve
cated in a bay that
interactions betwee
panels. The propul
the outboard edge o
inboard) to provide
structural support o

Four of the elec
Mars 1964 electronic
a new packaging co
improved utilization
containing a portion
uses a special conf
servicing problems
requirements with t
are structurally inte
electronic assemblie
on the octagon.

The scan platform
ture to the octagon.
the attitude control
routed to the panel

Subsystem cablin
of each electronic a
and lower system r
is contained in a tr

UNCLAS

UNCLASSIFIED

The *Mariner* Mars 1969 spacecraft can be considered as four distinct segments: (1) the *octagonal electronic compartment*, which is the basic structural building block for the spacecraft, houses the electronics of the spacecraft engineering subsystems and the major portion of the attitude reference and control elements, and the temperature control subsystem; (2) the *scan platform*, which provides mounting locations and subsystem support for the scientific experiments as well as sensors and actuators to provide platform pointing; (3) the *forward equipment area*, which includes the solar panels and spacecraft antennas; and (4) the *adapter section*, which provides the primary interface and transition structure between the spacecraft and launch vehicle, attachment and separation devices, and additional auxiliary equipment.

a. The octagon.

Structure and electronic packaging. The spacecraft electronics are housed in an octagonal structure approximately 18 in. high and 54 in. across the diagonal. Seven of the octagon bays contain electronics. The eighth, Bay II, contains the propulsion subsystem that is used for trajectory correction maneuvers. The propulsion subsystem is located in a bay that is between solar panels to minimize interactions between the motor exhaust plume and the panels. The propulsion subsystem may be mounted on the outboard edge of the octagon (*Mariner* Mars 1964 was inboard) to provide volume internal to the octagon for structural support of the scan platform.

Four of the electronic bays will utilize the *Mariner* Mars 1964 electronic packaging concept. Two bays utilize a new packaging concept (*Mariner* Mars 1969) to provide improved utilization of the available volume. One bay, containing a portion of the power subsystem electronics, uses a special configuration to minimize checkout and servicing problems and to satisfy mechanical interface requirements with the battery. All of the electronic bays are structurally integrated with the octagon such that the electronic assemblies carry a portion of the loads imposed on the octagon.

The scan platform is supported through secondary structure to the octagon. The secondary structure also supports the attitude control gas bottles and plumbing which are routed to the panel hinge line.

Subsystem cabling is located at the inboard surface of each electronic assembly and routed vertically to upper and lower system ring harnesses. The upper ring harness is contained in a trough attached to the upper octagonal ring. Subsystem cabling from the *Mariner* Mars 1964-type assemblies is pigtailed to hard-mounted connectors on the trough. Connections between the upper ring harness and the *Mariner* Mars 1969-type assemblies are through pigtails from the upper ring harness. The lower ring harness is routed about the lower octagonal ring and is connected through pigtails to hard-mounted connectors on each electronic assembly.

Attitude reference and control. The spacecraft celestial references are the Sun and the star Canopus. Nearly spherical coverage for viewing the Sun is provided by Sun sensors on both the top and bottom of the octagon. Sun sensors mounted on pedestals on top of Bays II and VI provide forward hemisphere coverage and four Sun sensors at the base of the spacecraft cover the rear hemisphere. A narrow-angle Sun sensor (3-deg half-angle cone), the Sun gate, is located on the Bay II pedestal and aligned parallel to the Sun line. Its function is to inform the attitude control logic when the Sun is within 3 deg of the roll axis (acquired). The Canopus sensor is located at the base of Bay VIII such that the star is viewed between and fore and aft of the solar panels. The Canopus sensor provides the attitude reference for roll (clock) angles. Clock angle is measured from the centerline of the Canopus sensor clockwise when viewing in the direction of the Sun.

Adjacent to the Canopus sensor, at the base of Bay VIII, is the approach guidance planet sensor and auxiliary Sun sensor. The planet sensor is pointed at a cone and clock angle of 155 and 106 deg, respectively, such that it can view Mars from 10 days ($E - 10$ days) to 1 day ($E - 1$ day) before encounter. A narrow-angle (1.25 deg half-angle cone) auxiliary Sun sensor is located adjacent to the planet sensor and views the Sun through an aperture provided in the octagon. The planet, star, and Sun sensors are grouped such that they should experience similar thermal environments and thereby minimize thermal distortions during the data-gathering period.

The attitude control gas system consists of two mechanically interchangeable units; each is made up of a storage vessel, mounting plate and associated equipment, plumbing and gas jet manifolds. The storage vessels are located in the internal cavity of the octagon. Plumbing is routed through the octagon structure across the panel hinge line, along the panel structure to the gas jet manifolds mounted on the tips of the solar panels. Each unit is a welded system, therefore, installed as an assembly. The jets are located at the tips of the panels to maximize the reaction force moment about the spacecraft center of mass.

UNCLASSIFIED

UNCLASSIFIED

Temperature control. The temperature control approach on the *Mariner* Mars 1969 spacecraft is similar to that of *Mariner* Mars 1964. In a configuration sense this means the spacecraft is shielded from the Sun to isolate this varying heat source, enclosed at the base to minimize heat losses, and bimetallically actuated louvers are mounted on the face of the octagon to regulate the rate of thermal radiation to space. Capability will exist for mounting louvers on each of the seven electronic bays. The scan platform is shielded by a turret enclosure to minimize heat losses from the instruments requiring warmer environment.

b. Scan platform. To achieve the pointing requirements of the scientific instruments, the *Mariner* Mars 1969 spacecraft has a two degrees-of-freedom scan platform, shown in Fig. 5. One axis provides rotational freedom of approximately 200 deg about a line parallel to the spacecraft-Sun line (clock angle). The second axis is normal to the clock axis and provides rotational freedom in cone angle (angle between the Sun line and the pointing direction) of between 90 and 155 deg, i.e., a 65-deg range.

The platform instruments are: two television cameras, infrared radiometer, infrared spectrometer with a gaseous cooling system, and an ultraviolet spectrometer (not shown in Fig. 5). The ultraviolet instrument is only on the clock axis gimbal. The remaining instruments have both degrees-of-freedom. The total scientific instrument weight on the platform is in the 80–90-lb range. Weight estimates of sensors, actuators, structure, etc. bring the total pointable mass to approximately 130 lb. This weight coupled with the volume, cabling, and view-angle requirements of these instruments makes the *Mariner* Mars 1969 platform significantly more complicated than that of *Mariner* Mars 1964 (total weight of 20 lb).

c. Forward equipment.

Solar panels. Current estimates of solar array area requirements for the *Mariner* Mars 1969 mission are in the 70–85-ft^2 range. Approaches to implementing this requirement range from four *Mariner* Mars 1964-type deployable panels, with small additional fixed panels, to larger area deployable panels of a new design. The spacecraft mechanical configuration is shaped to accommodate a *Mariner* Mars 1964 solar panel design and support system (70 ft^2 in four panels supported by viscously damped struts to the superstructure). All feasible solar array approaches will be evaluated as part of the total configuration design.

Antennas. The spacecraft communication antennas are of *Mariner* Mars 1964 design. The low-gain antenna consists of an 88-in. long, 4-in. diameter waveguide that radiates directly through a cruciform-shaped aperture at the tip. It is aligned parallel to the spacecraft roll axis and is mounted, at its base, to the top of the octagon and laterally supported by viscously damped struts from a point approximately one-fourth its length above the octagon to the superstructure. The high-gain antenna parabolic reflector in planform is a 46- × 21.2-in. ellipse. It is supported above the octagon by the superstructure and aligned to transmit data to Earth both before and after the spacecraft encounters the planet. The nominal pointing direction of the high-gain antenna is 40.4 deg in cone angle, 270 deg in clock angle, and 60 deg in skew angle. Skew angle is a measure of the location of the elliptical pattern about the antenna pointing direction.

d. Adapter section and launch vehicle interface. The spacecraft attaches to the launch vehicle through a transition or adapter section. It is part of the spacecraft system and interfaces to the launch vehicle at a bolted field joint and electrical connectors. The spacecraft attaches to the adapters through shoes clamping the corners of the octagon to the adapter in a V-shaped groove. The clamping force is provided by a V-band running circumferentially around the spacecraft at the shoes. Release is provided through pyrotechnically actuated devices in the V-band. A separation impulse is provided to the spacecraft from the adapter by spring-driven pistons in alternate corners of the octagon. The adapter also provides surfaces for mounting umbilical and separation cables and connectors and pads for securing separation-initiated devices.

The spacecraft is shaped to fit within the envelope provided by the *Centaur* nose fairing which is a cone approximately 120 in. in diameter and 190 in. long. The spacecraft nose fairing clearances allow for the dynamic environment of boost, and for the clamshell separation of the nose fairing.

The foregoing is a cursory description of the *Mariner* Mars 1969 spacecraft. The most significant departure in the configuration from the *Mariner* Mars 1964 design is the complexity of the scan platform. Additional study is required in this area as well as in the solar array configuration and the interface with the *Centaur*.

3. Structure Subsystem

The *Mariner* Mars 1969 spacecraft structural design will be similar to that of the *Mariner* Mars 1964 spacecraft with modifications being made only as necessary to meet new load requirements peculiar to the 1969 Mars mission. The spacecraft structure will be considered in its major

UNCLASSIFIED

UNCLASSIFIED

subelements: the basic octagonal bus, packaging structures, scan platform support structure within the octagon, superstructure truss work on top of the octagon, solar panel structures, and antenna structures. Each subelement will be examined for use without change from the *Mariner* Mars 1964 design, and a minimum modification will be made to strengthen the elements as necessary.

The *Mariner* Mars 1969 spacecraft will be approximately 40% heavier than *Mariner* Mars 1964 with much of the additional weight being concentrated onto a greatly enlarged scan platform. The general weight increase will be reflected in heavier basic octagon members, while the heavier scan platform will require a new scan platform support structure, and a more elaborate scan platform latching scheme. It is presently anticipated that no significant change will be made to the antenna structures and that modification of the solar panel structures will be contingent upon a need for solar panels larger than those of *Mariner* Mars 1964. The superstructure design will change to accommodate new high-gain antenna pointing directions; however, finalization of the superstructure design will be contingent upon the support scheme chosen for the solar panels. The electronic packaging for *Mariner* Mars 1969 will in some areas be essentially the same as for *Mariner* Mars 1964. Other areas, however, are to be redesigned and packaged in a new way, as described below.

Historically, electronic equipment has been packaged in "black boxes" with structures only stiff enough to support the items within, and these assemblies were then attached to some type of supporting structure. The JPL approach has been to integrate the electronic equipment structure with the support structure, thus affecting a more efficient utilization of space and weight. The *Mariner* Mars 1969 electronic equipment is being designed in accordance with this integrated structure concept.

The spacecraft structure contains removable and replaceable electronic assemblies that are generally of standardized size and shape in order to provide system design flexibility. The assemblies contain standardized subassembly chassis to allow for interchangeability. The electronic assemblies are located in seven sections of the spacecraft octagonal electronics compartment. The eighth section is reserved primarily for the midcourse rocket motor.

The electronic packaging design concept requires that electronic assemblies form an integral part of the spacecraft structure. Subassembly structures are mechanically integrated into the assembly chassis and the assembly chassis integrated to the spacecraft structure. The electronics are protected from excessive loading by dynamic decoupling. The subassemblies have resonant frequencies above 400 cps, while the assembly resonant frequency is designed to be above 350 cps. Two standard assembly designs are utilized on the *Mariner* Mars 1969 spacecraft. The electronic assembly configuration and geometry conform to the *Mariner* Mars 1964 configuration, as shown in Fig. 6, for *Mariner* Mars 1964-type equipment. The second type of standard assembly configuration is shown in Fig. 7. Within an assembly, the subassembly profile is standardized to facilitate location flexibility. To optimize design and to reduce interconnections, two profile standards are utilized in the configuration shown in Fig. 7, and subassembly thickness is varied as required to satisfy the particular equipment design requirements and packaging techniques.

A reevaluation of the trade-offs associated with the *Mariner* Mars 1964 packaging configuration led to the new design (Fig. 7). The *Mariner* Mars 1964 configuration required access to the spacecraft inboard side of the assembly for removal of the assembly and the subassemblies. In some instances the inboard access was sufficient so that an individual subassembly could be removed; in other instances the entire assembly had to be removed to permit subassembly removal. Another undesirable feature of the *Mariner* Mars 1964 design is the required flexing of the assembly harness when installing and removing subassemblies. The new design allows access to each subassembly from the spacecraft outboard side, but there is a limitation to the accessibility. Threaded fasteners are required between the assembly and subassemblies on the inboard side for dynamic stability and thermal control; however, it is anticipated that these fasteners will not be installed at the times when subassembly access is most often required. The assembly mounting hardware is also accessible from outboard the spacecraft, thereby facilitating the removal of an entire assembly. The use of a rack and panel connector configuration allows the assembly harness to be hard-mounted, thus improving reliability. Another benefit is a lessening of the dynamic response of the subassemblies since they are fastened to shear panels on both the inboard and outboard sides.

The major problems associated with the new design are well documented since a similar configuration was under development for the *Mariner B* program (flyby missions to Mars and Venus in 1964–66) prior to its cancellation. The problems are all related to the high (½ lb max.) insertion and withdrawal forces associated with the flight-qualified connector contacts. A subchassis

UNCLASSIFIED

UNCLASSIFIED

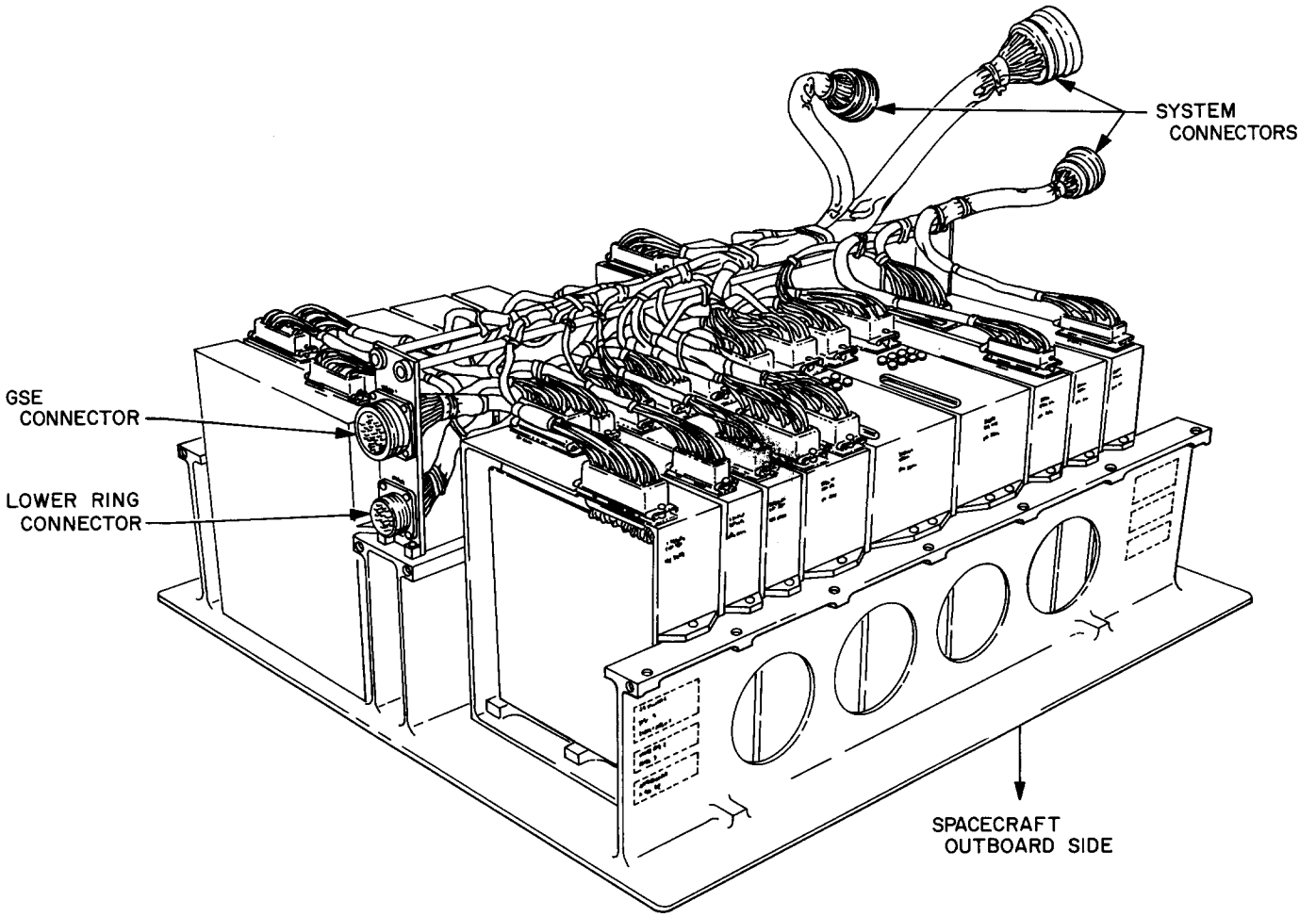

Fig. 6. Typical *Mariner* Mars 1964-type assembly

UNCLASSIFIED

UNCLASSIFIED

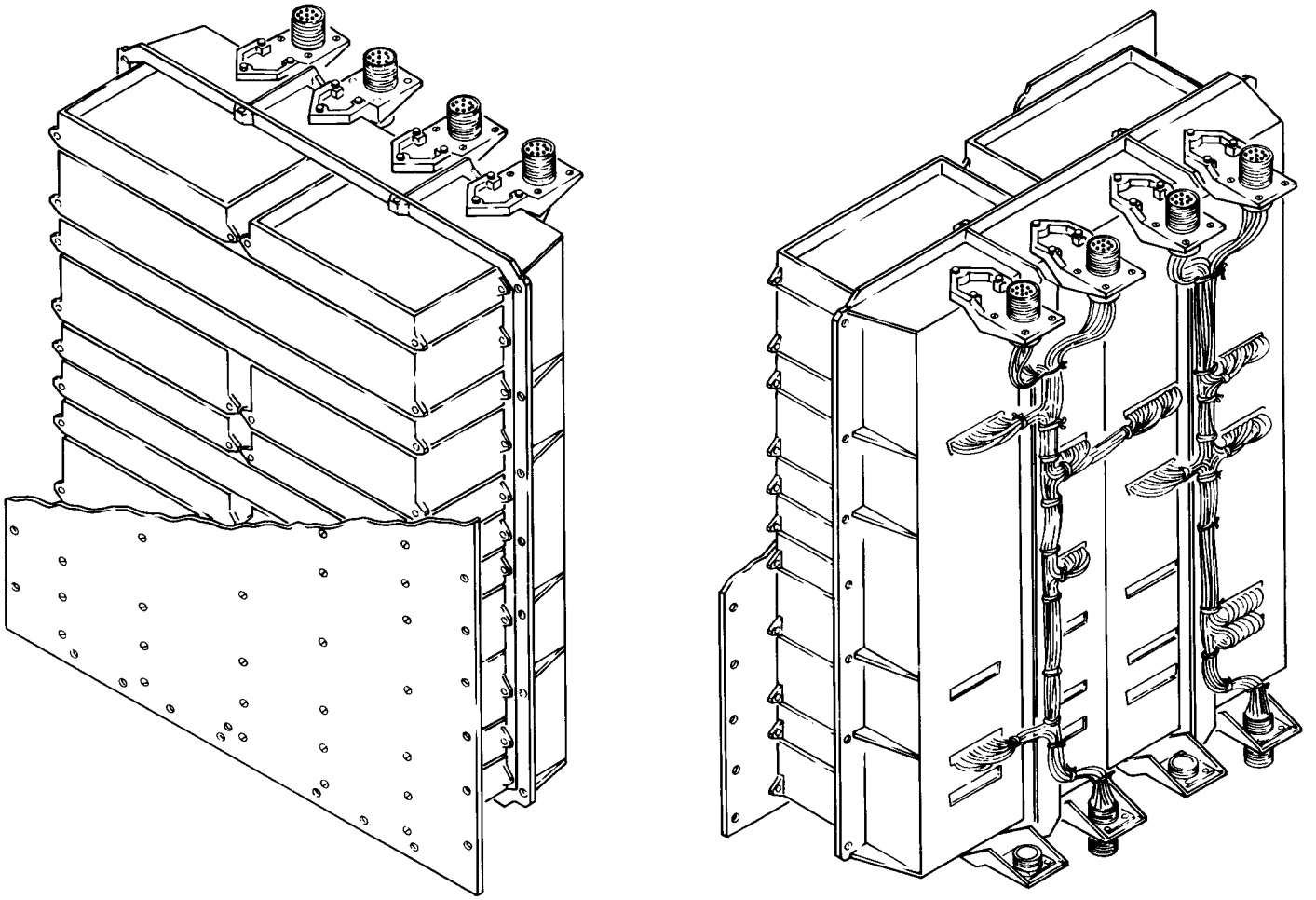

Fig. 7. Typical *Mariner* Mars 1969-type assembly

UNCLASSIFIED

UNCLASSIFIED

could contain as many as 350 contacts, yielding insertion and withdrawal forces as high as 175 lb. The chassis harness support is designed to also function as a stiffener to prevent chassis deflection due to the subassembly insertion load. Tooling is being designed to extract the subassemblies. It was discovered on *Mariner B* that the connector shells tend to deflect when mated, rack and panel fashion. Apparently, the difference in rack and panel mating and mating connectors by hand is that in the latter case a slight cocking action occurs which prevents the full insertion load from being developed. The problem is being remedied by two possible solutions: (1) the connector mounting configuration will provide optimum support for the connector shell; and (2) improved connector shell materials are being investigated.

Although the *Mariner* Mars 1964 packaging configuration has proved quite successful, it is felt that the new configuration will be an improvement in reliability and will facilitate spacecraft checkout. However, additional testing and analysis is still required and will continue.

4. Cabling Subsystem

In most of the *Mariner* Mars 1969 electronic bays and for the spacecraft ring harness, the basic *Mariner* Mars 1964 cabling philosophies (Fig. 8) will be utilized. For the remaining bays, a new electronic assembly concept is being utilized, in which the subassemblies are plugged into the assembly chassis. Cabling of the subassembly interconnections for the bays that utilize the plug-in subassembly concept, although functionally similar to the *Mariner* Mars 1964 and *Mariner* Venus 67 harnesses, requires some new design and fabrication techniques.

Although the over-all height for the electronic assembly and cabling remains the same, the deeper electronic assembly chassis will require harnesses which are closer to the mounting surface of the assembly. This requires replacing the bracket locating the Bendix connectors, which mate with those on the ring harnesses, with shorter individual brackets (Fig. 9) that spread the connectors across the width of the assembly chassis at either end of the chassis.

Connector brackets of two different designs will be used; one is designed to use the full 1-in. edge distance allocated in the packaging design for mounting these brackets. The alternate design, which mounts in ½ in. of the edge distance, will be used only if there is congestion around the mounting area and a need for clearance space for soldering as well as other fabrication or installation processes.

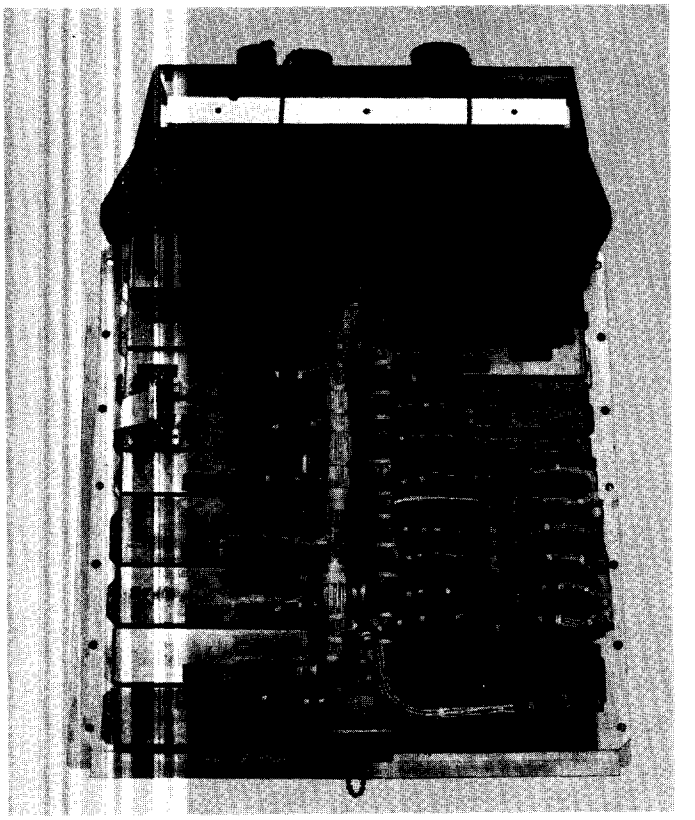

Fig. 8. *Mariner* Mars 1964 typical flight harness on fabrication fixture

The tubular brackets used on *Mariner* Mars 1964 and *Mariner* Venus 67 as cable mounts have also been eliminated from this assembly. The stiffeners of the assembly chassis will be used for mounting cables. Harness mounting will be accomplished with plastic cable wraps through rectangular holes in the stiffeners. The wire bundle will be wrapped with insulating strips under the cable wraps to prevent wire damage. Replacement of potting with shrink sleeving is presently contemplated. Preliminary testing indicates that a double sleeving arrangement provides five to ten times more flex life over wires potted as on *Mariner* Mars 1964. This testing was done by using only one type (CRN) of shrink tubing and varying the extension of the inner tube past the outer one. Further testing will compare various materials and techniques. Presently, sealing of the contact at the point of entry into the connector insert is the only problem preventing a firm recommendation of this method of back-sealing connectors.

Several methods of providing float in the harness rack and panel connectors are under investigation. This float is necessary to accommodate tolerances in positioning the

UNCLASSIFIED

UNCLASSIFIED

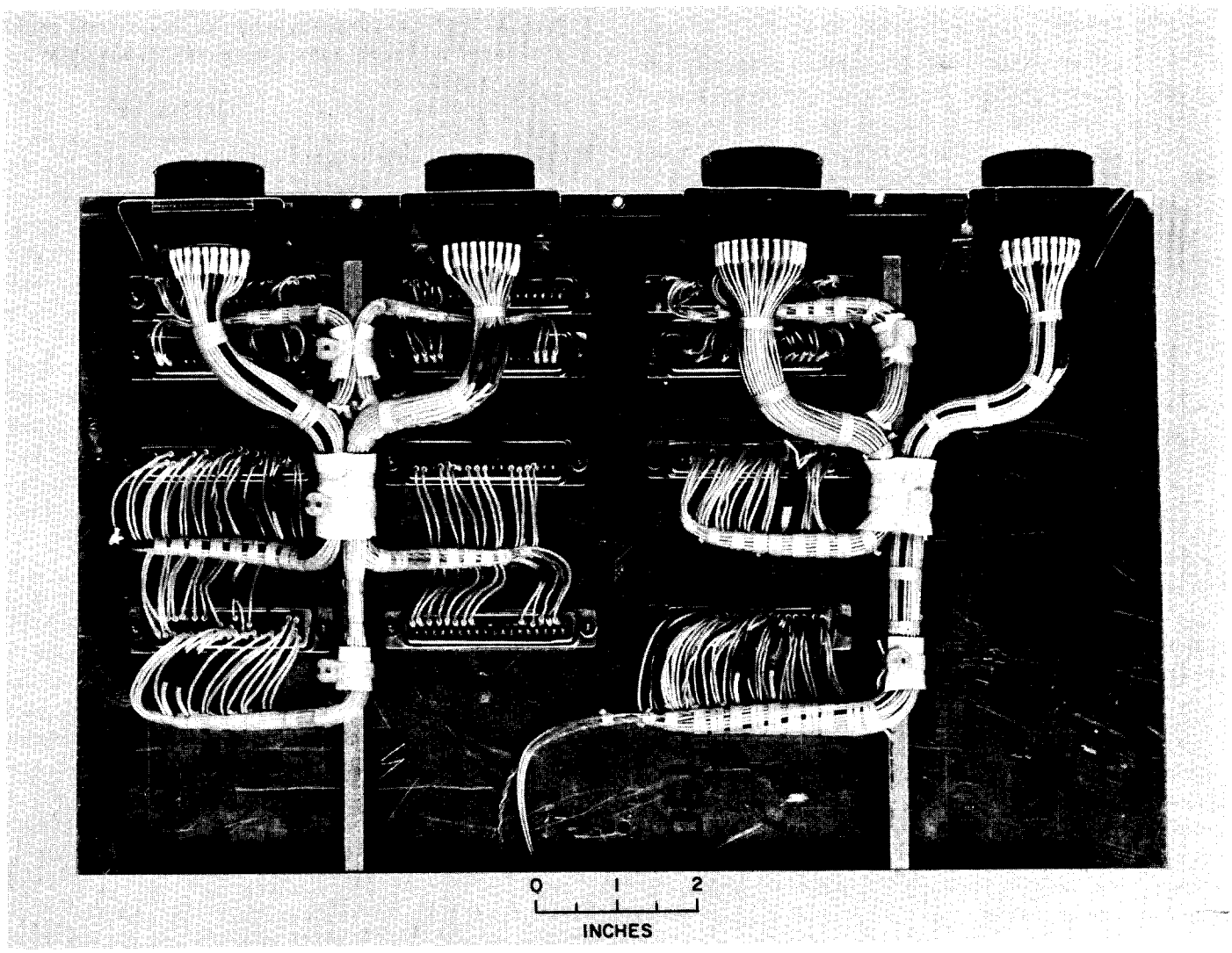

Fig. 9. *Mariner* Mars 1969 simulated harness on assembly chassis mock-up

hard-mounted connectors in the plug-in subassemblies. Guide pins may not be necessary except for alignment of subassemblies in the chassis with connector alignment accomplished by the polarized shells. Tests and evaluation will determine whether the polarized shells are sufficient to provide alignment under worst-case conditions, or whether each pair of mating connectors will require alignment pins.

It is believed that the "individual harnesses for each subsystem in each bay" constraint can be met without serious problems. However, the individual harnesses will be much more readily separated than on *Mariner* Mars 1964, where string ties were cut and circular connectors were removed from the brackets to separate two harnesses mounted on the same tubular bracket.

Standoff posts will be inserted between the chassis and the harness to support the wire groups where required by excessive length of breakouts from the main wire bundle to the connectors. Cable clamps will be used to attach the harness to the standoffs. The subminiature rack and panel connectors may be replaced by the Amphenol equivalent, which is interchangeable and may be mated with rack and panel connectors. Tests of this connector indicate that it is as good as, or better than, the "D"-type connectors in many respects.

Various makes of splices, shrink sleeving, shield terminations, insulating sleeving, and cable mounting wraps are under investigation to determine which offers the greatest advantage.

UNCLASSIFIED

UNCLASSIFIED

5. Temperature Control Subsystem

The *Mariner* Mars 1969 temperature control subsystem has been defined to encompass a more limited scope than has been used on previous *Mariner* projects. Previously, the temperature control subsystem activities included the spacecraft temperature control design as well as the deliverable hardware items required to implement the design. For *Mariner* Mars 1969 these two functions have been separated, primarily for contracting convenience, and the temperature control subsystem is now limited to the hardware activities. Where possible, the spacecraft temperature control requirements will be included in the thermal design of each part of the spacecraft. Only the hardware that is predominately for temperature control purposes constitutes this subsystem.

The thermal design of the spacecraft is still preliminary, but it appears at this time that the temperature control hardware will consist mainly of louver assemblies and thermal shields. It may be necessary later to include some more specialized items such as electrical or radioisotope heaters, paints with particular optical properties, or special low-conduction joints.

The louver assemblies will be essentially the same, and will be interchangeable with those used on *Mariner IV*. This will permit reuse of much of the test hardware. Two minor changes are planned: (1) the removal of the telemetry louver position indicator, and (2) the addition of an optional provision for limiting the angle to which the louver is allowed to open.

The use of multilayered insulation blankets and polished aluminum bolt-on thermal shields will also be similar to those previously used. The detail design of some of the shields will be retained, but the majority of the details of these items will be changed. This is a reflection of changes in the power distribution within the spacecraft and the geometry of the upper and lower surfaces of the bus.

A temperature control flux monitor (TCFM) is also included as part of the temperature control subsystem. It was developed to help resolve some of the difficulties experienced previously by not knowing the absolute value of the solar flux intercepted by the spacecraft. Errors of the order of 10 to 15% were experienced on the first *Mariner* flight to Mars, resulting in temperature variations as much as 30°F from predictions. The TCFM appears to be capable of measurements with an absolute error less than 1.5%. Laboratory models of the instrument have been fabricated and tested, and are presently used as the primary reference radiometer during temperature control testing in the JPL solar simulators.

6. Mechanical Devices Subsystem

The *Mariner* Mars 1969 spacecraft mechanical devices will be similar in design to those of *Mariner* Mars 1964 wherever parallel functional requirements exist. In cases where device requirements are similar, but enough changed to require new design, the *Mariner* Mars 1964 conceptual approach will be incorporated into the new hardware. The mechanical devices on *Mariner* Mars 1969 will be: low-gain antenna dampers, solar panel boost dampers, solar panel cruise dampers, solar panel actuators and open switches, pyrotechnic arming switch (PAS), separation-initiated timer (SIT), planet scan platform, scan platform latch system, and possibly scan platform resonance control system.

The *Mariner* Mars 1969 damper designs will be conceptually similar to the equivalent *Mariner* Mars 1964 designs; however, hardware details will be different with the possible exception being the cruise dampers. The solar panel actuators, SIT, and PAS are expected to remain unchanged except for the addition of a thermal expansion compensator to the SIT, a minor modification. The major mechanical device redesign will be made on the planet scan platform. It is anticipated that the *Mariner* Mars 1969 platform will provide two degrees (clock and cone) of scan freedom and will mount approximately 80 lb of scientific instruments. The most severe platform resonances may have to be controlled during launch. If it proves necessary, a scan platform resonance control system will be designed and most likely incorporated into the scan platform latch system.

E. Guidance and Control

1. Gyro Control Subassembly

The gyro control subassembly for the *Mariner* Mars 1969 Project will employ essentially the same system as was used on the *Mariner* Mars 1964 spacecraft. Based upon experience gained from that program, however, some improvements have been instituted. These are of such a nature as to increase the reliability of the system

UNCLASSIFIED

UNCLASSIFIED
CONFIDENTIAL

rather than functional changes to improve its performance or efficiency.

To accommodate the long lead times involved, procurement of gyros was initiated prior to award of the attitude control subsystem contract. A complete buy of 24 miniature floated rate integrating gyros, P/N 2565001, has been negotiated with Kearfott Systems Division of General Precision, Inc. These devices are a repeat of the *Mariner* Mars 1964 choice in keeping with the Project Office directive to incorporate "...maximum utilization of the *Mariner* Mars 1964 design." However, much tighter control has been placed upon the allowable internal contamination and on the assembly procedures. In this way, it is anticipated that the number of rejectable units will decrease and the probability of success of each gyro will greatly increase.

Changes which have been proposed in the gyro electronics are minimal. The over-all assembly dimensions have been changed somewhat to accommodate the spacecraft Case VII location redesign. These changes have allowed repackaging of three of the electronics modules to increase their size slightly, thereby reducing the density now present in them. The result will be to reduce the probability of error during assembly and to relieve local heating problems within the module. One module is being redesigned to include critical portions of the other two. This will reduce the problems experienced in the past, due to electrical pickup in critical areas.

References

1. Chernosky, E. J., and Hagan, M. P., "The Zurich Sunspot Number and its Variation for 1700–1957," *Journal of Geophysical Research*, Vol. 63, No. 4, pp. 775–788, December 1958.

2. Weddell, J. B., and Haffner, J. W., "Statistical Evaluation of Proton Radiation from Solar Flares," Final Technical Report (JPL Contract 951243), NAA-S & ID, Downey, California, May 20, 1966.

3. King-Hele, D. G., "Prediction of the Dates and Intensities of the Next Two Sunspot Maxima," *Nature*, Vol. 209, pp. 285–286, January 15, 1966.

4. Minnis, C. M., "An Estimate of the Peak Sunspot Number in 1968," *Nature*, Vol. 186, pp. 462, May 7, 1960.

5. Jose, P. D., "Sun's Motion and Sunspots," *The Astronomical Journal*, Vol. 70, No. 3, pp. 193–199, April 1965.

6. Webber, W. R., "An Evaluation of the Radiation Hazard Due to Solar Particle Events," D2-90469, The Boeing Company, Seattle, Washington, December 1963.

7. McDonald, F. B., Ed., "Solar Proton Manual," NASA TR-R-169, Goddard Space Flight Center, NASA, Washington, D.C., December 1963.

8. Hess, W. N., Ed., "The Physics of Solar Flares," (AAS-NASA Symposium) NASA SP-50 Proceedings held at Goddard Space Flight Center, Greenbelt, Maryland, October 28–30, 1963, pp. 215–256, NASA, Washington, D.C., 1964.

9. Ogilvie, K. W., Bryant, D. S., and Davis, L. R., "Rocket Observations of Solar Protons During the November 1960 Events, 1," *Journal of Geophysical Research*, Vol. 67, No. 3, pp. 929–937, March 1962.

UNCLASSIFIED
CONFIDENTIAL

UNCLASSIFIED

References (Cont'd)

10. Lin, W. C., and Van Allen, J. A., "Observation of Solar Cosmic Rays from October 13, 1959 to February 17, 1961 with *Explorer VII*," *Proceedings of the International School of Physics*, Enrico Fermi Course XXIV, Space Exploration and the Solar System, Academic Press, New York and London, pp. 194–225, 1964.

11. Masley, A. J., and Geodeke, A. D., "Complete Dose Analysis of the November 12, 1960 Solar Cosmic Ray Event," COSPAR, *Life Sciences and Space Research*, pp. 45–109, 1963.

12. Foelsche, T., "Estimates of Radiation Doses in Space on the Basis of Current Data," COSPAR, *Life Sciences and Space Research*, pp. 48–94, 1963.

13. Ney, E. P., and Stein, W. A., "Solar Protons, Alpha Particles, and Heavy Nuclei in November 1960," *Journal of Geophysical Research*, Vol. 67, No. 6, pp. 2087–2105, June 1962.

14. Walker, H. M., and Lev, J., "Statistical Inference," Holt, Rinehard, and Winston, New York, 1953.

UNCLASSIFIED

UNCLASSIFIED

III. *Voyager* Project

A. Introduction

1. Project Objectives

The primary objective of the *Voyager* Project is to carry out scientific investigations of the solar system by instrumented, unmanned spacecraft which will fly by, orbit, and/or land on the planets. Emphasis will be placed on the acquisition of scientific information relevant to the origin and evolution of the solar system and the origin, evolution, and nature of life; and the application of this information to an understanding of terrestrial life. The primary objective of the *Voyager* missions to Mars beginning in 1973 is to obtain information relative to the existence and nature of extraterrestrial life; the atmospheric, surface, and body characteristics of Mars; and the planetary environment by performing unmanned experiments on the surface of, and in orbit about, the planet. A secondary objective is to further our knowledge of the interplanetary medium between the planets Earth and Mars by obtaining scientific and engineering measurements while the spacecraft is in transit.

2. Project Plan

All *Voyager* missions will be conducted as events of an integrated program in which each individual flight forms a part of a logical sequence in an over-all technical plan of both lander and orbital operations. The *Voyager* design will provide for the transport of large scientific payloads to the planet, the telemetering of a large volume of data back to Earth, and long useful lifetimes in orbit about the planet and/or on the planetary surface. Hardware will be designed to accommodate a variety of spacecraft and/or capsule science payloads, mission profiles, and trajectories. Particular emphasis will be given to simple and conservative designs; redundancy wherever appropriate; and a comprehensive program of component, subsystem, and system testing.

Since no deep space flight tests of the flight spacecraft are planned, compensation will be made by additional ground tests conducted to the extent possible. During the test program for the flight capsule, which is planned to include Earth-entry flight tests, entry dynamics will be investigated.

Over-all direction and evaluation of the *Voyager* Project is the responsibility of the NASA Office of Space Science and Applications (OSSA). The project's management and the implementation of selected systems are the responsibilities of JPL.

3. Technical Description of Vehicles

Two *Voyager* planetary vehicles are to be designed, constructed, and tested for launch, using a single *Saturn V*

CONFIDENTIAL
UNCLASSIFIED

UNCLASSIFIED

launch vehicle, during the 1973 Mars opportunity. Attention is also being given to requirements imposed on such vehicles by launches subsequent to 1973, such as a similar mission planned for 1975. Each planetary vehicle is to consist of a flight spacecraft and a flight capsule, with science experiments conducted both from the orbiter and on the planetary surface for the 1973 mission. The flight spacecraft, with several hundred pounds of science payload, will weigh approximately 2500 lb; its retropropulsion subsystem may, in addition, weigh up to 15,000 lb; and the flight capsule will weigh 3000 lb or less. The flight spacecraft will be a fully attitude-stabilized device utilizing celestial references for the cruise phase. Velocity increments for midcourse trajectory corrections and for Mars orbit attainment by both the flight spacecraft and flight capsule will be provided. On-board sequencing and logic and ground command capability will also be provided. The flight spacecraft will supply its own power from solar energy or from internal sources and will be capable of maintaining radio communications with Earth. In addition, the flight spacecraft will be thermally integrated and stabilized. Data concerning various scientific phenomena near Mars and during transit and those concerning spacecraft performance will be monitored and telemetered to Earth.

The flight spacecraft will also provide the flight capsule with services such as power, timing and sequencing, telemetry, and command during the transit portion of the missions and may also serve as a communications relay. The sterilized flight capsule will be designed for separation from the flight spacecraft in orbit, attainment of a Mars impact trajectory, entry into the Martian atmosphere, descent to the surface, impact survival and surface lifetimes of 2 days in 1973. Later goals for surface lifetimes are as much as 6 mo. The flight capsule will contain the power, guidance, control, communications, and data handling systems necessary to complete its mission.

B. Guidance and Control

1. A Proposed Attitude-Control Subsystem

a. Introduction. Presented here are the results of a preliminary study to determine the feasibility of and basic requirements for a proposed *Voyager* spacecraft attitude-control subsystem. These results are based on an analysis of the roll-axis attitude-control subsystem. However, a large portion of the analysis is applicable to the pitch- and yaw-axis attitude-control subsystems since their basic configurations are the same.

The two essential differences between the method of attitude control described in this article and the method used on previous spacecraft, such as the *Ranger* and *Mariner* Mars 1964 spacecraft, are the following: (1) application of a wide-angle position gyro, and (2) the commanded turn configuration. In the past, narrow-angle high-gain rate-integrating gyros were used. These configurations necessitated the use of very large feedback capacitors (4000-μf) to derive position information during commanded turns.

The method of attitude control using the wide-angle position gyro described here provides the following distinct advantages over previous methods:

(1) During acquisition, the wide-angle gyro is caged in the rate mode with the Canopus tracker signal fed into the gyro torquer. No additional compensation is required to obtain suitable rate-plus-position control. The rate-to-position gain during this mode is a function of the gyro torquer gain, gyro angular momentum, and the Canopus tracker scale factor. Derived rate, although not required for acquisition, provides additional rate damping, which further improves attitude-control subsystem response during acquisition.

(2) Prior to initiating a commanded turn, the gyro is caged in the rate mode. Since the Canopus tracker is connected to the gyro torquer, the gyro gimbal offset angle corresponds to the Canopus sensor position error. Hence, the accuracy of a commanded turn is increased since the initial conditions for the gyro have been precisely determined.

(3) During a commanded turn, the gyro is in a position mode. No additional compensation, other than derived rate, is required for rate control.

The only requirement that must be met for the wide-angle gyro is the need for active temperature control due to this gyro's higher sensitivity to the temperature environment.

b. Roll-axis attitude-control subsystem configuration. The basic configuration for the roll-axis attitude-control subsystem is shown in Fig. 1. This mechanization consists of a wide-angle position gyro connected in a rate mode (caged; i.e., gyro output fed back to torquer). The gyro

UNCLASSIFIED

UNCLASSIFIED

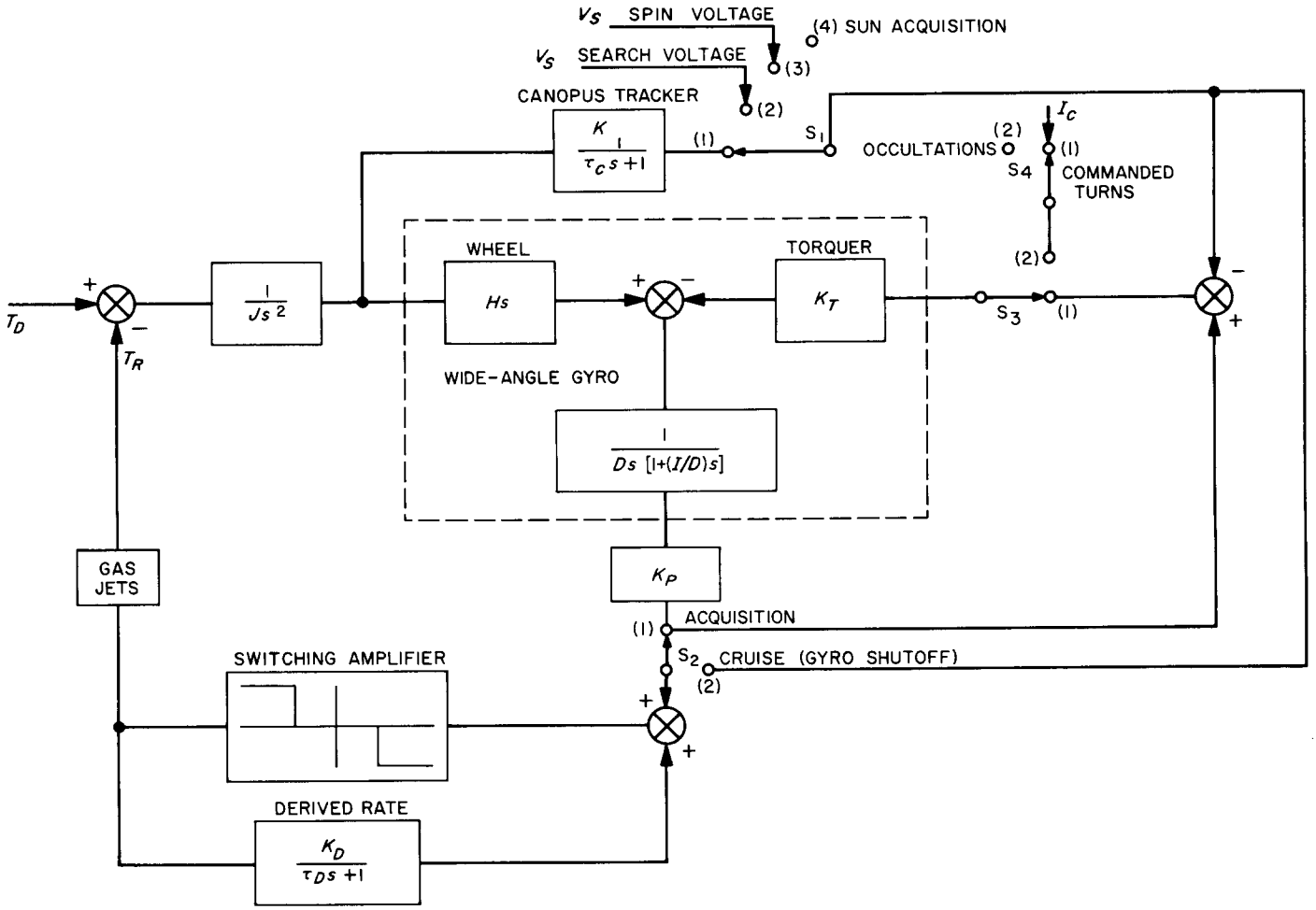

Fig. 1. Basic configuration of roll-axis attitude-control subsystem

output signal is summed with the derived rate signal as an input to a switching amplifier. The switching amplifier, with a deadband, activates a cold-gas system in an *on, off* mode of operation for control torques to provide constant acceleration.

The switches S_1, S_2, S_3, and S_4 shown in Fig. 1 are intended to show the functional switching within the control system during the various operating modes. A description of the control system operation is given below.

Canopus acquisition. In addition to the gyro output, several other signals are fed into the gyro torquer. This switching function is represented by switch S_1 in Fig. 1. During Sun acquisition, S_1 is in position (4), so that the gyro output signal represents pure rate.

$$\frac{V_o}{\dot{\theta}_R} = \frac{H}{K_T(\tau s + 1)}, \qquad (1)$$

where

$$\tau = \frac{D}{K_P K_T},$$

and the gyro time constant I/D is neglected.

After completion of Sun acquisition, S_1 switches to position (3), connecting a spin voltage to the gyro torquer for magnetometer calibration. The gyro output signal is now a rate signal biased by the spin voltage V_S. The spacecraft is then maintained at a constant roll rate corresponding to V_S.

At completion of the magnetometer spin mode, S_1 switches to position (2), connecting a search voltage to the gyro torquer. This mode is identical to the spin mode in that the gyro output signal is again biased by V_S and

UNCLASSIFIED

UNCLASSIFIED

the spacecraft is maintained at a constant roll search rate (equal to the spin rate).

$$V_o = \frac{[\dot{\theta}_R(H/K_T) - V_S]}{(\tau s + 1)} . \quad (2)$$

Upon receiving a Canopus acquisition signal, S_1 switches to position (1), connecting the Canopus sensor output to the gyro torquer. The gyro output signal is now proportional to rate plus position.

$$\frac{V_o}{\theta_R} = \frac{K_{S_1}(k\tau s + 1)}{(\tau s + 1)} , \quad (3)$$

where

$$\tau = D/K_P K_T ,$$

$$k = HK_P/DK_{S_1} ,$$

and the Canopus tracker time constant τ_1 has been neglected to more readily show the form of the gyro output signal.

After receipt of the Canopus acquisition signal, the vehicle remains on gyro rate-plus-position control (all axes) for 180 sec (a nominal value), at which time the gyros are shut off and the system switches into the cruise mode

Cruise mode. At completion of the Canopus acquisition mode, switch S_2 moves to position (2), gyro shutoff, connecting the Canopus tracker signal to the switching amplifier (Fig. 1). Rate damping is provided by derived rate feedback around the switching amplifier. The system continues in this mode until the first midcourse maneuver.

Inertial hold mode for commanded turns. Prior to initiating a commanded turn, the gyro's motors are "run up" and stabilized. Referring to Fig. 1, the gyro is still connected in the rate-plus-position configuration. The gyro gimbal offset angle then corresponds to the Canopus sensor position error. Hence, the initial conditions on the gyro (assuming very low rates in cruise) are precisely determined prior to initiating a commanded turn.

After gyro run-up and stabilization, the system is prepared for the inertial hold mode. Upon receipt of the roll inertial hold command, switch S_2 moves to position (1), connecting the gyro output to the switching amplifier, and switch S_3 moves to position (2). The gyro output is now a biased position signal corresponding to the product of the commanded turn current I_C and the length of time it is applied.

Since the gyro is uncaged and in a position mode, rate compensation is achieved with derived rate feedback. The derived rate parameters (discussed later) are optimized for commanded turns.

After completion of the midcourse maneuver, the inertial hold command is removed and reacquisition begins.

Canopus reacquisition. The Canopus reacquisition mode is identical to the initial acquisition mode, with the exception that the roll spin mode is disabled.

Orbit insertions and orbit trims. The orbit insertion and orbit trim mode of operation is identical to the inertial hold mode for commanded turns.

Orbital mode with and without occultations. When occultations are anticipated, the occultation mode command is given; this places the gyro (all axes) on rate-plus-position control and energizes the Sun and Canopus occultation sensors. When Canopus occultation is detected, the roll-axis gyro is placed in the inertial hold mode with switch S_4 in position (2). The gyro output now represents pure position.

$$\frac{V_o}{\theta_R} = \frac{HK_P}{D} . \quad (4)$$

Rate compensation is accomplished with derived rate. When the occultation sensors detect the end of occultation, the normal reacquisition sequence is initiated.

When no Canopus occultations are anticipated, the orbital mode of operation is identical to the cruise mode.

c. Analysis

Acquisition modes. The gyro configuration during Canopus acquisition is shown in Fig. 2. The gyro output signal V_o is related to the roll error position signal θ_R as follows:

$$V_o = \left[Hs\theta_R - K_T \left(V_o - \frac{\theta_R K_{S_1}}{\tau_c s + 1} \right) \right] \frac{K_P}{Is^2 + Ds} . \quad (5)$$

After simplification,

$$\frac{V_o}{\theta_R} = \frac{K_P H}{I} \left[\frac{s^2 + \frac{1}{\tau_c} s + \frac{K_T K_{S_1}}{H \tau_c}}{\left(s + \frac{1}{\tau_c} \right) \left(s^2 + \frac{D}{I} s + \frac{K_T K_P}{I} \right)} \right] , \quad (6)$$

where I = gimbal output axis inertia = 250 g-cm^2, and K_P = gyro pickoff scale factor and output amplifier

UNCLASSIFIED

UNCLASSIFIED

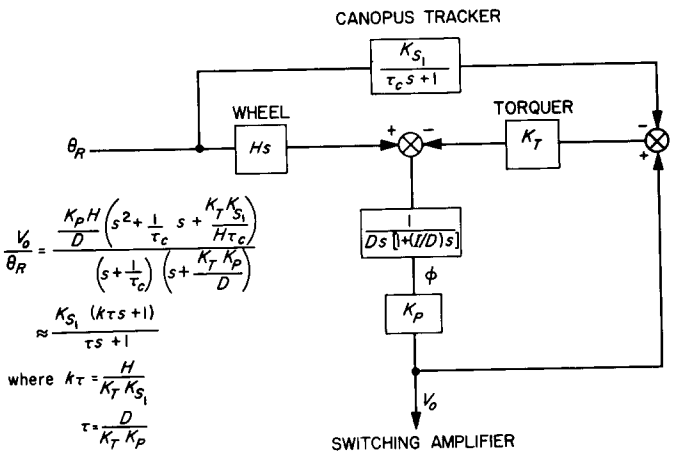

Fig. 2. Gyro and Canopus tracker configuration during Canopus acquisition

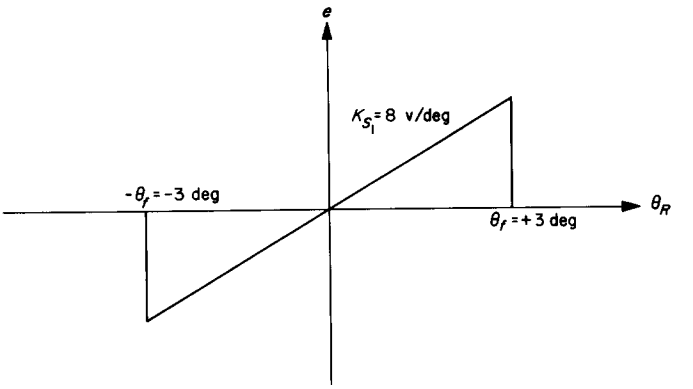

Fig. 3. Canopus tracker characteristics

gain. The other parameters are defined in Table 1. The parameters H, D, I, K_T, and K_P are based on typical characteristics of the Honeywell GG-334 series of single-degree-of-freedom wide-angle gas bearing gyros. The Canopus tracker characteristics τ_c and K_{S_1} are typical values. The tracker characteristics are shown in Fig. 3.

Eq. (6) may be further simplified by neglecting the gyro characteristic time constant I/D. For the gyro being considered, $I/D = 0.000625$ sec. Hence,

$$\frac{V_o}{\theta_R} = \frac{\dfrac{K_P H}{D}\left[s^2 + \dfrac{1}{\tau_c}s + \dfrac{K_T K_{S_1}}{H\tau_c}\right]}{\left(s + \dfrac{1}{\tau_c}\right)\left(s + \dfrac{K_T K_P}{D}\right)}. \qquad (7)$$

Table 1. Attitude-control subsystem parameter values during various modes of operation

Parameter	Mode		
	Canopus acquisition	Cruise	Commanded turns and occultations
Gyro characteristic gain, H/D	0.5	—	0.5
Gyro angular momentum, H, g-cm^2/sec	2×10^5	—	2×10^5
Gyro output axis damping, D, dyne-cm-sec	4×10^5	—	4×10^5
Gyro input angular freedom, deg (mrad)	±10 (±175)	—	±10 (±175)
Gyro output gimbal freedom, ϕ, deg (mrad)	±5 (±87.3)	—	±5 (±87.3)
Gyro pickoff scale factor, v/rad	20	—	20
Gyro output amplifier gain	1000	—	45.8
Gyro torquer gain, K_T, dyne-cm/v	36.4	—	36.4
Nominal acceleration constant, α, mrad/sec^2	0.35	0.35	0.35
Canopus tracker scale factor, K_{S_1}, v/deg	8	8	8
Canopus tracker field of view, $\pm\theta_f$, deg	±3	±3	—
Canopus tracker time constant, τ_c, sec	0.5	0.5	0.5
Commanded turn rate, θ_{R_C}, mrad/sec	—	—	π
Equivalent commanded turn voltage, E_c, v	—	—	17.3
Switching amplifier position deadband, θ_{db}, deg	±0.5	±0.5	±0.5
Switching amplifier electrical deadband, e_{db}, v	±4	±4	±4
Derived rate gain, K_D, v	13.8	13.8	13.8
Derived rate charge time constant, τ_{DC}, sec	14.0	14.0	14.0
Derived rate discharge time constant, τ_{DDC}, sec	100.0	100.0	100.0
Gas jet minimum on time, sec	0.020	0.020	0.020

CONFIDENTIAL UNCLASSIFIED

UNCLASSIFIED

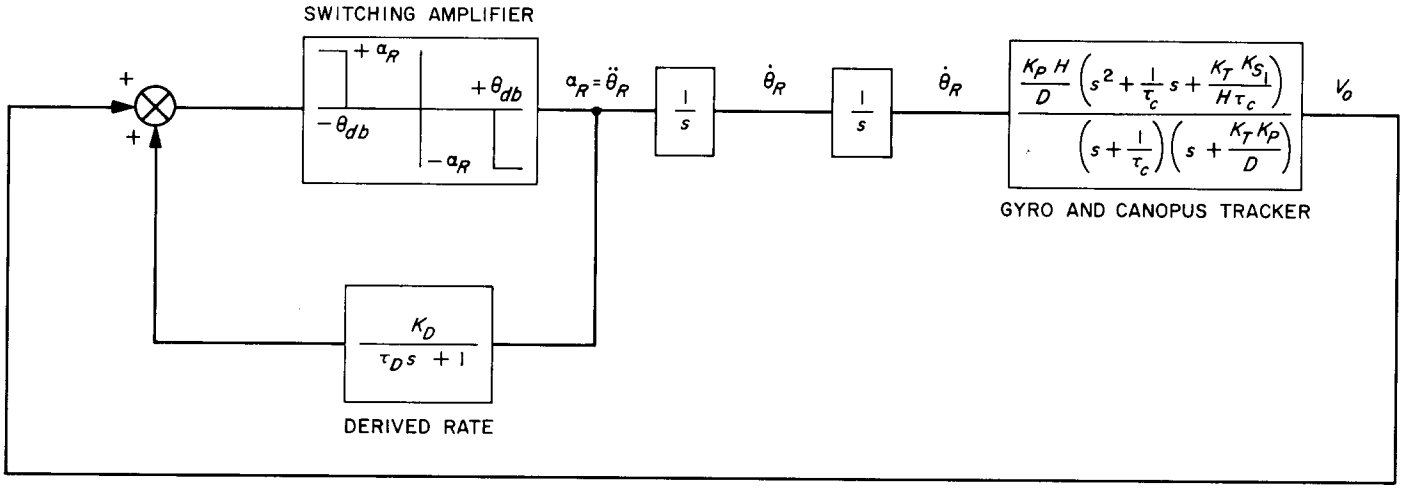

Fig. 4. Configuration of subsystem for Canopus acquisition mode

Fig. 4 shows Fig. 1 redrawn for the Canopus acquisition mode in terms of acceleration, rate, and position. Further simplification of the block diagram in Fig. 4 is possible if the effects of derived rate and the Canopus tracker time constant τ_c are ignored. This is a reasonable assumption, since the gyro is the primary controlling element during the initial portion of acquisition. If τ_c is neglected, Eq. (7) becomes

$$\frac{V_o}{\theta_R} = \frac{K_{S_1}(k_\tau s + 1)}{\tau s + 1}, \tag{8}$$

where

$$k_\tau \triangleq \text{rate-to-position gain} = \frac{H}{K_T K_{S_1}},$$

$$\tau = \frac{D}{K_P K_T}.$$

Now, for proper rate control during the initial portion of acquisition, the gyro response time τ must be comparable to the Canopus tracker time constant τ_c; i.e., τ must be on the order of 0.5 sec. If this time constant is also neglected, the block diagram shown in Fig. 4 reduces to the simple second-order configuration shown in Fig. 5. By analysis of this simplified control loop in the phase plane, upper and lower bounds can be determined for the gyro torquer gain K_T and the rate-to-position gain k_τ.

In the linear region of the Canopus tracker,

$$V_o = K_{S_1}(\theta_R + k_\tau \dot{\theta}_R), \qquad -\theta_f \leq \theta_R \leq \theta_f, \tag{9}$$

or

$$\phi = \frac{V_o}{K_{S_1}} = (\theta_R + k_\tau \dot{\theta}_R). \tag{10}$$

Now, when $\phi = \pm\theta_{db}$, the switching amplifier output is $\pm\alpha$ (equivalently). Hence, the switching lines in the phase plane are given by

$$\pm\theta_{db} = \theta_R(t) + k_\tau \dot{\theta}_R(t), \qquad -\theta_f \leq \theta_R \leq \theta_f \tag{11}$$

where

$$k_\tau = \frac{H}{K_T K_{S_1}},$$

$$\theta_{db} = \pm 0.5 \text{ deg}.$$

When $\theta_R > \theta_f$ or $< -\theta_f$, switch S_1 (Fig. 1) moves to position (2) and a search voltage V_S is applied to the gyro torquer. For this condition,

$$V_o = \frac{\left[\dot{\theta}_{R_S}\left(\frac{H}{K_T}\right) - V_S\right]}{\tau s + 1}, \qquad \theta_R > \theta_f \text{ or } < -\theta_f, \tag{12}$$

$$\approx \dot{\theta}_{R_S}\frac{H}{K_T} - V_S, \tag{13}$$

or

$$\frac{V_o}{K_{S_1}} = \phi = \dot{\theta}_{R_S}\frac{H}{K_T K_{S_1}} - \frac{V_S}{K_{S_1}} = k_\tau \dot{\theta}_{R_S} + \theta_S, \tag{14}$$

UNCLASSIFIED

UNCLASSIFIED

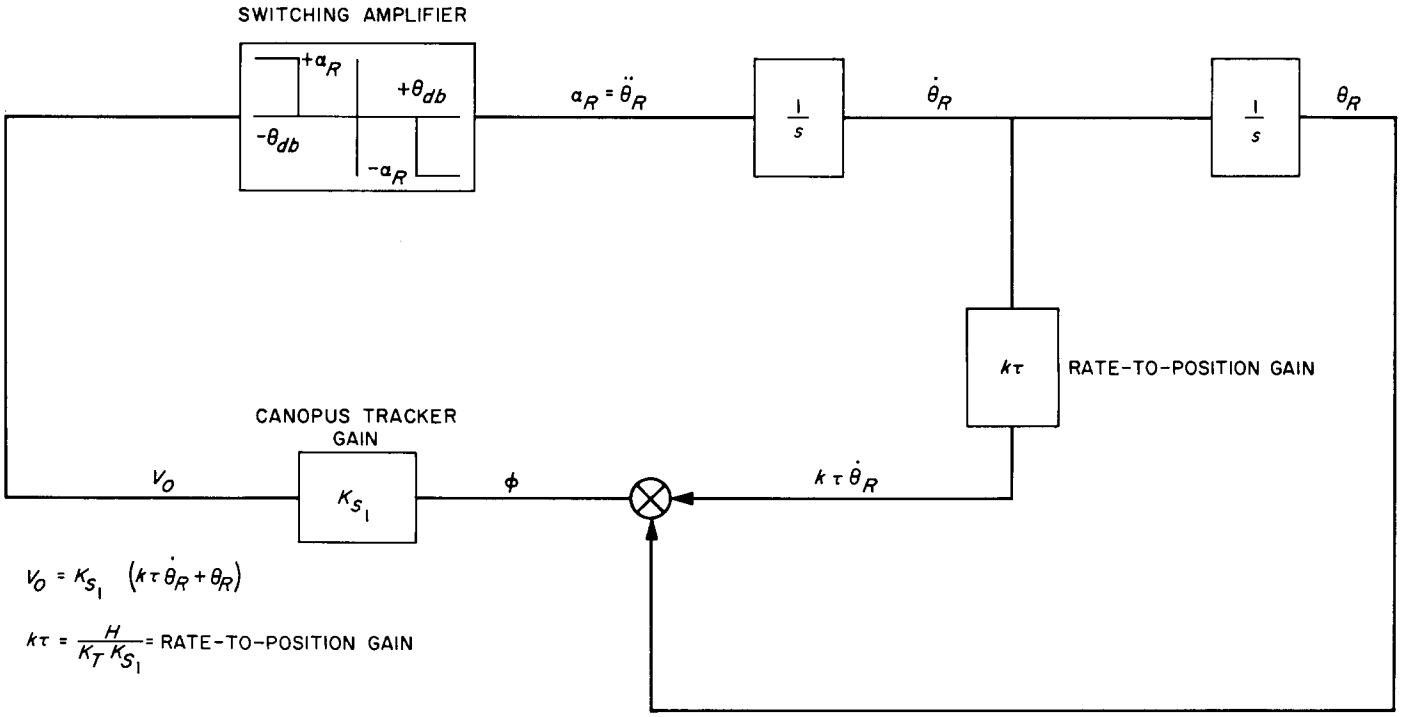

Fig. 5. Simplified configuration of subsystem for Canopus acquisition mode

where

$$\theta_S \triangleq -\frac{V_S}{K_{S_1}}.$$

Hence, the search rate deadband is given by

$$\pm\theta_{db} = k\tau\dot{\theta}_{R_S} + \theta_S, \tag{15}$$

and the actual search rate is

$$\dot{\theta}_{R_S} = \frac{\pm\theta_{db} - \theta_S}{k\tau}, \qquad \theta_R > \theta_f \text{ or } < -\theta_f. \tag{16}$$

The nominal search rate is

$$(\dot{\theta}_{R_S})_{\text{nom}} = \frac{\theta_S}{k\tau}. \tag{17}$$

Using Eqs. (11) and (16), the switching lines can be constructed in the phase plane, as shown in Fig. 6.

The phase trajectories in the phase plane are parabolic since the acceleration produced by the gas jets is constant.

$$\ddot{\theta}_R = \alpha = \dot{\theta}_R \frac{d\dot{\theta}_R}{d\theta_R}. \tag{18}$$

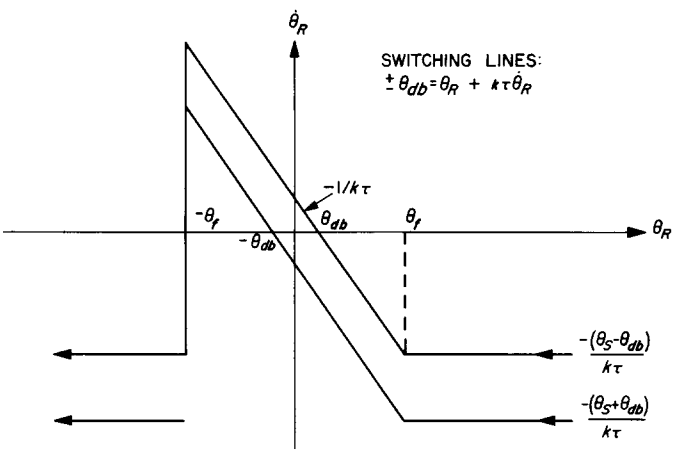

Fig. 6. Phase-plane switching lines

Integrating both sides yields

$$\int_{\theta_{R_0}}^{\theta_R} \alpha d\dot{\theta}_R = \int_{\theta_{R_1}}^{\theta_R} \dot{\theta}_R \frac{d\dot{\theta}_R}{d\theta_R} d\theta_R \tag{19}$$

$$\pm\alpha(\theta_R - \theta_{0R}) = \frac{1}{2}(\dot{\theta}_R^2 - \dot{\theta}_{0R}^2). \tag{20}$$

UNCLASSIFIED

UNCLASSIFIED

The initial conditions for Canopus acquisition (star just entering tracker field of view at roll search rate) are

$$\dot{\theta}_{R_0} = \dot{\theta}_{R_S} = \frac{\pm\theta_{db} - \theta_s}{k_T}, \tag{21}$$

and

$$\theta_{R_0} = \theta_f. \tag{22}$$

Canopus acquisition will occur if $\dot{\theta}_R \geq 0$ when $\theta_R = -\theta_f$. From Eq. (20),

$$\dot{\theta}_R^2 - \dot{\theta}_{0_R}^2 = \pm 2\alpha(\theta_R - \theta_{0_R}). \tag{23}$$

Setting $\theta_R = -\theta_f$,

$$\dot{\theta}_R^2 = 2\alpha(\theta_R - \theta_{0_R}) + \dot{\theta}_{0_R}^2 \geq 0. \tag{24}$$

Rearranging,

$$\left(\frac{\theta_S + \theta_{db}}{k_T}\right)^2 \leq -2\alpha(\theta_R - \theta_{0_R}). \tag{25}$$

Setting $\theta_{0_R} = \theta_f$ yields

$$\left(\frac{\theta_S + \theta_{db}}{k_T}\right) \leq (4\alpha\theta_f)^{1/2}. \tag{26}$$

Typical values for the acceleration constant α and the nominal search rate $(\dot{\theta}_S)_{\text{nom}}$ are as follows:

$$\alpha = 0.35 \text{ mrad/sec}^2$$

$$(\dot{\theta}_S)_{\text{nom}} = \frac{\theta_S}{k_T} = 3.56 \text{ mrad/sec}.$$

Substituting Eq. (17) into inequality (26) and solving for k_T yields

$$k_T \geq \frac{\theta_{db}}{(4\alpha\theta_f)^{1/2} - (\dot{\theta}_S)_{\text{nom}}} \tag{27}$$

A lower bound on the rate-to-position gain k_T can now be determined. The worst-case conditions on α and θ_f are

$$\alpha_{hg} = 0.17 \text{ mrad/sec}^2 \text{ (half gas failure)},$$

$$\theta_f = \pm 3 \text{ deg}.$$

Substituting into the inequality given in Eq. (27) yields

$$k_T \geq 3.6 \text{ sec}, \tag{28}$$

which represents a minimum possible value for k_T.

An upper bound on the gyro torquer gain K_T can now be determined from its relationship to k_T.

$$k_T = \frac{H}{K_T K_{S_1}}, \tag{29}$$

where

$$k_T \geq 3.6 \text{ sec},$$

$$H = 2 \times 10^5 \text{ g-cm}^2/\text{sec},$$

$$K_{S_1} = 8 \text{ v/deg}.$$

Substituting into Eq. (29) and solving for K_T yields

$$K_T \leq 121 \text{ dyne-cm/v}. \tag{30}$$

The final selection of k_T and K_T was accomplished through simulation of the control system on the IBM 1620 computer. The values that were determined are $k_T = 12.0$ and $K_T = 36.4$.

The maximum initial rate from which Canopus acquisition can occur may be computed from Eq. (24). Setting

$$\theta_{0_R} = \theta_f,$$

$$\theta_R = -\theta_f,$$

$$\dot{\theta}_R = 0,$$

and solving for $\dot{\theta}_{0_R}$ yields

$$\dot{\theta}_{0_R}^2 - 4\alpha\theta_f.$$

For a full gas system and $\theta_f = 3$ deg,

$$(\dot{\theta}_{0_R})_{\max} = 8.5 \text{ mrad/sec}.$$

This maximum initial rate was found to be exactly the same as the value determined by computer simulation.

The value of K_P, the gyro output amplifier gain, was selected to minimize the gyro time constant $(D/K_P K_T)$, subject to the constraints on amplifier physical realizability. Setting $\tau = \tau_c$ yields

$$\tau = \frac{D}{K_P K_T} = 0.5 \text{ sec}, \tag{31}$$

$$K_P = \frac{D}{K_T(0.5)} = 2.2 \times 10^4 \text{ v/rad}. \tag{32}$$

Choosing $K_P = 2 \times 10^4$ makes $\tau = 0.55$, and, for a pick-off scale factor of 20 v/rad, requires an output amplifier gain of 1000.

The switching amplifier electrical deadband corresponding to the position deadband θ_{db} is determined by the Canopus tracker scale factor K_{S_1}. This is easily shown by applying the final-value theorem to Eq. (7).

$$\lim_{s \to 0} \frac{V_O}{\theta_R}(s) = K_{S_1}. \tag{33}$$

UNCLASSIFIED

Hence, the electrical deadband is

$$e_{db} = K_{S_1}\,\theta_{db} = 4\text{ v.} \tag{34}$$

Cruise modes. At completion of Canopus acquisition, the system switches into the cruise mode (Fig. 1). The only rate damping provided during this mode is by derived rate feedback around the switching amplifier. By computer simulation of the control system configuration during its cruise mode, it was determined that system performance was not significantly affected by large variations in the selected derived rate parameters. However, the selection of derived rate parameters strongly influenced system behavior during the inertial hold mode for commanded turns, as discussed below.

Commanded turns. The attitude-control subsystem configuration for commanded turns and occultations is shown in Fig. 7. At initiation of a commanded turn, S_3 is in position (2), applying a commanded turn current pulse I_C to the gyro torquer. The gyro output is given by

$$V_o = [H\,\dot{\theta}_R - K_T\,I_C]\,\frac{K_P}{Ds}\,. \tag{35}$$

When $\dot{\theta}_R$ reaches the commanded turn rate,

$$H\,\dot{\theta}_R = K_T\,E_C, \tag{36}$$

where E_C is an equivalent commanded turn voltage. If the desired commanded turn rate is π mrad/sec, the required commanded turn voltage is

$$E_C = \frac{H\,\dot{\theta}_R}{K_T} = \frac{(2)\,(10^5)\,(\pi)\,(10^{-3})}{36.4} \tag{37}$$

$$= 17.3\text{ v.}$$

The desired commanded turn roll position is proportional to the product of the pulse amplitude and the length of time it is applied. For example, if a π-rad roll turn is desired and the commanded turn rate is π mrad/sec, the pulse duration is

$$t_{roll} = \frac{\pi}{(\pi)\,(10^{-3})} = 1000\text{ sec.} \tag{38}$$

A major constraint on the selection of commanded turn rate is the gyro angular storage limit. For the particular

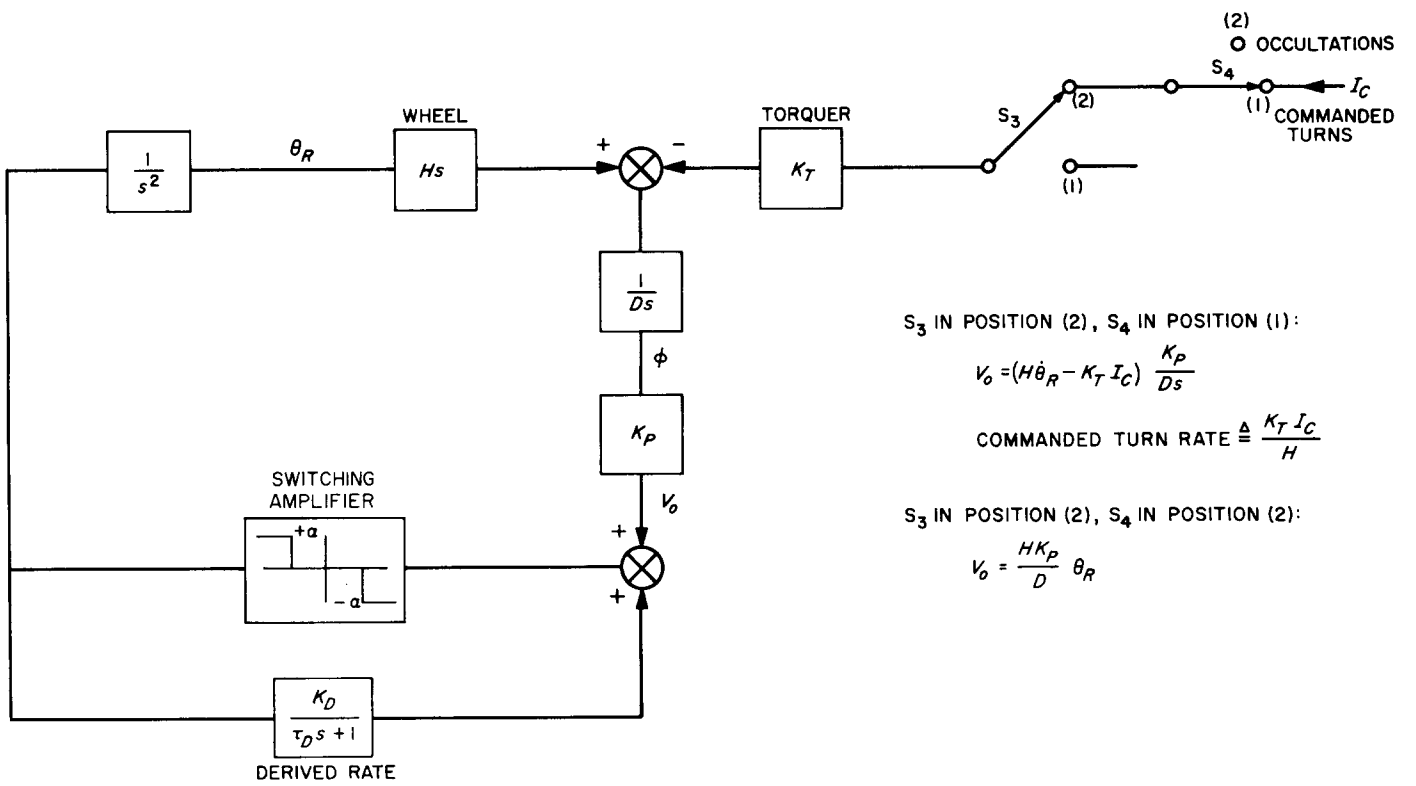

Fig. 7. Configuration of subsystem for commanded turns and occultations

UNCLASSIFIED

gyro being considered, the gyro angular input freedom is ± 10 deg. The gyro output gimbal freedom is then

$$\left(\frac{H}{D}\right)(\pm\ 10\ \text{deg}) = \pm\ 5\ \text{deg} = \pm\ 87.3\ \text{mrad}. \tag{39}$$

When the pulse is applied to the torquer, the time to reach π mrad/sec (for continuous jet firing) is

$$t = \frac{\dot{\theta}_R}{\alpha} = \frac{\pi}{0.35} = 8.97\ \text{sec}. \tag{40}$$

Assuming that $\theta_R(0) = \theta_{db} = 8.73$ mrad and $\dot{\theta}_R(0) = 0$, the worst-case angular storage that would be required is

$$\theta_{db} + \frac{1}{2}\alpha t^2 = 8.73 + (0.5)(0.35)(8.97)^2 = 22.8\ \text{mrad}, \tag{41}$$

which is considerably less than the maximum capability of ± 87.3 mrad.

Another important consideration in system performance during the initial hold and occultation modes is the effective position deadband of the switching amplifier. During Canopus acquisition and cruise, the switching amplifier position deadband is determined by the Canopus tracker scale factor (Eq. 33). However, during the inertial hold and occultation modes, the effective position deadband is determined by the gyro open-loop gain, HK_P/D. If the same K_P is used for inertial hold and occultations as was used for acquisition and cruise, the switching amplifier deadband becomes

$$\theta_{db} = \frac{e_{db}}{HK_P/D} = 0.0228\ \text{deg}, \tag{42}$$

which is approximately 1/20 of the original deadband value. This small deadband value would tend to be destabilizing and would greatly increase gas consumption.

To maintain the switching amplifier deadband at ± 0.5 deg, the gyro output amplifier gain can be switched to a lesser value when the roll inertial hold and occultation mode commands are given. For $\theta_{db} = 0.5$ deg,

$$K_P = \frac{e_{db}}{H\theta_{db}} = \frac{4}{(0.5)(0.5)} = 16\ \text{v/deg} = 917\ \text{v/rad}, \tag{43}$$

which requires an output amplifier gain of 45.8.

During inertial hold and occultations, rate damping is accomplished by derived rate. The derived rate charge and discharge time constants are selected to provide proper rate damping during the commanded turn. The input to the switching amplifier E_ε is the sum of the gyro output V_o and the derived rate signal E_D. For a positive commanded turn, V_o is negative and E_D is positive. The derived rate charge time constant is selected so that $|E_\varepsilon| \geq 4.0$ v until the spacecraft roll rate has reached the desired commanded turn rate. This assures continuous jet firing and achievement of the desired commanded turn rate in minimum time. The gyro output signal for a commanded turn is, from Eq. (35),

$$V_o = (H\dot{\theta}_R - K_T E_C)\frac{K_P}{Ds}. \tag{44}$$

Now,

$$\dot{\theta}_R = \alpha t \rightarrow \dot{\theta}_R(s) = \frac{\alpha}{s^2}, \tag{45}$$

$$E_C(s) = \frac{E_C}{s}. \tag{46}$$

Hence,

$$V_0(s) = \frac{K_P}{D}\left[\frac{H\alpha}{s^3} - \frac{K_T E_C}{s^2}\right], \tag{47}$$

$$v_o(t) = \mathcal{L}^{-1} V_o(s) = \frac{K_P}{D}\left[\frac{H\alpha t^2}{2} - K_T E_C t\right]. \tag{48}$$

Eq. (48) represents the gyro output after the gyro has charged to a value greater than the switching level of the switching amplifier, $v_o > 4$ v. Let $v_o(t) = 4$ v at $t = t_1$. Then, for $t < t_1$,

$$V_0(s) = -\frac{K_T E_C K_P}{Ds^2}, \tag{49}$$

$$v_o(t) = -\frac{K_T E_C K_P}{D} t, \qquad 0 \leq t \leq t_1. \tag{50}$$

Also, for $0 \leq t \leq t_1$, $E_\varepsilon = v_0$ since $E_D = 0$. The time required for the gyro to charge to 4.0 v is, from Eq. (50),

$$t_1 = \frac{4D}{K_T E_C K_P} = 2.78\ \text{sec}. \tag{51}$$

Now, let t_2 be the time at which the spacecraft roll rate has reached the commanded turn rate. Then, at $t = t_2$,

$$\dot{\theta}_R(t_2) = \pi\ \text{mrad/sec}, \tag{52}$$

$$|E_\varepsilon| = |v_o| = 4\ \text{v}, \tag{53}$$

and, from Eq. (40),

$$t_2 - t_1 = \frac{\dot{\theta}_R}{\alpha} = 8.97. \tag{54}$$

UNCLASSIFIED

UNCLASSIFIED

Now, for $t \geq t_1$, the derived rate is charging and

$$E_\varepsilon = K_D\,[1 - e^{-(t-t_1)/\tau_c}] + \frac{K_P}{D}\left[\frac{H\alpha}{2}(t - t_1)^2 - K_T E_C t\right]. \tag{55}$$

To assure continuous jet firing during the period $t_1 \leq t \leq t_2$, the requirement for E_ε is $|E_\varepsilon| \geq 4.0$ v. If a positive commanded turn is desired,

$$E_\varepsilon \leq -4.0 \text{ v}. \tag{56}$$

Substituting inequality (56) into Eq. (55) and rearranging yields

$$\frac{K_T K_P E_C}{D} t > 4.0 + K_D\,[1 - e^{-(t-t_1)/\tau_c}] + \frac{K_P}{D}\frac{H\alpha}{2}(t - t_1)^2, \quad t_1 \leq t \leq t_2. \tag{57}$$

Substituting

$$t = t_2 = t_1 + \frac{\dot\theta_R}{\alpha} = 11.75 \text{ sec}$$

and solving for τ_c yields

$$\tau_c > 14.6 \text{ sec}. \tag{58}$$

Hence, if the derived rate charge time constant is selected to be 14.6 sec, the derived rate signal will not cause gas jet turnoff until the spacecraft roll rate has just reached the commanded turn rate, $\dot\theta_R = \pi$ mrad/sec.

Now, at $t = t_2$, the derived rate signal has caused gas jet turnoff. To minimize the amount of rate overshoot, the discharge time constant must be selected such that the derived rate signal will not decay at a faster rate than the gyro output signal. A suitable value for the discharge time constant τ_{DDC} was determined by computer simulation (discussed later) to be

$$\tau_{DDC} = 100 \text{ sec}.$$

The value of derived rate gain, K_D, was chosen to be compatible with the charge time constant τ_c. In addition, K_D had to be chosen such that it would not cause undesirable effects during acquisition and cruise. The value of K_D finally selected again resulted from the computer simulation:

$$K_D = 13.8 \text{ v}.$$

Computer simulation. The dynamic behavior of the control system during the Canopus acquisition, cruise, and commanded turn and occultation modes was simulated on the IBM 1620 computer. The simulation program, called DIANA, is essentially a further refinement of the PACTOLUS digital–analog simulation program.

It was shown earlier that the minimum rate-to-position gain under a half gas system failure was $k_T = 3.6$ sec. The optimum value of k_T was determined by simulation to be $k_T = 12.0$ sec. From Eq. (29), the required gyro torquer gain becomes $K_T = 36.4$ dyne-cm/v. The optimum value of K_P was determined to be $K_P = 2 \times 10^4$, which, for a pickoff scale factor of 20 v/rad, requires a gyro output amplifier gain of 1000.

The search rate deadband is given by Eq. (16). For $k_T = 12.0$, $\dot\theta_{R_S} = -4.3$ mrad/sec and -2.8 mrad/sec. A phase plane ($\dot\theta_R$ vs θ_R) is illustrated in Fig. 8, showing spacecraft response during Canopus acquisition from the maximum search rate $\dot\theta_{R_S} = -4.3$ mrad/sec. Inspection of Fig. 8 shows that the phase trajectory initially enters the deadband between the switching lines, joggles up the lower switching line, enters the position deadband, and begins to limit-cycle. The joggling effect along the switching line is readily apparent in Fig. 9, which shows the alternate charging and discharging of the derived rate signal followed by the long discharge as the spacecraft coasts across the deadband and begins to limit-cycle. A gas jet minimum-on-time equal to 20 msec was included in the computer simulation.

At $t = 180$ sec, the simulated attitude-control subsystem automatically switches into the cruise mode, turning

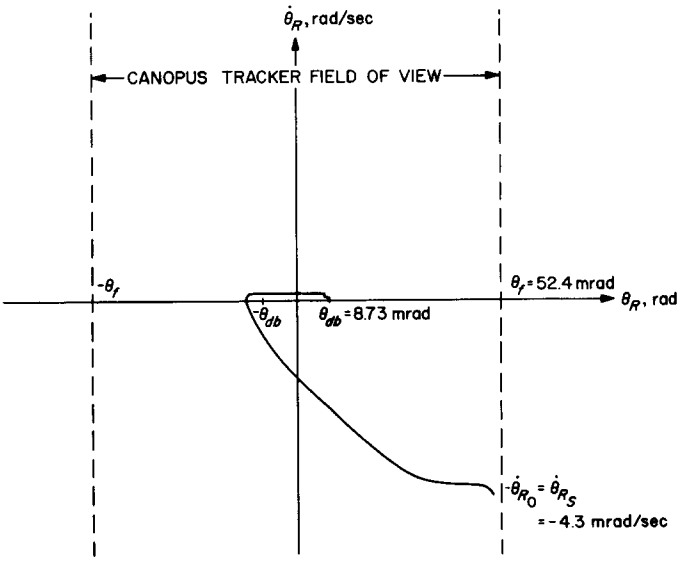

Fig. 8. Phase plane $\dot\theta_R$ vs θ_R showing spacecraft response during Canopus acquisition from maximum search rate

UNCLASSIFIED

UNCLASSIFIED

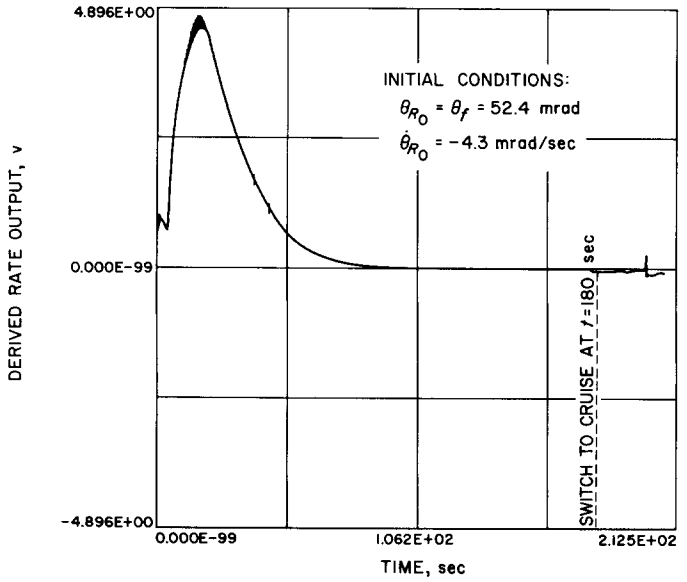

Fig. 9. Derived rate output vs time

off the gyro and applying the Canopus tracker output to the switching amplifier (Fig. 1). This length of time was selected as a nominal value and was found to be more than sufficient for acquisition of Canopus. In all cases, Canopus acquisition occurred within 90 sec.

Previously, it was determined that the maximum initial rate from which Canopus acquisition can occur is $\dot{\theta}_{R_0} = -8.5$ mrad/sec. Spacecraft response to this initial rate is shown in Fig. 10. Inspection of Fig. 10 shows continuous firing of the positive gas jet to remove the large initial rate. The phase trajectory just misses the edge of the tracker field of view, crosses the deadband between the switching lines, and joggles down the top switching line into the position deadband. This maximum initial rate is based on the minimum tracker field of view of 3 deg (52.4 mrad). The nominal field of view is 4 deg, in which case the maximum initial rate would be approximately -10.0 mrad/sec.

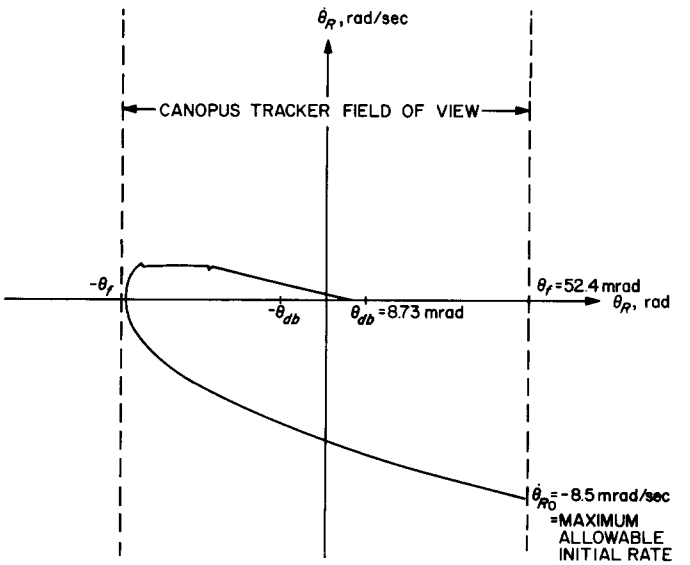

Fig. 10. Phase plane $\dot{\theta}_R$ vs θ_R showing spacecraft response for maximum initial search rate from which Canopus acquisition can occur

The primary source of rate damping during acquisition is provided by the gyro. Fig. 11, however, shows that Canopus acquisition is possible with derived rate as the only source of rate damping (e.g., gyro failure), provided that the initial rate is not too large. For the case shown in Fig. 11, $\dot{\theta}_{R_0} = -3.0$ mrad/sec. This case clearly shows that, even though the derived rate parameters are optimized for commanded turns, any additional rate damping provided by derived rate aids, rather than hinders, acquisition. During cruise, it was determined that the system was not highly sensitive to the degree of rate damping provided by derived rate since very little rate damping is required to maintain stable limit-cycle operation.

It was determined earlier in this article that, if the derived rate charge time constant τ_{DC} was chosen to satisfy the inequality given in Eq. (58), the derived rate signal would not cause jet turnoff until the spacecraft roll rate had reached the commanded turn rate, $\dot{\theta}_R = \pi$ mrad/sec. The value of τ_c determined by simulation

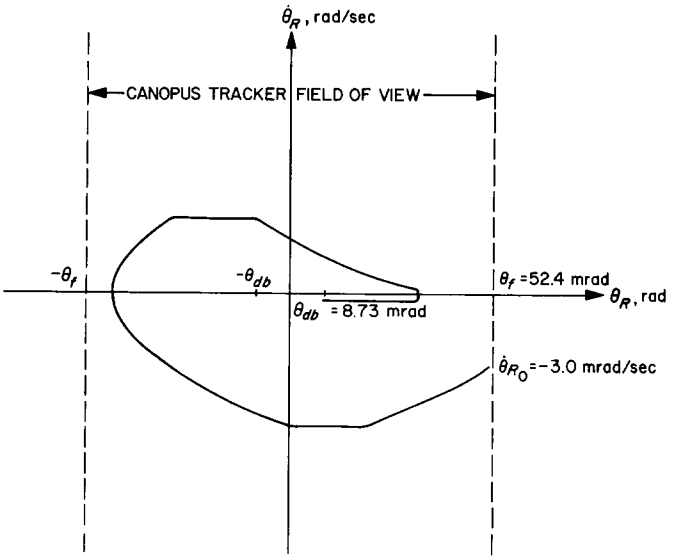

Fig. 11. Derived rate acquisition

UNCLASSIFIED

UNCLASSIFIED

to yield this response is $\tau_c = 14.0$ sec. The derived rate discharge time constant τ_{DDC} was selected to minimize the amount of rate overshoot during the commanded turn. Ideally, the commanded turn response would be critically damped (i.e., no overshoot) if τ_{DDC} is infinite. This is equivalent to the derived rate discharge behaving as an ideal integrator. However, subject to the constraints on component physical realizability, τ_{DDC} was selected to be $\tau_{DDC} = 100$ sec.

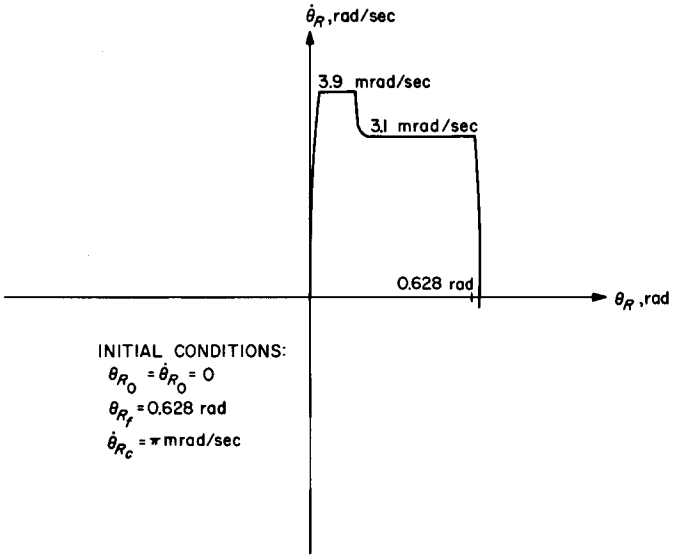

Fig. 12. Phase plane $\dot{\theta}_R$ vs θ_R showing spacecraft response for commanded roll turn

Fig. 12 shows the spacecraft response to a 0.628-rad commanded roll turn. The commanded turn was executed by simulating an equivalent voltage pulse of height $E_c = 17.3$ v and duration $\Delta T = 200$ sec on the input to the gyro torquer (Eq. 37). Inspection of Fig. 12 shows the rate overshoot to be approximately 25% and the rate undershoot to be 2%. The overshoot and undershoot are caused by the intermittent firing of the gas jets after the spacecraft has reached the commanded turn rate. This effect results from the alternate charge and discharge of the derived rate signal.

Fig. 13 shows the gyro angular storage required for the commanded turn. The gyro output gimbal position varies from −11.42 to 11.37 mrad, a range well within the design limits for wide-angle gyros.

The required attitude-control subsystem parameters for Canopus acquisition, cruise, and inertial hold (commanded turns and occultations), based on the computer

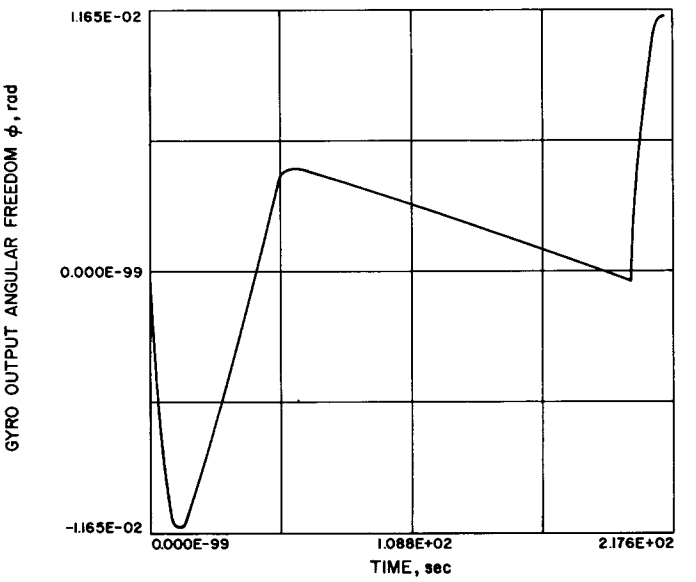

Fig. 13. Commanded-turn gyro output gimbal angle vs time

simulation and the analysis presented here, are listed in Table 1.

The values given represent typical values based on analysis of the nominal attitude-control subsystem configuration. Further analysis remains to be carried out in the areas of cruise-gas requirements and gyro drift effects during inertial hold modes. The final phase of this study calls for the development of an actual hardware simulation model of the attitude-control subsystem.

2. *Triple Redundancy in Attitude-Control Electronics*

Breadboard construction and testing of the attitude-control triple-redundant circuits proposed in the spacecraft conceptual design on December 1965 have been under way since that time. Fig. 14 depicts the basic electronics circuit for a single axis of control; the circuit is made up of the following three distinct parts:

(1) *Triple redundant power switches.* Fig. 15 shows diode and transistor mechanizations for a digital switching circuit. The required output logic for triple redundancy (i.e., majority voting) is: $(A \cdot B) + (B \cdot C) + (C \cdot A)$. An entire power switch for the roll-control axis that was completely breadboarded and initiated into testing on December 20 has undergone more than 5000 hr of life testing under various simulated failure conditions and is performing perfectly. Dual chip transistors (NPN–PNP, NPN–NPN, and PNP–PNP) are being utilized

UNCLASSIFIED

UNCLASSIFIED

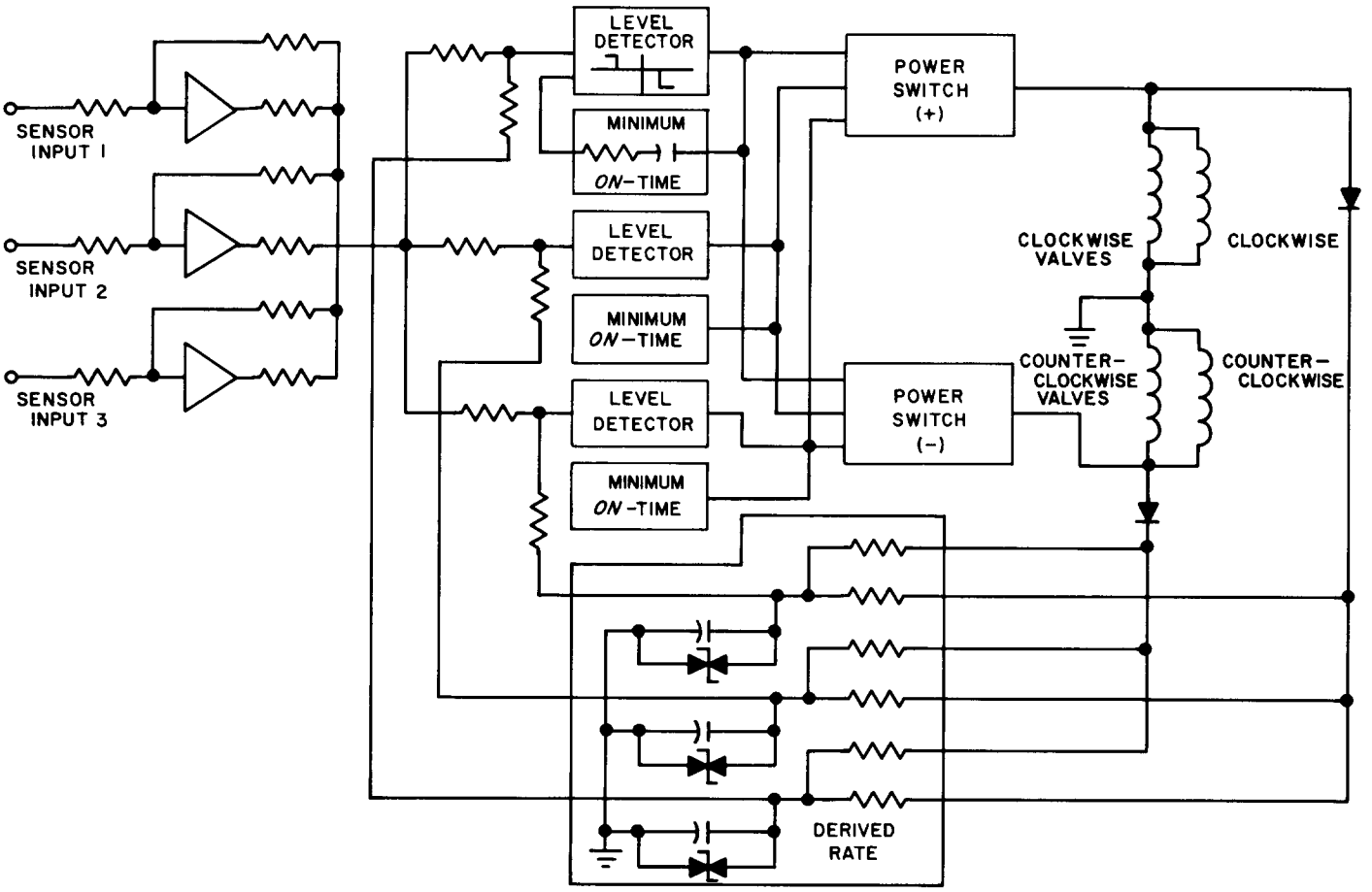

Fig. 14. Attitude-control redundant single-axis electronics

UNCLASSIFIED

UNCLASSIFIED

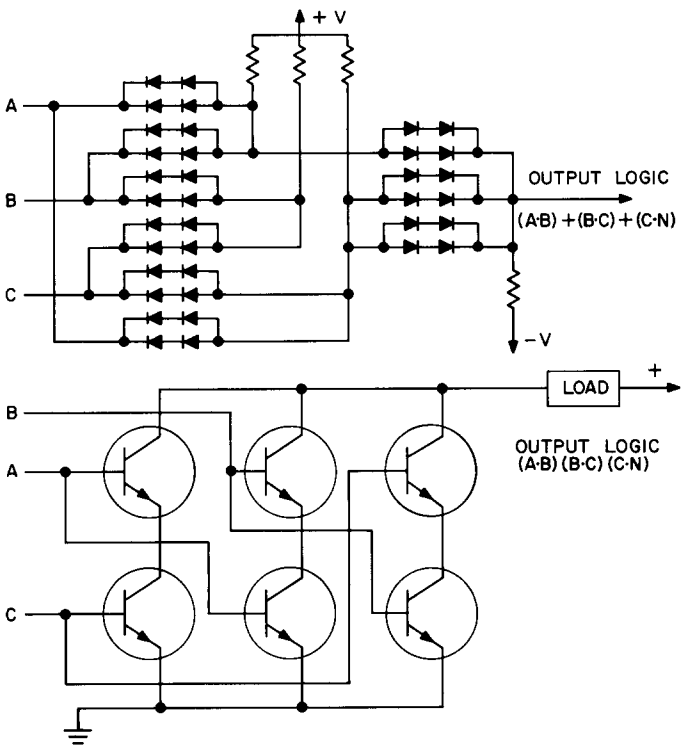

Fig. 15. Triple-redundant circuits for digital signals

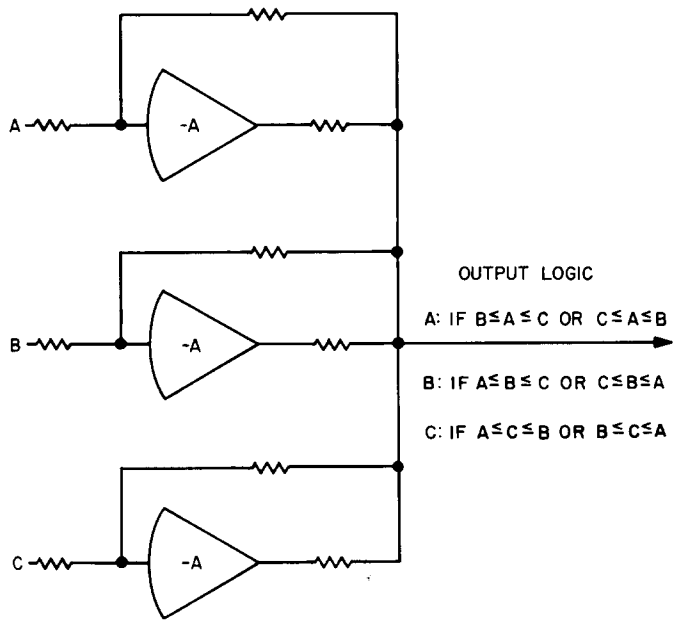

Fig. 16. Triple-redundant circuit for analog signals

to decrease volume. This breadboard also contains the triple-redundant (i.e., separate resistance-capacitance) derived-rate circuits.

(2) *Level detectors (with minimum on-time).* Each of these circuits, which serve the threefold function of a summing junction for derived rate, deadband, and minimum *on*-time, are constructed using two integrated circuit operational amplifiers. Integrated circuits by General Electric Co., Fairchild Semiconductor, and Philbrick Researches, Inc., are being evaluated. Three of the circuits have been constructed, tested, and used to drive the power switch section; testing to date indicates the circuits are functioning correctly.

(3) *Analog amplifiers.* Fig. 16 illustrates the basic logic circuit used to amplify analog signals in a triple-redundant approach. The logic shown represents an analog to the majority-voting logic of the power switch. This circuit, which drives the level detector section, has been constructed and tested.

An entire single-axis subassembly of the triple-redundancy electronics has been completed and is ready for demonstration. The schematic of the subassembly is shown in Fig. 17. Figs. 18 through 21 illustrate the breadboarded hardware. Seventeen switches (labeled A through Q in Fig. 17) are available to simulate various failure conditions in all parts of the system. Approximately 2750 hr of life testing have been accumulated on the over-all system.

Breadboarding of other conceptual redundant techniques for the next few months will be concentrated on logic, time delay, and power switching circuitry.

C. Telecommunications

1. High-Impact Traveling-Wave-Tube Amplifier Development

The traveling-wave-tube (TWT) amplifier development program first described in *SPS 37-39*, Vol. II, pp. 29, 30, has been redirected; only a TWT and its associated RF output filter are now being developed. The effort required to develop a TWT capable of surviving 10,000-*g* 1-msec shocks is greater than was anticipated by either Watkins-Johnson Co. or JPL. In fact, it is now apparent that the effort required to develop the TWT and filter will be more than was originally planned for the entire amplifier, including the power supply and package.

CONFIDENTIAL
UNCLASSIFIED

UNCLASSIFIED

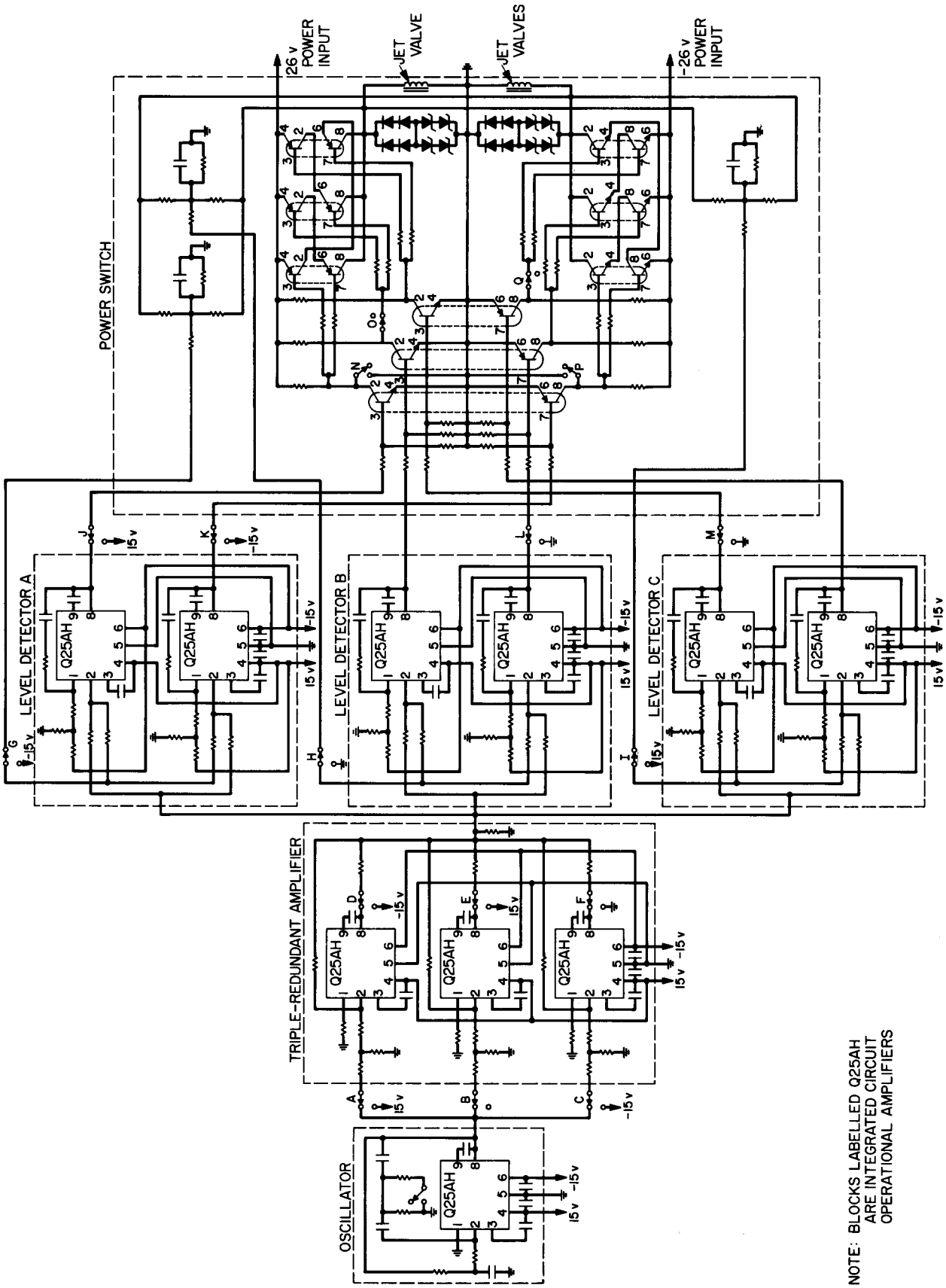

Fig. 17. Single-axis subassembly of the triple-redundant electronics

UNCLASSIFIED

UNCLASSIFIED

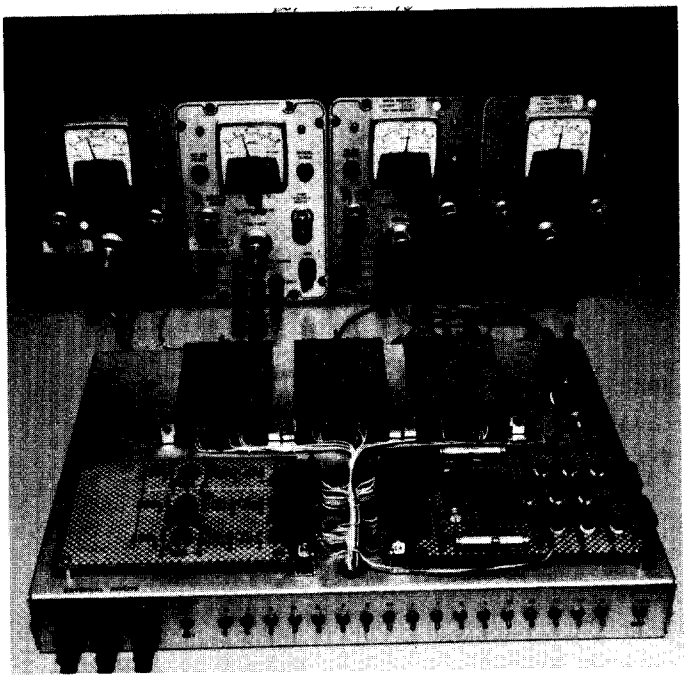

Fig. 18. Over-all test setup for triple-redundant electronics

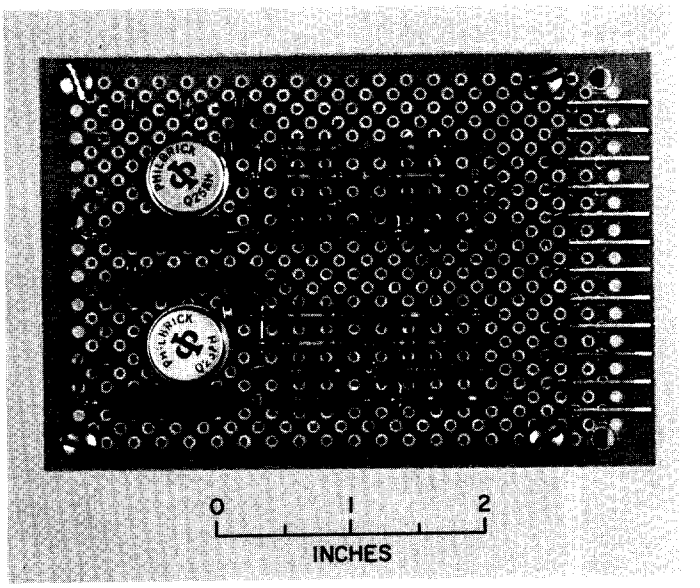

Fig. 20. Level detectors

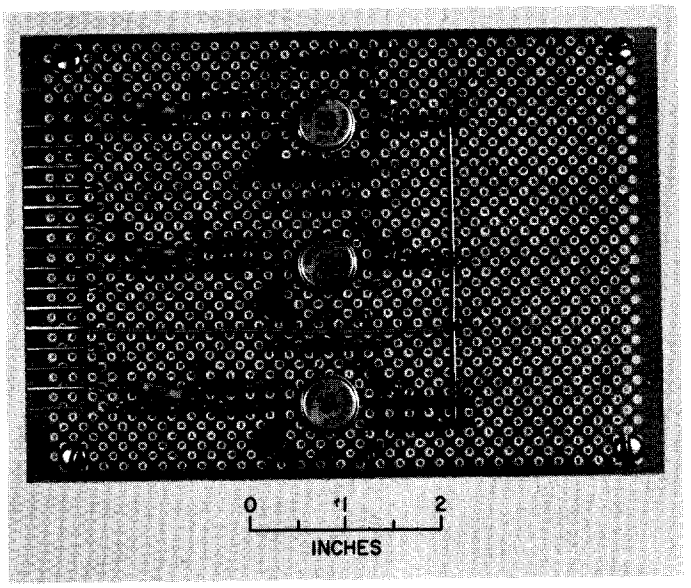

Fig. 19. Analog amplifiers

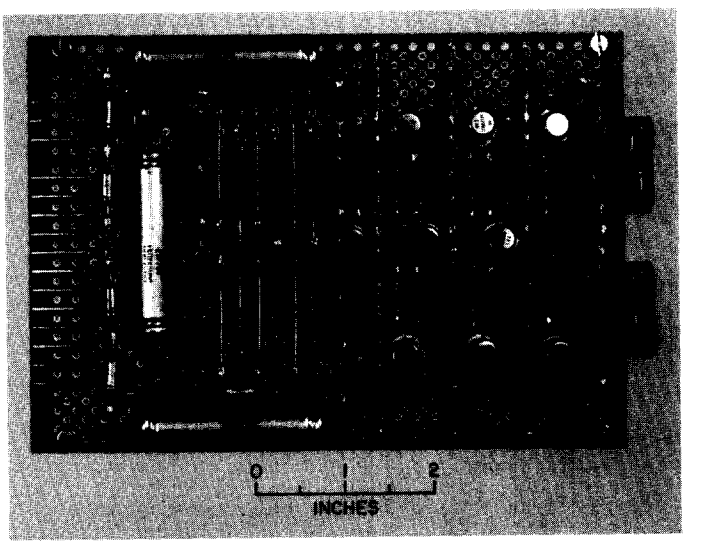

Fig. 21. Power switches

CONFIDENTIAL
UNCLASSIFIED

UNCLASSIFIED

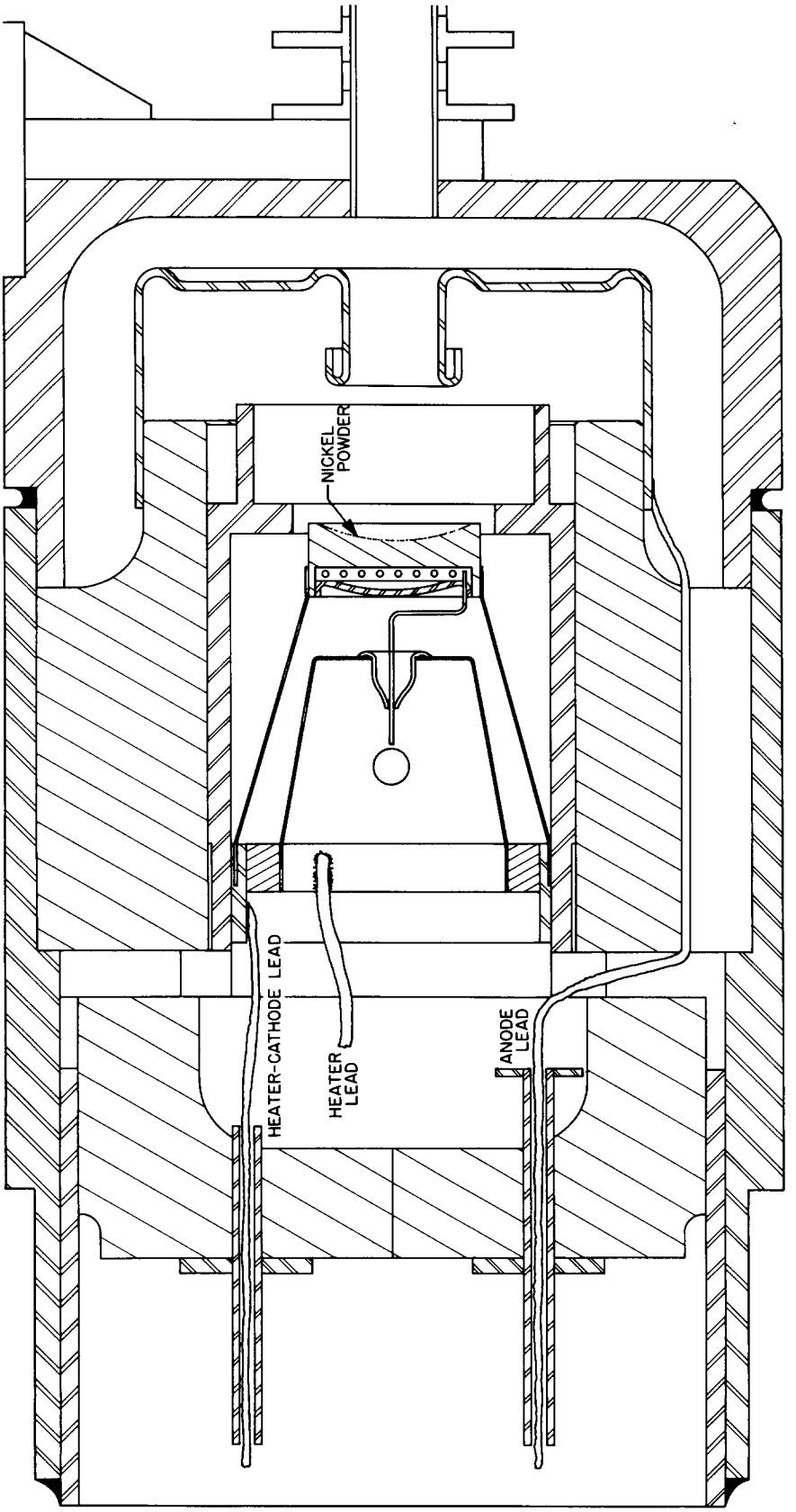

Fig. 22. Final design of high-impact TWT electron gun

UNCLASSIFIED

UNCLASSIFIED

a. TWT development. Four series of high-impact tests of TWT components have been conducted. Original program plans called for a single series of high-impact tests preceding fabrication of the first TWT, but the deficiencies revealed by tests were greater in number and severity than anticipated. The major problems occurred in the following areas:

(1) Breakage of ceramic electron-gun parts.

(2) Deformation of the cathode button.

(3) Oxide coating stripped from the cathode button.

(4) Failure of magnet supports.

(5) Failure of the helix lock-in technique.

The ceramic breakage problem has been solved by using pressure-molded ceramic parts, instead of parts machined from ceramic stock, and by redesigning all of the parts to avoid stress concentrations caused by sharp corners. Cathode-button deformation has been corrected by increasing the thickness of the cathode button. The cathode button is now roughened by sintering a layer of nickel spheres to its surface before applying the cathode coating; also, the coating is now brushed on, instead of sprayed on. These two changes increased oxide adhesion and prevented loss of the oxide coating in the fourth series of tests.

Design, fabrication, and testing of three different electron guns were required to meet the 10,000-g test requirement. The final electron gun design is shown in cross section in Fig. 22.

Failure of the TWT magnet supports was reported in *SPS 37-39*. The magnets in the periodic focusing array are now supported by nonmagnetic "washers," which fit between the individual ring-shaped magnets and extend outward into a supporting mass of hard epoxy. This configuration, illustrated in Fig. 23, proved adequate in later tests.

Failure of the planned helix lock-in technique has been the most serious problem encountered to date. The glaze bond, reported in *SPS 37-39*, will support the helix within the beryllia rods, but the beryllia rods themselves move when the assembly is shocked in the axial direction. The final design uses a helix-and-rod assembly which is 0.001 in. larger than the inner diameter of the supporting stainless-steel tube. The helix assembly is inserted by deforming the tube and is held in place by compression. The beryllia rod cross-section has been changed to cause a line contact with the outer tube, rather than an area contact, to increase the resistance to axial motion.

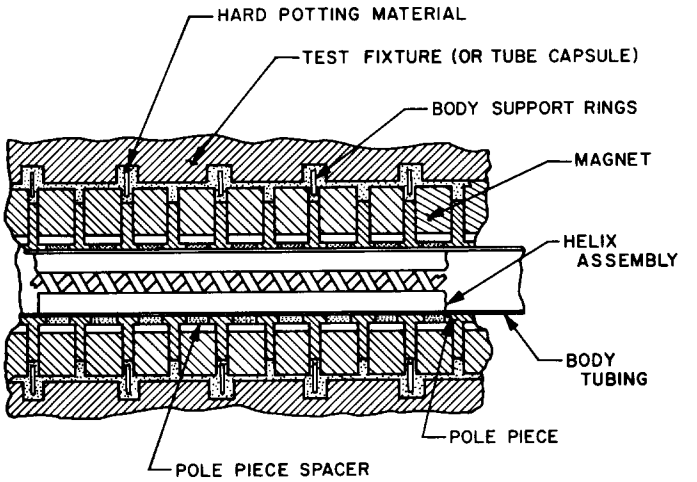

Fig. 23. Final design of magnet lock-in scheme

The data from the fourth series of high-impact tests are still being analyzed. The cathode support cone was damaged slightly, and there were changes in the voltage standing wave ratios of both the input and output helices. It seems likely that the problems remaining will be minor enough to allow the fabrication of a complete TWT with a reasonable level of confidence; if so, fabrication should be completed in late-October.

b. RF output filter development. The RF filter designed by Rantec Corporation is a six-section low-pass and band-reject unit. Insertion loss is less than 0.3 db. The breadboard unit was shocked at 13,000 g for 0.5 msec. There was significant deformation of the tuning probes and motion of the low-pass center conductor, but the filter's electrical characteristics remained within the specification limits. An engineering model with larger diameter tuning probes was then fabricated, and this unit passed the shock tests with no significant deformation.

The qualification unit has been fabricated by Rantec, but will not be delivered until late-September, when test equipment will be available for shock tests of the specification requirement of 1-msec duration, instead of the present maximum of 0.5 msec.

c. Revised amplifier characteristics. The specifications for weight, input power, and input voltages were changed by the deletion of the power supply and package. The

CONFIDENTIAL UNCLASSIFIED

UNCLASSIFIED

input power and voltage specifications listed in *SPS 37-39* may be regained at a later date by addition of an 85%-efficient power supply. The weight of the TWT and filter is now specified as less than 3 lb.

2. Development of a Spacecraft Traveling-Wave-Tube Amplifier

A 50-w traveling-wave-tube (TWT) amplifier is being developed for spacecraft use. A single package, approximately $5\frac{1}{2} \times 3 \times 10$ in., will contain a TWT, a power supply, and an RF output filter. The entire amplifier is to take DC power from a 25- to 50-v bus and produce an S-band output of 50 w from an input RF drive of 200 mw. Design specifications are summarized below:

Weight, lb	7
Operational life, hr	20,000 +
Input power, w	$\leqslant 150$
Input voltage, v dc	25 to 50
RF output, dbm	47 (50)
RF input (drive), dbm	$\leqslant 23$
Frequency range, GHz	2.29 to 2.30

The amplifier packaging design and the TWT design and fabrication are being accomplished by EIMAC, a division of Varian Associates; Engineered Magnetics, a division of Gulton Industries, will design and fabricate the power supply; and Telonic Engineering Company will design and fabricate the RF output filter.

a. Amplifier packaging. The amplifier is to operate through critical breakdown pressures; thus, it will be able to operate during launch or during entry in a planetary lander. Because of the high DC voltages (2-kv) required for TWT operation and the RF voltages in the output filter, the amplifier will be packaged in a hermetically sealed stainless-steel container pressurized with SF_6 gas. This gas is chemically inert and has a high minimum breakdown voltage at its critical breakdown pressure.

The enclosure design is based on the MILCOMSAT amplifier enclosure. The MILCOMSAT amplifiers have accumulated 75,000 test hr in vacuum, with 10,000 hr on a single unit. Eight such units are now in orbit. No enclosure failures have occurred.

b. TWT design. The most difficult requirement of this development is the 33%-efficiency (over-all) specification. The current design calls for this to be met by using a 43%-efficient TWT, an 88%-efficient power supply, and an RF filter with 0.4 db of loss. No "exotic" techniques such as velocity jumps or phase tapers are to be used. The efficiency requirement is to be met by optimizing a standard single depressed-collector TWT design. This design restriction is necessary to assure timely development and qualification of a state-of-the-art amplifier.

The TWT design efficiency goal is based on an RF beam efficiency of about 25% and a collector depression of 50%. If these are met, this would result in an over-all efficiency slightly above the required 43% when helix interception and heater power are taken into account.

To achieve the beam efficiency, the electron-beam-to-helix coupling is being maximized. Beryllia helix support rods are being used, instead of the usual alumina, to reduce dielectric loading on the helix. A flat-tape helix will be used, rather than a wire helix, to reduce the difference between the beam diameter and the mean helix diameter. If proved reliable by vacuum heating tests, the helix may be copper-plated to reduce resistive losses.

High beam efficiencies generally result in small allowable collector depressions because of the large velocity spread in the beam. This tendency will be reduced in this design by a defocusing magnetic field in the collector. This defocusing field will prevent low velocity primary beam electrons and locally generated secondary electrons from returning to the helix. An electrostatic defocusing iris will aid the magnetic field and will intercept returning electrons, thus preventing helix heating.

c. Power-supply design. The power-supply efficiency requirement is 88%. Since this is slightly above the present state-of-the-art, Engineered Magnetics felt that a more advanced concept than the separate regulator and converter used for the *Mariner* Mars 1964 TWT power supply must be employed.

Engineered Magnetics advanced concept uses a conventional low-power regulator and converter to provide filament, anode, and helix voltages, but used a power bridge circuit to regulate and invert power for the collector supply in a single operation. Since more than 80% of the TWT power input is used by the collector supply, any gain in efficiency would have its greatest effect at this point. Unfortunately, the AC output waveform of the new regulator–converter, consisting of variable-width positive and negative pulses, is difficult to rectify and

UNCLASSIFIED

CONFIDENTIAL
UNCLASSIFIED

filter. Rectifier diode and filter losses have reduced the efficiency to less than that of conventional units.

A parallel effort has been started to develop a conventional supply based on the *Mariner* Mars 1964 design. Development of both supplies will be continued until sufficient data are available to enable a decision as to the most desirable concept.

d. RF output filter design. Telonic Engineering Company is designing a four-section band-pass filter which will provide enough rejection at spacecraft up-link frequencies to prevent TWT noise from causing an increase in the effective spacecraft receiver noise figure. This filter will also attenuate the TWT harmonics sufficiently to prevent RF interference from this source.

e. Development status. The first test TWT fabricated had a large number of discrepancies. An excessive amount of braze material was used in fabricating the RF windows. This material "wicked" into an expansion joint and caused stresses which cracked the ceramic insert, admitting air to the tube and poisoning the cathode.

The window and the cathode were replaced, and the tube was reactivated. RF tests showed that the helix turn-per-inch (TPI) value was incorrect. This error resulted in a 3-kv required beam voltage, instead of the designed 2-kv, and also caused the gain parameter to be below the required value. Since the beam efficiency is related to the gain parameter, it was also lower than desired. Beam efficiency was 14%, as opposed to the 25% design beam efficiency. Before the optimum operating point could be located so that over-all efficiency measurements with the depressed collector could be made, another leak developed and the cathode was again poisoned. Because of the excessive beam voltage and non-depressed collector operation, the electron beam remained focused within the collector and overheated the end cap. The resulting expansion cracked a braze joint, admitting the air.

Because the first TWT deviated so greatly from design parameters, no further attempt was made to repair it. A second test TWT has now been fabricated and will be tested in the near future.

After the poor showing by the supposedly advanced power supply concept, an alternate breadboard unit with more conventional circuitry has been fabricated. No data have yet been generated concerning its performance.

A first RF output filter prototype has been delivered to EIMAC. Manufacturer's data show that the rejection is greater than required at all frequencies of interest. Insertion loss is 0.4 db, the maximum allowed by the specification.

No attempt to finalize the amplifier packaging design will be made until the major component designs have been made more definite. Further developments will be reported in the *SPS* as they occur.

3. S-Band Traveling-Wave-Tube Test Set Design

The philosophy, design, and mechanization of an S-band traveling-wave-tube (TWT) test set were described in *SPS 37-39*, Vol. II, pp. 30–34. This article describes some changes and additions to the test set, which were found necessary in order to evaluate the TWT.

The JPL-designed transistorized circuitry which protected the TWT helix from excessive current and shut down the TWT when its output power dropped operated marginally. The chief problem was susceptibility to line transients and subsequent transistor damage by power supply transients. The circuitry was changed to afford better isolation between the two functions, and small-voltage zener diodes were placed across the inputs. The circuit is now stable in operation and appears immune to line transients.

The original philosophy did not afford protection in the event of failure of power to the protective circuitry. A voltage-sensing relay was installed to shut down all AC power to the test set and the TWT in the event of such a failure.

The initial design of the protective circuitry for loss of vacuum did not include an override switch. Because of this (when interfacing with the vacuum chamber), the test set and TWT would not turn on until a vacuum of at least 10^{-3} mm Hg was reached. A hooded toggle switch was installed in the test set to bypass the loss-of-vacuum protection system until at least 10^{-3} mm Hg was achieved.

The need to know the time at which a failure occurred was easily satisfied by the installation of an ordinary 117-v 60-cycle clock across the protected 117-v circuitry, since such circuitry remained off after a failure until manually activated.

UNCLASSIFIED

UNCLASSIFIED

An unforeseen difficulty arose in the high-voltage feed system inside the vacuum chamber. Due to outgassing of the resilient insert of military-standard (MS) connectors carrying high voltages to the TWT, an ionized path occurred between the pins and the case of the connector, permitting an arc-over to occur. The difficulty was overcome by removing the connectors from the chamber and running all DC voltages to the TWT by wire alone. As may be seen in Fig. 24(a), the connector was physically secured to the entry plate, but remained outside the chamber. The wire (25-kv capability) entered the vacuum chamber through a teflon and steel packing gland (Fig. 24b). No arcing occurred thereafter.

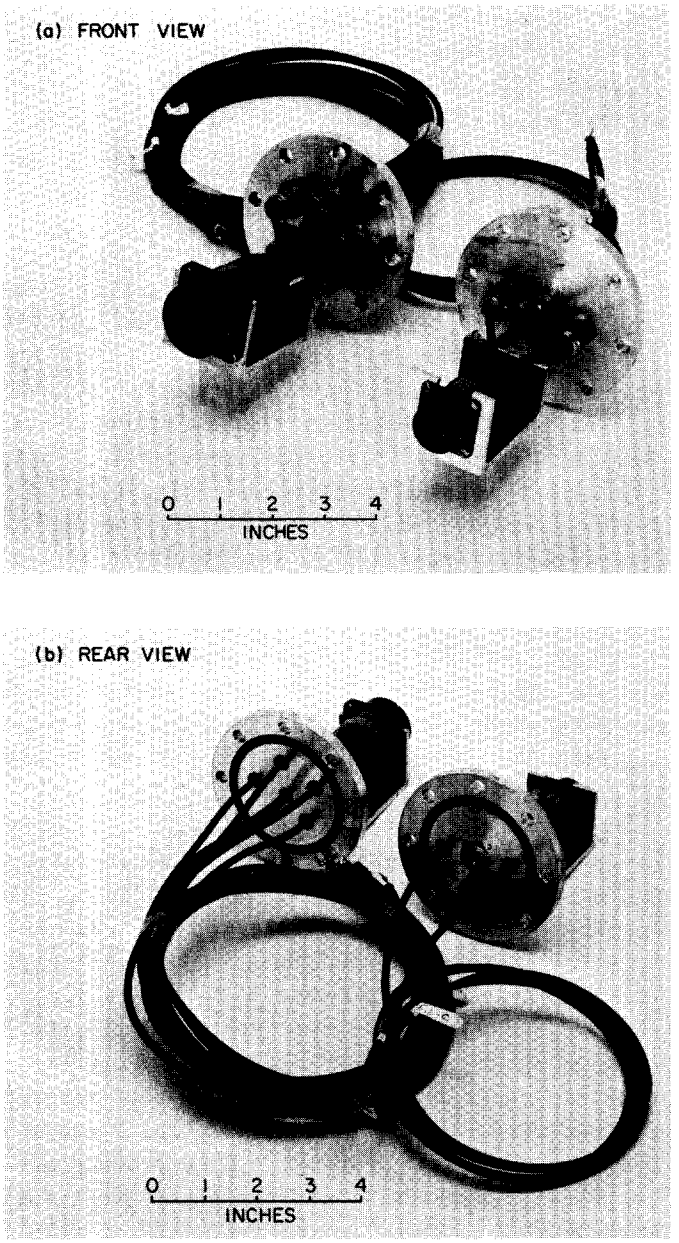

Fig. 24. High voltage entry into the vacuum chamber

Temperature testing of the TWT (a Hughes 394-H) began on July 15, 1966 (per JPL *Mariner* Mars 1964 Specification 30250B) and was completed on July 28. The test set performed quite well during this period. No actual TWT failure occurred, although the protective circuitry of the test set was exercised several times when severe power line variations occurred and when the TWT's environment exceeded preset levels.

The TWT is now ready for shock test and vibration (per the same JPL specification). A report covering the TWT's performance through the entire test sequence will be issued at the conclusion of all testing.

D. Propulsion

1. Preliminary Evaluation of G-11 and G-16 Percussion Primers

Percussion primers, like those usually used in rifle ammunition, can also be used for initiating certain pyrotechnic devices on spacecraft, such as parachute reefing line cutters and parachute release mechanisms, and possibly for releasing shock absorbing material from a capsule. However, most such primers are quickly deteriorated by elevated temperatures and will not meet the *Voyager* spacecraft thermal sterilization requirement. Certain high-temperature storage tests have been made at Frankford Arsenal on four versions (49G-11, 49G-16, 73G-11, and 73G-16) of a percussion primer manufactured by the Remington Arms Company. These four primers are described in Fig. 25. Results of the Frankford Arsenal tests (Ref. 1) indicate that these primers may be heated to the sterilizing temperature of 275°F for several hundred hours without adverse effects.

However, to determine the feasibility for the use of these primers on a spacecraft (as well as possible design limitations), it was necessary to investigate several additional characteristics of these primers. All firing tests were performed on the ball drop machine shown in Fig. 26. This apparatus allowed the 2.32-oz ball to be dropped on the firing pin from various measured heights to determine the input energy imparted to the primers.

CONFIDENTIAL
UNCLASSIFIED

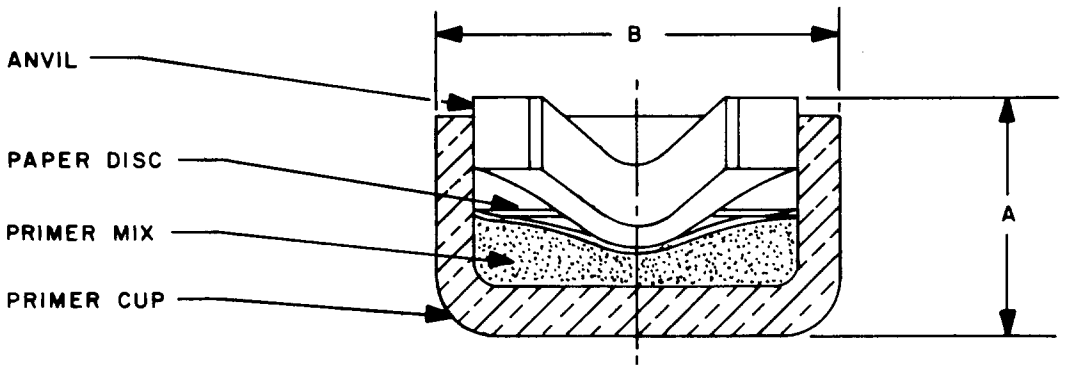

PRIMER TYPE	DIMENSIONS, in.		CHARGE, grains	NOMINAL SENSITIVITY (90% FIRING POINT), in.-oz
	A	B		
49G—11	0.119	0.175	0.31	32.2
73G—11	0.119	0.210	0.43	39.5
49G—16	0.119	0.175	0.31	38.5
73G—16	0.119	0.210	0.43	48.8

Fig. 25. Physical characteristics of four percussion primers

First, a series of tests was conducted to determine the effect of confinement of the primers on "squibbing" or low-order firing. It was determined that the "squibbing" could be eliminated by confining the primers with aluminum membranes 0.005 in. thick. All of the following tests were made with the primers confined in this manner.

Tests were then performed to determine if primer sensitivity could be increased by reconsolidating the pyrotechnic load by mechanically pressing the primers into the firing holders. A small increase in sensitivity resulted (Fig. 27).

The energy required to fire primers with the firing pin offset 0.025 in. from the center was compared with the energy required when the firing pin was in the center. As shown in Fig. 28, a considerable difference was noted.

A temperature shock test was made by subjecting 10 primers to 10 cycles between −60 and 300°F. The primers were allowed to soak 1 hr at each temperature. After the 10 cycles, the primers were returned to room temperature and were fired. When the results were compared with a control sample of 10 identical (unshocked) primers, no degradation of sensitivity was observed.

An impact shock test was performed by mounting eight primers in firing holders. These were then mounted in a fixture and accelerated down the track of a JPL impact test machine. The average shock was approximately 9100 *g* for approximately 0.5 msec. The peak acceleration was about 12,000 *g*. All eight primers were then functioned in the ball drop machine with an input of 65 in.-oz. All firing was of high order.

To determine the effect of rough handling, 12 primers were placed in a round steel container with square ends (similar to a 1-qt paint container) set up to rotate end over end, and were tumbled for 10 min. The container, 5 in. high and 3.5 in. in diameter, was rotated at 45 rev/min. The primers fell a distance of 5 and 3.5 in. twice each revolution, or a total of 1800 drops in the 10 min. After the tumbling, each primer was pressed into a holder and fired at an energy input of 65 in.-oz (drop height of 28 in.). All firing was of high order.

Since the chemical composition of the G-11 and G-16 primers is slightly different (Table 2), it was considered important to obtain information on their relative firing sensitivity. The results of this series of tests are shown in Fig. 29.

After the above testing had been completed, additional information on the subject of primers was received from the Remington Arms Company. Remington indicated that the 49-size primers were intended for use in 30-caliber carbine ammunition and the 73-size primers were to be used in 30-caliber rifle ammunition. Both the carbine

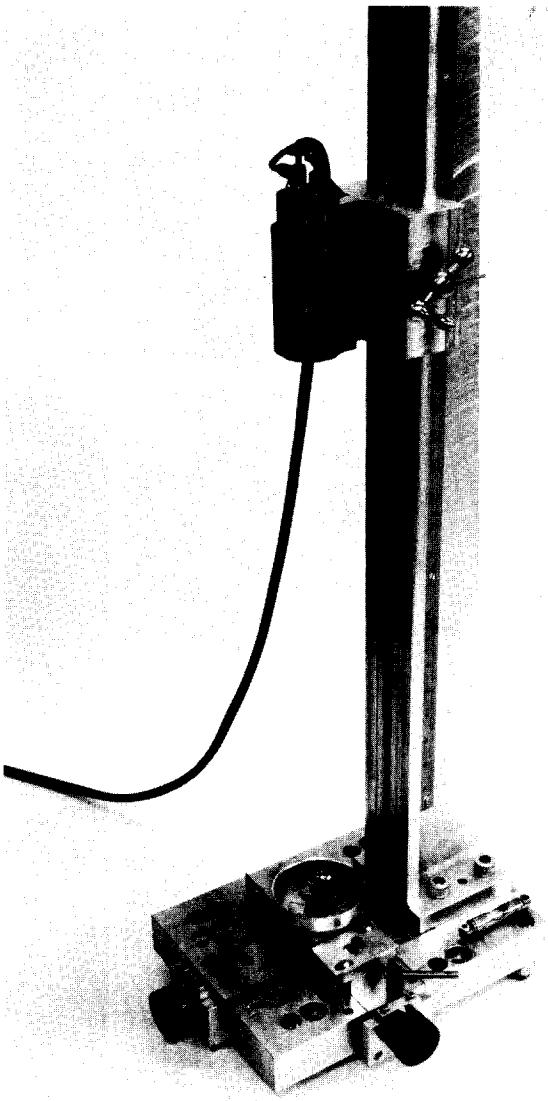

Fig. 26. Ball drop machine used in primer firing tests

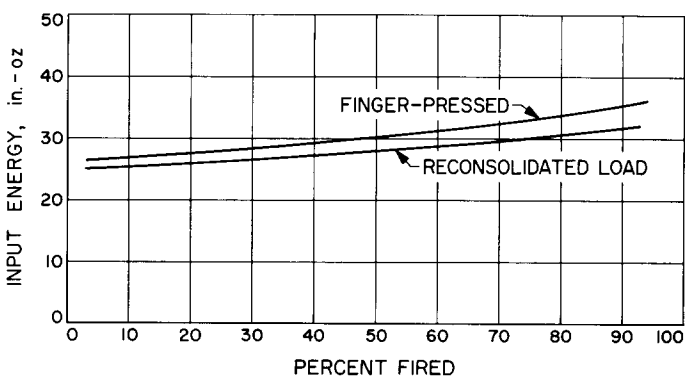

Fig. 27. Comparison of energies required to fire 49G-11 primer finger-pressed into firing holder and those with reconsolidated pyrotechnic load

Table 2. Chemical composition of charge

Component	Percent composition	
	G-11	G-16
Potassium chlorate	53	53
Tacot	10	—
Antimony trisulfide	25	30
Calcium silicide	12	17

[a] Tacot is a proprietary high-temperature explosive developed by E. I. du Pont; it is added to one formulation to increase the sensitivity.

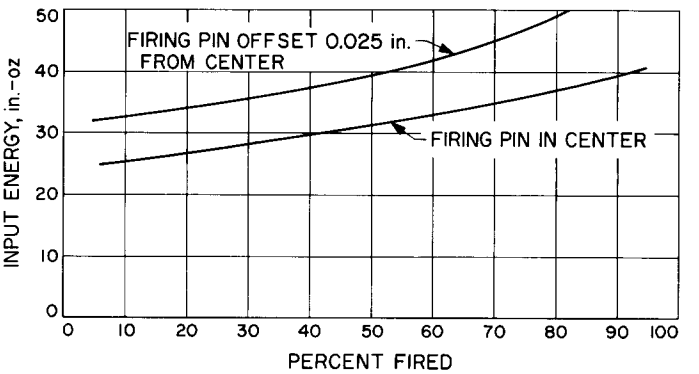

Fig. 28. Comparison of energies required to fire primers with firing pin in center and those with firing pin offset 0.025 in. from center

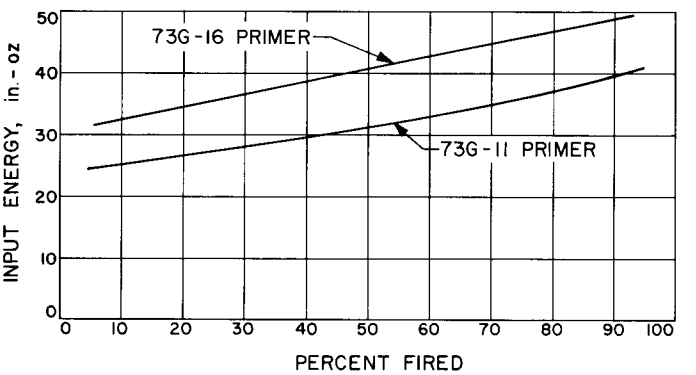

Fig. 29. Comparison of sensitivities of 73G-11 and 73G-16 primers (firing pin in center)

and the rifle use a firing pin with an 0.076-in. diameter. Since the tests conducted in the program had been made with a firing pin of 0.040-in. diameter, a short series of tests was performed to determine the effect of firing pin diameter on primer sensitivity. It was found that less input energy is required to fire the primers when the larger firing pin is used. A typical comparison of input energy values is shown in Fig. 30.

UNCLASSIFIED

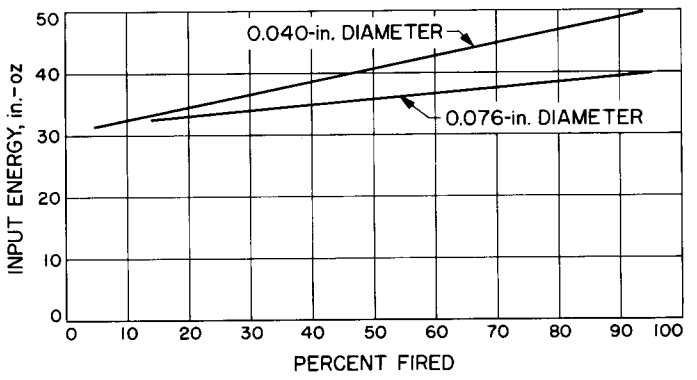

Fig. 30. Effect of firing pin diameter on input energy required to fire 73G-16 primers

2. *Analysis of Propellant Slosh Dynamics and Generation of an Equivalent Mechanical Model*

a. Introduction. Propellant sloshing is a potential source of spacecraft disturbances which may adversely affect the stability of the attitude-control subsystem during both powered and unpowered phases of flight. Sloshing refers to the free-surface oscillations of a fluid in a partially filled tank. These oscillations result from lateral and longitudinal displacements or angular motions of the spacecraft. The magnitude of the free-surface oscillations, and hence the forces and moments acting on the vehicle as a result of propellant motion, depend upon several factors. The most significant parameters influencing propellant slosh are the following: (1) tank geometry, (2) propellant properties, (3) slosh damping, (4) depth of propellant in the tank, (5) acceleration field, and (6) perturbed motion of the spacecraft.

Since current *Voyager* spacecraft designs envisage liquid propulsion systems with propellant loads of up to 60% of the total planetary vehicle mass, sloshing can be expected to be a potential source of disturbances. Various theoretical and analytical investigations have shown that sloshing waves can be large enough to produce forces whose magnitude and phase can cause instabilities in closed-loop control systems. The addition of baffles to the tanks will provide damping, if required, and is expected to limit the resultant slosh to an acceptable value.

Analysis of the coupled response of the spacecraft attitude-control subsystem and propellant free-surface oscillations requires either: (1) an equivalent mechanical model for the fluid system, or (2) a transfer function for the forces and moments produced by the propellant motion in response to an input excitation. The effort reported herein concerns the matter of obtaining the aforementioned analytical tools for use in the analysis of control system dynamics. All analysis to date has been concerned with propellant motion during the powered phases of flight.

The linearized dynamic equations of propellant motion in the gravity-force-dominated regime have been developed for a cylindrical tank approximation of the lunar excursion module descent system (LEMDS) tankage. An equivalent mechanical model consisting of a fixed mass and an infinite series of springs and masses has been generated. This model will, in the limit of infinite series, duplicate the forces and moments on a tank resulting from propellant slosh in response to a lateral input motion, and will closely approximate most fluid dynamic situations when truncated to only two terms.

The natural frequency of the propellant motion has been shown to be dependent upon the tank diameter, acceleration magnitude, and fluid depth; it has been found to be independent of fluid density. The maximum natural frequency of propellant motion for a nominal 1973 *Voyager* spacecraft, flying a nominal mission profile, has been found to be 4.25 rad/sec ($\approx$0.68 cps) and to prevail during the orbit insertion maneuver. The minimum natural frequency for these nominal conditions is approximately 1 rad/sec ($\approx$0.16 cps) and occurs at the end of orbit trim. The propellant slosh mass has been found to be essentially independent of acceleration and dependent upon tank radius, residual propellant mass per tank, and, consequently, the depth of propellant in a given tank.

b. Analysis. The determination of the forced oscillations of a fluid assumed to be inviscid and irrotational in a tank of arbitrary shape consists of a solution for a velocity potential function which satisfies: (1) Laplace's equation in the region of space occupied by the fluid, and (2) certain boundary conditions on the surfaces enclosing the region occupied by the fluid. Since the situation consists of a boundary-value problem in differential equations, the solution can become extremely difficult to obtain in closed form if the geometry of the problem cannot be simplified so as to display symmetry in a standard coordinate system (i.e., cartesian, spherical, or cylindrical).

The LEMDS propellant tanks, the subject of the current investigation, consist of two hemispherical end caps with a cylindrical section between them. Since this geometry

UNCLASSIFIED

UNCLASSIFIED

does not lead to a simple mathematical description of the bounding surface, an equivalent tank with symmetry in cylindrical coordinates and a flat bottom was constructed as a means for approximating the slosh properties of the actual tank. This equivalent cylindrical tank has the properties that its diameter is equivalent to the diameter of the cylindrical section of the LEMDS tank and its internal volume is equivalent to the internal volume of that tank. A graphical representation of this approximation is shown in Fig. 31.

It is of interest to determine *a priori* the relevant forces that will influence the fluid motion so that irrelevant forces can be neglected in the dynamic equations, thereby simplifying the problem. Viscous forces will be neglected since the Reynolds number for the assumed tanks is of the order of 10^5. Surface tension forces can, however, become important in low-gravity environments. An estimation of the Bond number (ratio of gravity to capillary forces) furnishes information on the relative importance of surface tension and gravity forces in the problem at hand. The Bond number, based on the tank radius r, is given by:

$$B_0 = \frac{\rho g r^2}{\sigma g_c}, \tag{1}$$

where ρ is the liquid density; g, the longitudinal acceleration field; and σ, the surface tension. (These and other symbols used in this article are also defined in Table 3 on page 84.) For the LEMDS tanks, $r = 2.25$ ft, $\rho(N_2O_4) = 90.48$ lbm/ft^3, $\sigma = 2.18 \times 10^{-3}$ lbf/ft. Therefore,

$$B_0 = 1.9 \times 10^5 \left(\frac{g}{g_c}\right) = 2.1 \times 10^5 \left(\frac{F}{M}\right). \tag{2}$$

Thus, the thrust/mass ratio of the spacecraft would have to be of the order of 10^{-5} g before the Bond number of an oxidizer tank would approach unity. Although surface tension may well influence the hydrodynamics for Bond numbers on the order of 100, it can still be seen that, for any reasonable thrust/mass ratio (say, $> 10^{-3}$ g), one would not expect surface tension to exert any detectable influence upon the propellant motion during the powered phases of the mission. Therefore, surface tension forces have also been neglected in the current analysis.

The problem can therefore be stated as follows: Determine a velocity potential function ϕ which satisfies the following conditions:

$$\nabla^2\phi = 0 \text{ in } \begin{cases} 0 \leqq r \leqq a \\ 0 \leqq \theta \leqq 2\pi \\ -h \leqq z \leqq 0 \end{cases} \tag{3}$$

subject to the boundary conditions that

$$\frac{\partial \phi}{\partial r} = 0 \text{ on } r = a, \tag{4}$$

$$\frac{\partial \phi}{\partial z} = 0 \text{ on } z = -h, \tag{5}$$

$$\frac{\partial^2 \phi}{\partial t^2} + g\frac{\partial \phi}{\partial z} = -\ddot{u}_0 x \text{ on the free surface.} \tag{6}$$

The solution of Eq. (3), subject to Eqs. (4), (5), and (6), can be obtained by a standard separation-of-variables method. It has been shown[1] that the solution for the velocity potential function of the (mn) mode of slosh can be represented by:

$$\phi_{mn} = \left[C_{mn}\cos(m\theta) + D_{mn}\sin(m\theta)\right] \times J_m(\lambda_{mn} r)\frac{\cosh\left[\lambda_{mn}(z+h)\right]}{\cosh\left[\lambda_{mn} h\right]} T_{mn}(t), \tag{7}$$

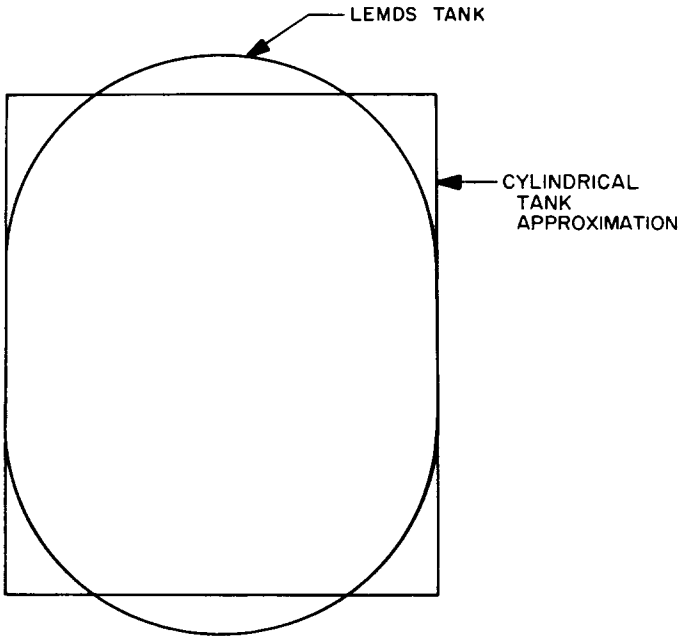

Fig. 31. Cylindrical tank approximation of the LEMDS propellant tank

[1]This solution is developed in detail in Lance, T. A., *Analysis of Propellant Slosh Dynamics and Generation of an Equivalent Mechanical Model For Use in Preliminary Voyager Autopilot Design Studies*, Technical Memorandum No. 33-306, Jet Propulsion Laboratory, Pasadena, California (To be published).

UNCLASSIFIED

UNCLASSIFIED

where $T_{mn}(t)$ is an unknown function of time (which depends upon the input excitation) through the free-surface boundary conditions. The most general solution is, then:

$$\phi = \sum_{m=1}^{\infty} \sum_{n=1}^{\infty} \phi_{mn} .$$

In certain cases, all but one or two of the (mn) modes may be neglected. In the case of a lateral input excitation, experiments have shown that the first asymmetric mode will be the major contributor to forces and torques on the propellant tanks. Less than 3% of the total sloshing mass is usually associated with the higher-order $(n = 2, 3, \cdots, \infty)$ modes.

If the lateral excitation is assumed to be sinusoidal, it can be represented as:

$$u_0 = \epsilon_0 \omega \cos(\omega t) . \tag{8}$$

The unknown function of time then becomes

$$T_{1n} = \frac{\epsilon_0 \omega^3 F_n}{p_{1n}^2 - \omega^2} \cos(\omega t) , \tag{9}$$

where F_n is given by

$$F_n = \frac{2a}{(\lambda_{1n}^2 a^2 - 1) J_1(\lambda_{1n} a)} ,$$

and the velocity potential becomes

$$\phi = \sum_{n=1}^{\infty} \frac{2\epsilon_0 \omega^3 a}{(\lambda_{1n}^2 a^2 - 1)(p_{1n}^2 - \omega^2)} \frac{J_1(\lambda_{1n} r)}{J_1(\lambda_{1n} a)} \times \frac{\cos[\lambda_{1n}(z + h)]}{\cos[\lambda_{1n} h]} \cos\theta \cos(\omega t) , \tag{10}$$

where only the first asymmetric mode has been considered.

In Eq. (10) above, p_{1n} is the natural circular slosh frequency and is given by:

$$p_{mn} = [g\lambda_{mn} \tanh(\lambda_{mn} h)]^{1/2} \tag{11}$$

and ω is the frequency of the forcing function. It is apparent from inspection of Eq. (10) that, as ω approaches p, the solution becomes unbounded. Actually, in the region $|p| - |\omega| < \epsilon$, where ϵ is a small number, the linearized theory breaks down and the current analysis will not apply.

c. Construction of an equivalent mechanical model. An equivalent mechanical model can be developed by performing the following operations: If we take Euler's equation in the form

$$\frac{\partial \phi}{\partial t} + \frac{1}{2}(\nabla\phi \cdot \nabla\phi) + \dot{u}_0 x + \dot{v}_0 y + \dot{w}_0 z + gz + \frac{p}{\rho} = 0 \tag{12}$$

and, linearizing by assuming that the squares of the velocity terms can be neglected and also that $\dot{v}_0 = \dot{w}_0 = 0$, solve for the pressure term, we get:

$$p(t) = \rho\left[\frac{-\partial\phi}{\partial t} - \ddot{x}_0 r \cos\theta - gz\right] . \tag{13}$$

If the static pressure term gz is neglected, we can take the Laplace transform of Eq. (13) to obtain:

$$p(s) = [-\rho s\phi(s) + s^2 r \cos\theta\, x_0(s)] . \tag{14}$$

Further, taking the transform of the velocity potential function (Eq. 7), we get:

$$\phi(s) = \frac{-2as^3 x_0(s)}{(s^2 + p^2) J_1(\lambda_n a)(\lambda_n^2 a^2 - 1)} J_1(\lambda_n r) \frac{\cosh[\lambda_n(z + h)]}{\cosh(\lambda_n h)} \cos\theta . \tag{15}$$

Substituting Eq. (15) into Eq. (14) and integrating the x-component of the pressure force over the wetted surface of the tank, we obtain the transform of the sum of the forces in the x-direction:

$$F_x(s) = \int_{z=-h}^{0} \int_{\theta=0}^{2\pi} p(t)\, a \cos\theta\, d\theta\, dz \tag{16}$$

or, performing the indicated operations,

$$F_x(s) = -ms^2 x_0(s) + m \frac{2s^4 x_0(s) \tanh(\lambda_n h)}{\lambda_n h (s^2 - p^2)(\lambda_n^2 a^2 - 1)} . \tag{17}$$

UNCLASSIFIED

UNCLASSIFIED

Similarly, by integrating the infinitesimal pressure forces multiplied by their respective perpendicular distances from the y-axis, we obtain the total moment around the y-axis:

$$M_0(s) = \int_{r=0}^{a} \int_{\theta=0}^{2\pi} \rho(s) r^2 \cos\theta \, d\theta \, dr + \int_{\theta=0}^{2\pi} \int_{z=-h}^{0} p(s) z a \cos\theta \, d\theta \, dr \tag{18}$$

where the first integrand is evaluated at $z = -h$ and the second at $r = a$. Therefore, we obtain:

$$M_0(s) = m\left(\frac{h}{2} - \frac{a^2}{4h}\right) s^2 x_0(s) + ms^4 x_0(s) \left\{ \frac{2\left[2 - \cosh(\lambda_n h)\right]}{\lambda_n^2 h \left(\lambda_n^2 a^2 - 1\right)\left(s^2 + p^2\right) \cosh(\lambda_n h)} \right\}. \tag{19}$$

Since experimental studies reported in the literature have shown that the fluid velocity decreases exponentially with depth [a fact which is verified by the exponential dependence of the velocity potential function upon depth through the hyperbolic functions (see Eq. 15)], one might suspect that the fluid dynamics of propellant slosh in response to a lateral input excitation might be represented by a fixed mass and an infinite series of oscillating spring masses. Such a system is shown schematically in Fig. 32. The infinite series of spring masses can be chosen so that each represents a single slosh mode and the series can, therefore, be truncated at any desired accuracy. In practice, it has been found that usually only one spring mass is required, since only a small percentage of the total slosh mass is associated with higher-order modes.

If one develops the equations of motions for this spring-mass system, the following expressions are obtained (in transform notation):

$$F_x(s) = s^2 x_0(s)\left(m_0 + \Sigma m_n\right) + s^4 \sum \frac{m_n x_0(s)}{s^2 + \omega_n^2}, \quad n = 1, 2, \cdots, \infty, \tag{20}$$

$$M_0(s) = -s^2 x_0(s)\left[m_0 d_0 - \Sigma m_n \left(d_n + \frac{g}{\omega_n^2}\right)\right] + s^4 x_0(s) \sum \frac{m_n \left(d_n + \frac{g}{\omega_n^2}\right)}{s^2 + \omega_n^2}. \tag{21}$$

Comparison of Eq. (17) with Eq. (20) and Eq. (19) with Eq. (21) shows that, for dynamic similarity between the fluid system and the equivalent mechanical system to exist, the following relationships relative to the parameters describing the mechanical model must be satisfied:

$$\omega_n = p_n, \tag{22}$$

$$m_n = mA_n, \tag{23}$$

$$m_0 = m\left(1 - \Sigma A_n\right), \tag{24}$$

$$d_n = \frac{2\left[1 - \cosh(\lambda_n h)\right]}{\lambda_n \sinh(\lambda_n h)}, \tag{25}$$

$$d_0 = \frac{B + \Sigma B_n}{1 - \Sigma A_n}, \tag{26}$$

where

$$A_n = \frac{2\tanh(\lambda_n h)}{\lambda_n h\left(\lambda_n^2 a^2 - 1\right)},$$

$$B = \left(\frac{a^2}{4h} - \frac{h}{2}\right), \tag{27}$$

$$B_n = \frac{2\left(2 - \cosh\lambda_n h\right)}{\lambda_n^2 h\left(\lambda_n^2 a^2 - 1\right)\cosh(\lambda_n h)}.$$

d. Application to a typical Voyager mission. Figs. 33 through 40 show the results of calculations for a typical 200-m/sec midcourse maneuver, a 2-km/sec retromaneuver, and a 200-m/sec orbit trim (with the capsule off). The spacecraft characteristics assumed for these computations were typical of those for a 1973 *Voyager* mission with a 3000-lbm capsule. The following specific masses were assumed: spacecraft bus and payload: 2500 lbm,

UNCLASSIFIED

UNCLASSIFIED

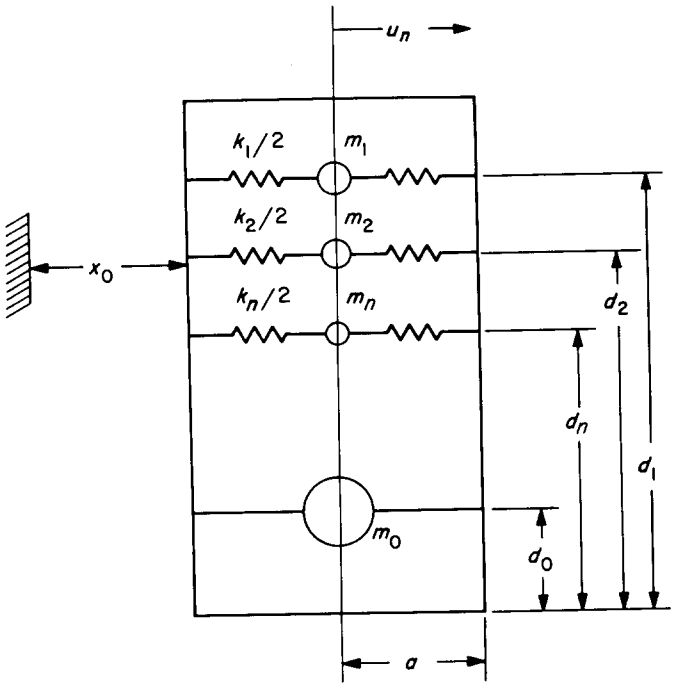

Fig. 32. Equivalent spring-mass system for propellant slosh in a cylindrical tank

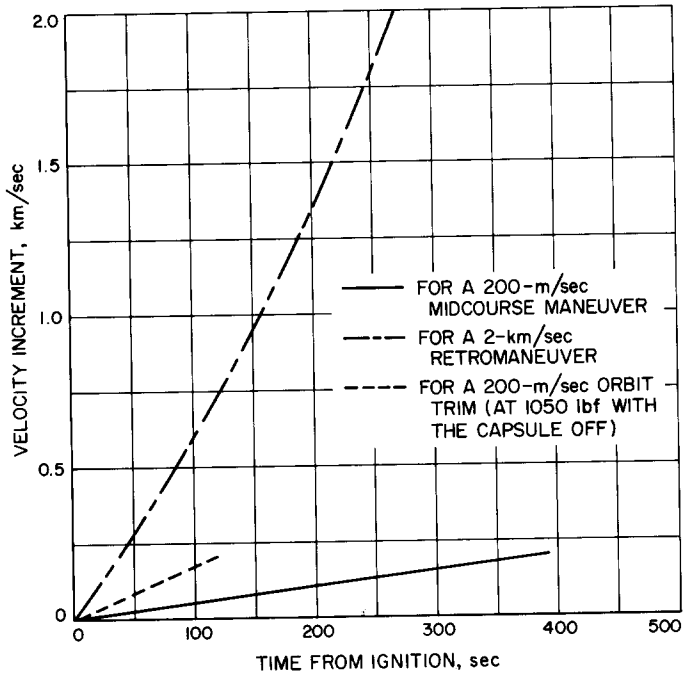

Fig. 33. Velocity increment vs time from ignition

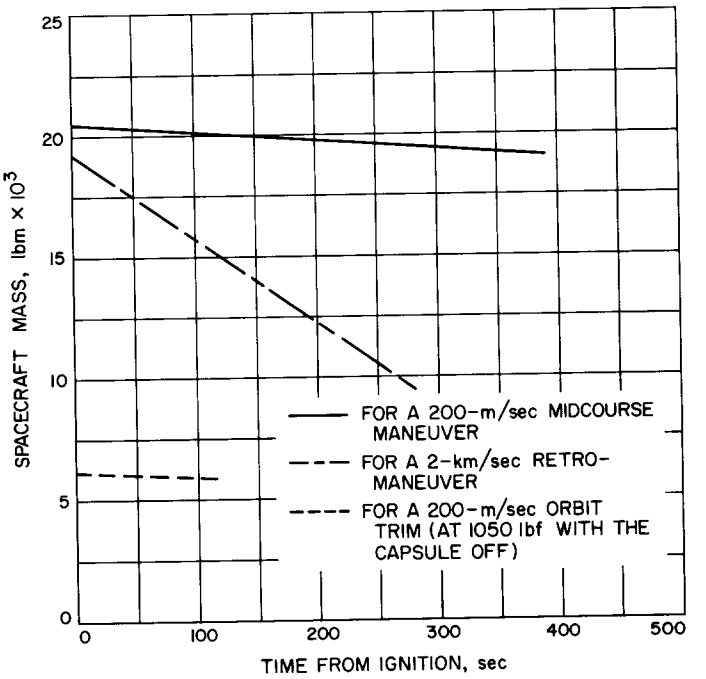

Fig. 34. Spacecraft mass vs time from ignition

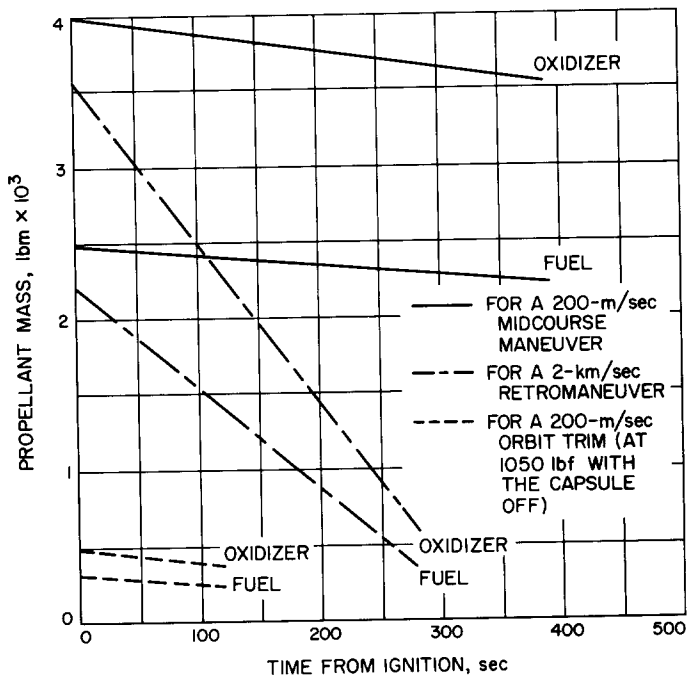

Fig. 35. Propellant mass vs time from ignition

spacecraft propulsion: 15,000 lbm, flight capsule: 3000 lbm, and total planetary vehicle: 20,500 lbm. It was further assumed that 12,914 lbm of propellant were tanked and that this propellant was contained in four equal-volume cylindrical tanks of 51-in. diameter (two oxidizer and two fuel). These tanks constitute the cylindrical tank approximation of the LEMDS tankage. The 12,914 lbm of propellant represent a mass fraction of

UNCLASSIFIED

UNCLASSIFIED

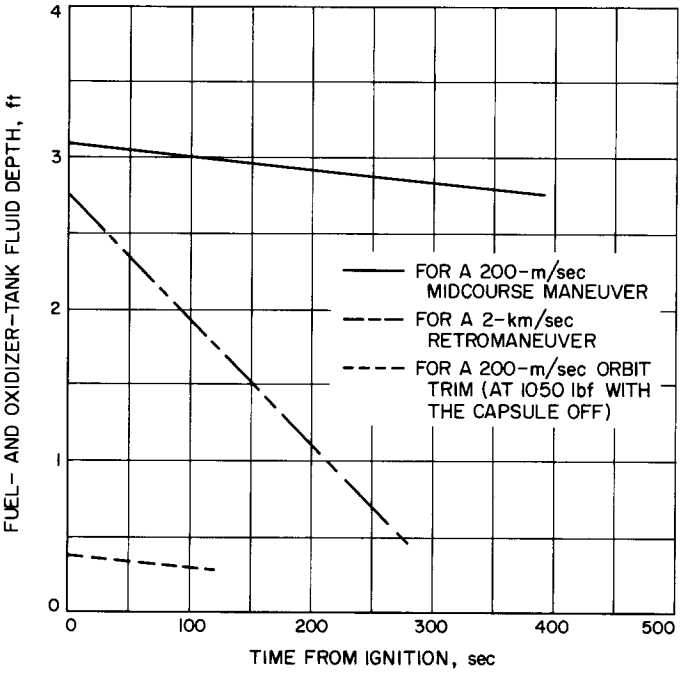
FUEL- AND OXIDIZER-TANK FLUID DEPTH, ft
TIME FROM IGNITION, sec
FOR A 200-m/sec MIDCOURSE MANEUVER
FOR A 2-km/sec RETROMANEUVER
FOR A 200-m/sec ORBIT TRIM (AT 1050 lbf WITH THE CAPSULE OFF)

Fig. 36. Fuel- and oxidizer-tank fluid depth vs time from ignition

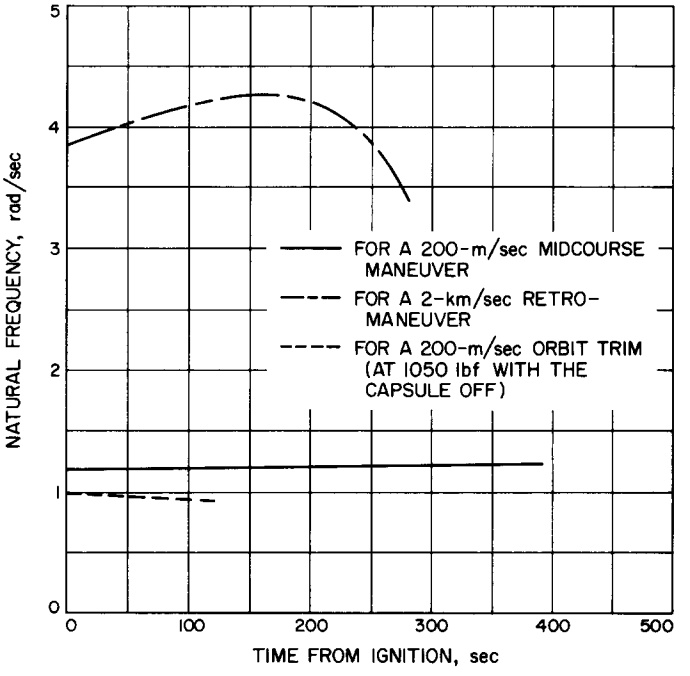
NATURAL FREQUENCY, rad/sec
TIME FROM IGNITION, sec
FOR A 200-m/sec MIDCOURSE MANEUVER
FOR A 2-km/sec RETRO-MANEUVER
FOR A 200-m/sec ORBIT TRIM (AT 1050 lbf WITH THE CAPSULE OFF)

Fig. 37. Fuel- and oxidizer-tank natural frequency vs time from ignition

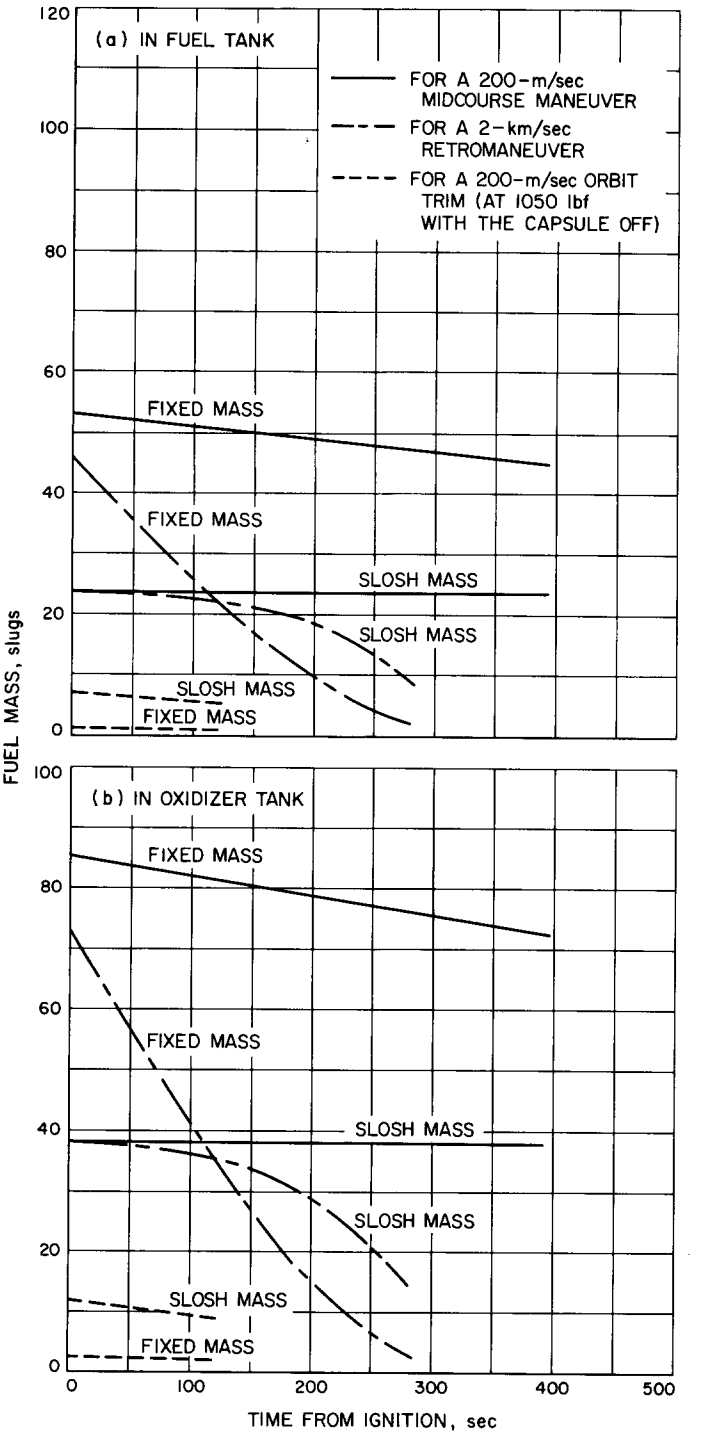

Fig. 38. Fixed and slosh masses in the fuel and oxidizer tanks vs time from ignition

0.86, which does not exceed the capability of the current LEMDS tanks. The propellants assumed were a 50–50 blend of hydrazine and unsymmetrical-dimethylhydrazine with a density of 56.78 lbm/ft^3 and nitrogen tetroxide with a density of 90.48 lbm/ft^3.

In these plots, it was assumed that the 200-m/sec midcourse maneuver was performed by the LEMDS en-

UNCLASSIFIED

UNCLASSIFIED

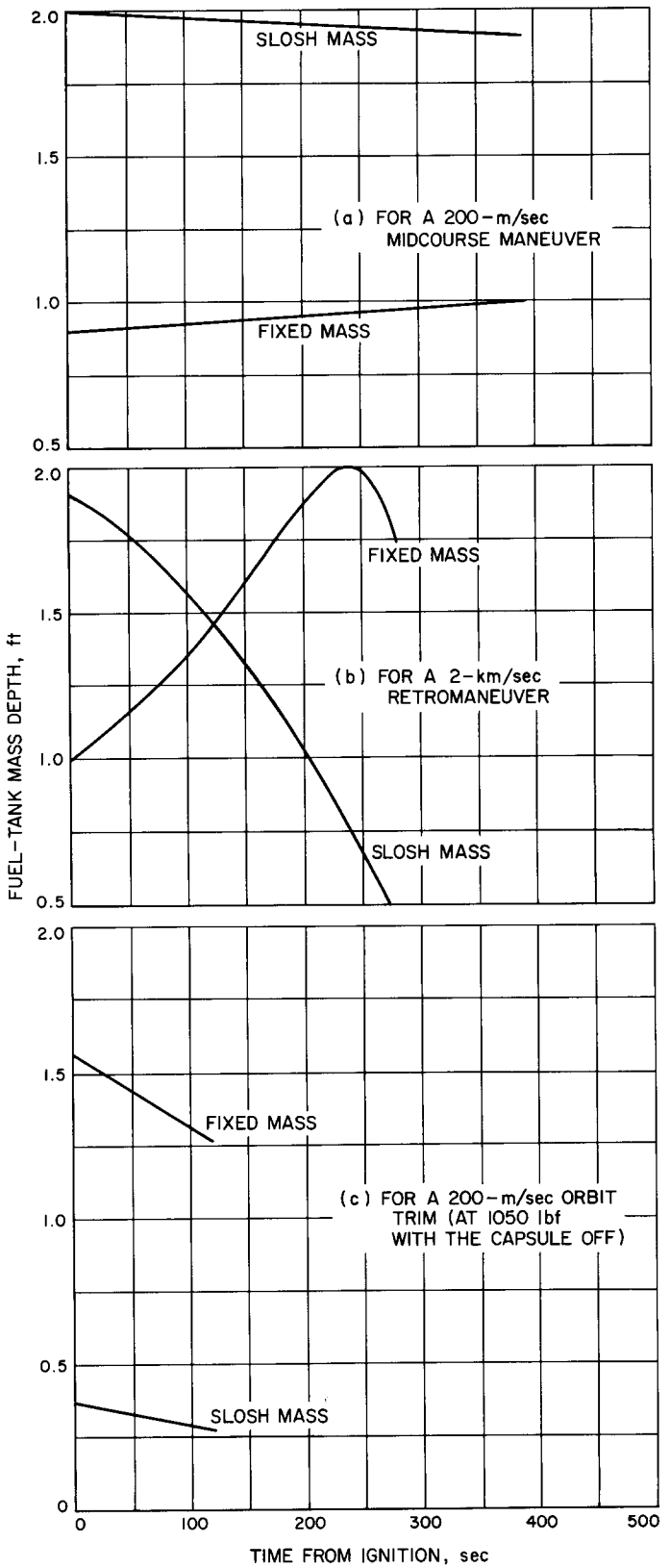

Fig. 39. Fixed and slosh mass depth in the fuel tank vs time from ignition

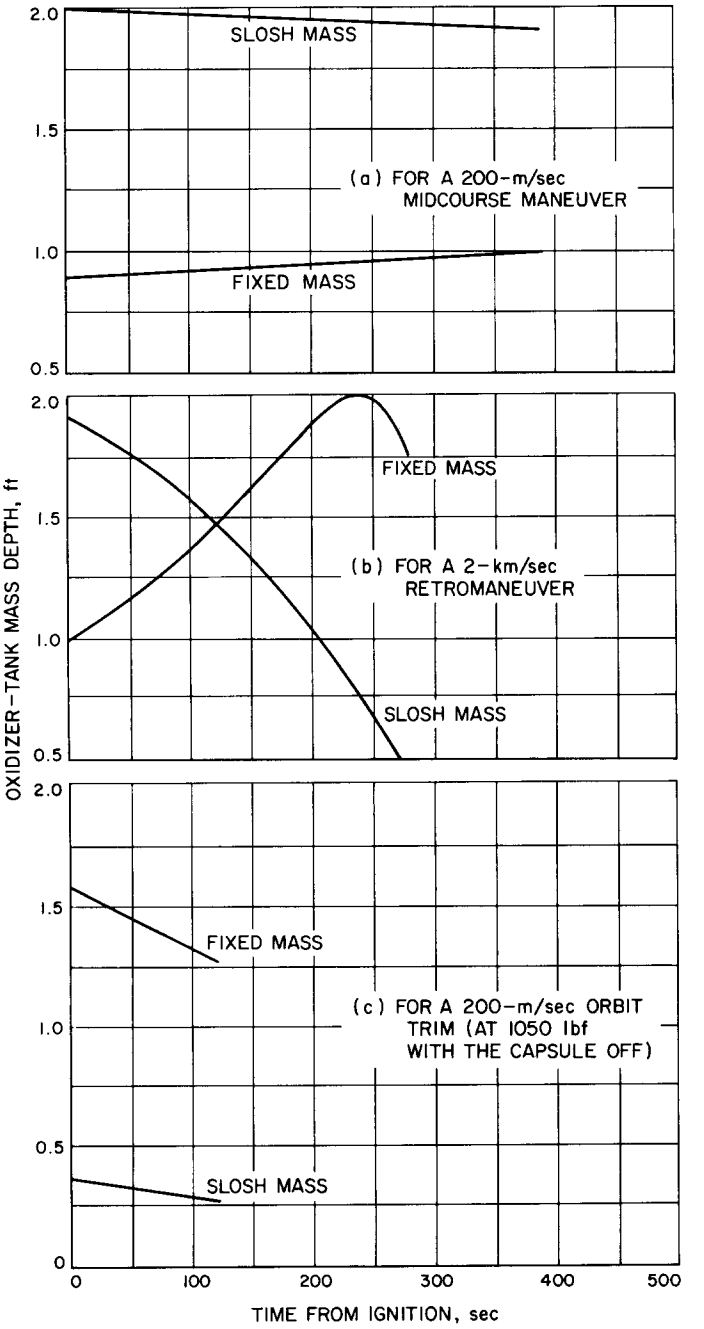

Fig. 40. Fixed and slosh mass depth in the oxidizer tank vs time from ignition

gine operating at 1050-lbf thrust, 1.6 mixture ratio, and 302-lbf-sec/lbm specific impulse. For the 2-km/sec retromaneuver, the spacecraft mass at retro-ignition was assumed to be the residual mass at midcourse thrust termination. In this case, however, the thrust was assumed to be 10,500 lbf. For the 200-m/sec orbit trim, calculations were made for 1050-lbf thrust with capsule off.

UNCLASSIFIED

Fig. 33 shows the velocity increment versus time from ignition; Fig. 34 shows spacecraft mass versus time from ignition; and Fig. 35 depicts residual fuel and oxidizer mass during each maneuver. The fuel- and oxidizer-tank fluid depth plot in Fig. 36 shows that the tanks are being depleted at approximately the same rate with the assumed mixture ratio and propellant densities. In Fig. 37, which shows the fuel- and oxidizer-tank natural frequencies, it is interesting to note that, for the assumed conditions, the frequencies of the tanks are identical. This is to be expected since the natural frequency for a given mode is a function of the tank diameter, acceleration field, and fluid depth only; i.e., it is independent of density. Since the assumed conditions were equal-diameter tanks and equal volumetric mixture ratio, the natural frequencies of the fuel and oxidizer tanks are identical.

It can also be seen in Fig. 37 that the natural frequencies change very little during the midcourse maneuver. This results from the fact that, during the midcourse maneuver, only about 10% of the total propellant load is expended and, therefore, the tank fluid depths change very little while the acceleration increases by less than 8%. Further, these effects tend to cancel each other.

It should be noted that the natural frequencies of the propellant tanks increase from about 1.22 rad/sec at the end of the midcourse maneuver to 3.87 rad/sec at the start of the retromaneuver. Inspection of Eq. (11) shows that the natural frequency is proportional to the square root of the acceleration. Since thrust has been increased by an order of magnitude for the retromaneuver, one would expect the frequency to increase by the square root of 10. It can also be noted that the natural frequency of the tanks exhibits a maximum of 4.25 rad/sec at about 175 sec into the retromaneuver.

Fig. 38 shows the fixed and slosh masses as functions of time from ignition for the fuel and oxidizer tanks. It can be seen from these plots that, for the midcourse maneuver, the slosh mass remains approximately constant while the fixed mass is depleted. This corresponds to the physical observation that, for relatively deep liquid levels, most of the fluid motion takes place near the free surface, while the fluid near the bottom of the

Table 3. Definition of symbols

a	cylindrical tank radius
a_0	acceleration of tank relative to a fixed coordinate system
B_0	Bond number
C, D	undetermined coefficients
d_0, d_1	location of rigid and first-mode sloshing masses
F	thrust
F_x	force in x-direction
g	longitudinal acceleration field
g_c	force–mass conversion constant
h	fluid depth
J_m	Bessel function of the first kind of order m
k_n	nth-order sloshing mass-spring constant
M	moment
m	total fluid mass or separation constant
m_0	rigid mass
m_1	sloshing mass (first mode)
p	fluid pressure, or natural fluid oscillation frequency
r	tank radius
s	dummy variable in Laplace transform
T	unknown function of time
t	time
u_n	velocity of the nth sloshing mass relative to the tank
u_0	velocity of tank in the x-direction
v_0	velocity of tank in y-direction
w_0	velocity of tank in z-direction
x	x coordinate
y	y coordinate
z	distance from free surface (+ downward into fluid)
Greek symbols	
ϵ_0	small displacement
θ	circumferential coordinate
λ	separation constant
ρ	liquid density
ϕ	velocity potential
ω	tank excitation frequency or spring–mass natural frequency
σ	surface tension
Subscripts	
m	mth-order mode of vibration in the θ-direction
n	nth-order mode of vibration in the r-direction

UNCLASSIFIED

tank is nearly quiescent. Thus, the mechanical model represents, at least qualitatively, this particular physical phenomenon. In Fig. 38, it can be seen that the propellant slosh and fixed masses are equal at the end of the midcourse maneuver and the start of the retromaneuver, even though the acceleration has increased by a factor of 10. Inspection of Eqs. (23) and (24) shows that these masses are independent of acceleration.

Figs. 39 and 40 show the locations of the attachment points for the fixed and slosh masses in the fuel and oxidizer tanks, respectively.

Reference

1. Stevenson, T., and Ciccone, T. Q., (Chemical Research Laboratory, Frankford Arsenal, Philadelphia, Pennsylvania), "High Temperature Percussion Primers for PAD Systems," *Proceedings of the Electric Initiator Symposium*, 1963.

UNCLASSIFIED

UNCLASSIFIED

IV. Future Projects

A. Introduction

The JPL Future Projects Office is responsible for the direction, sponsorship, and, in cooperation with other elements of the Laboratory, origination of advanced mission and future project studies in the areas of interest and applicability to the Laboratory. The objective of this effort is to ensure that preliminary technical information and plans for the various potential missions, together with associated information on spacecraft systems, instrumentation systems, launch vehicle systems, resources, and schedule, be available as required. This preliminary mission study information will be used primarily for defining specific flight mission programs and as generalized guidance for the Laboratory research and advanced development programs.

Each such study has been, and will continue to be, documented in a formal final report. Provided here is an abstract or summary of the results of each such study, including, where appropriate, reference to the final report for additional details.

B. Science Planning for a Venus/Mercury Swingby Mission[1]

1. Introduction

It has been proposed by Minovitch (Ref. 1) and Hunter (Ref. 2) that trajectories using the gravitational perturbations of Venus can be used to achieve a lower-launch-velocity mission to Mercury. For example, an analysis of the 1970 opportunity by Cutting and Sturms (Ref. 3) suggests a distance of closest approach to the surface of Venus (depending on the time of launch within the 30-day launch period studied) ranging from 1500 to 3300 km, with the total flight time to Mercury ranging from 158 to 182 days. The communications distance at Mercury encounter for this opportunity would be about

[1]This article forms a summary of Engineering Planning Document No. 409, *Venus/Mercury Swing-By With Venus Capsule, Preliminary Science Objectives and Experiments for Use in Advanced Mission Studies,* by Roy G. Brereton, et al.

UNCLASSIFIED

UNCLASSIFIED
CONFIDENTIAL

175×10^6 km. Similar calculations made for other opportunities in the 1970's suggest flyby distances from both Venus and Mercury that are very favorable for scientific observations. Further, these trajectories provide an opportunity for an occultation experiment at Venus and, under limited circumstances, at Mercury and the outer portion of the solar corona.

The launch vehicle that can be assumed for this mission would likely have at least the capabilities of an *Atlas/Centaur*; this means the spacecraft would be the same type as the *Mariner* Mars 1964 spacecraft, weighing over 1300 lb for the 1970 opportunity and 1000 lb for the 1973 opportunity. In the event an improved *Atlas/Centaur* launch vehicle is available for the 1973 opportunity, the spacecraft weight could be increased to approximately 1700 lb. This spread in launch vehicle capability suggests a scientific payload weight of perhaps 125 lb minimum and at least 200 lb maximum. It further suggests the possibility of designing for more than a simple Venus/Mercury swingby mission: possibly a Venus/Mercury swingby with a Venus capsule.

The primary objectives of planetary science are to obtain an understanding of: (1) the origin and evolution of life, (2) the origin and evolution of the solar system, and (3) the physical processes that determine the terrestrial environment. For this particular mission, it is believed that experiments relating to objectives (2) and (3) should have the highest priority. Thus, although Venus cannot be ruled out as a possible abode for life, the most practical scientific experiments for this mission would be those investigating the composition, pressure, temperature, and structure of the planet's atmosphere and the nature of its surface. Information of this type should be relevant to the biological problem, while simultaneously contributing to a better understanding of cosmogony and terrestrial problems. Investigation of Mercury should provide information for a better understanding of the atmosphere, surface, and mass density of the planet. The latter is particularly relevant to certain facets of the cosmogonical problem, and a solution seems practical from this mission.

2. Scientific Payload

Several specific scientific experiments to satisfy the planetary science objectives are discussed here. As indicated earlier, the mission profile can be either a Venus/Mercury swingby or a Venus/Mercury swingby with a Venus capsule, the latter profile requiring a division of scientific payload between swingby science and capsule science. Table 1 presents typical swingby science for a Venus/Mercury swingby mission; Table 2 presents typical Venus capsule science; and Table 3 presents select swingby experiments for a so-called minimum swingby–capsule mission.

An effort has been made to select preferentially those scientific instruments that: (1) can provide meaningful experimental information about both Venus and Mercury, or (2) take special advantage of this particular mission. Also, because this mission presents an unusual opportunity to investigate the interplanetary environment close to the Sun (and maybe over a time period coincident with maximum activity on the Sun), a considerable portion of the scientific payload has been allocated to these experiments. Attempts to design a worthwhile scientific payload for a combined Venus/Mercury swingby mission are confounded by the fact that one planet has an extensive atmosphere and the other has almost no atmosphere; further, the trajectory offers a very close swingby distance for Venus, but a more distant one for Mercury. However, as shown in Table 1, the selection of a worthwhile payload is quite feasible.

A close Venus swingby miss distance would be best for such experiments as the ultraviolet spectroscopy, microwave spectrometer, magnetometer, trapped radiation detector, and perhaps RF occultation experiments. However, the photo-imaging experiment, because it is optimized for a greater Mercury swingby distance, would have very limited, but high-resolution, area coverage for Venus at distances close to the planet. From considerations of the probable trajectory and of the resolution versus areal coverage versus scientific objectives for each of the experiments, a Venus swingby miss distance of 5000 km seems practicable for this mission; however, a miss distance of up to 10,000 km would be satisfactory.

For Mercury, a swingby miss distance of 5000 km is considered optimum, but a miss distance of up to 40,000 km would be satisfactory. The selected Mercury swingby distance and trajectory must offer a good opportunity to determine the mass of the planet: a most important scientific objective of this mission. Also, the desirability of a Mercury occultation experiment should be noted. It is expected that the wide dispersion of swingby distances quoted above will be compatible with several Venus/Mercury swingby opportunities for the period extending through the 1970's.[2]

[2]Private communication with F. M. Sturms, a member of JPL Technical Section 312.

CONFIDENTIAL
UNCLASSIFIED

UNCLASSIFIED

Table 1. Typical scientific experiments for a Venus/Mercury swingby mission

Experiment	Scientific objectives		Weight, lb	Power, w
	Venus	Mercury		
Photo-imaging experiment	To provide information about the nature and structure of an atmosphere of Venus (similar to data from early U.S. weather satellites for Earth)	To obtain television pictures of the planetary surface to a resolution of about 150 m/TV line; to photograph entire visible disk of planet to obtain diameter; and, from this information in conjunction with mass from trajectory, to obtain an order-of-magnitude density determination	15	20
Microwave spectrometer (multifrequency instrument)	To obtain limb-to-limb brightness temperature at several wavelengths from 3 mm to 3 cm; and, from these data, to attempt to obtain information about the atmosphere, including composition, three-dimensional physical and thermal structure, circulation, and density	To obtain a three-dimensional thermal map of the planetary surface/subsurface; and, at shorter wavelengths, to possibly obtain information on temperature, pressure, and density of the planetary atmosphere	35	10
Ultraviolet spectrometer	To determine the abundance and distribution of upper atmospheric constituents obtained from ultraviolet spectra of the planets		25	12
RF occultation	To measure changes at several frequencies of spacecraft radio signal resulting from occultation of spacecraft by Venus and perhaps Mercury and the Sun; and to obtain atmospheric scale heights for Venus and Mercury and the planetary diameter for Mercury.		—[a]	—[a]
Relativity experiment	To measure changes in range signal between space probe and Earth resulting from relativistic effect when range signal passes near the Sun		—[b]	—[b]
Magnetometer	To investigate planetary and interplanetary magnetic fields, including their relationship, characteristics, magnitude, direction, and orientation		5	5
Solar plasma probe	To make detailed energy and flux measurements (similar to the *Orbiting Geophysical Observatory E* plasma experiment)		7–15	5–10
Trapped radiation detector	To determine intensity, direction, and spatial distribution of planetary trapped radiation and interplanetary cosmic rays		2.6	0.7
Micrometeoroid detector	To measure flux of cosmic dust particles as a function of direction, distance from Sun, and momentum with respect to spacecraft		5	0.5
Particle flux/ionization chamber	To monitor total ionizing radiation, including energy and particle type, with time and position in interplanetary space		2.5	0.35
Cosmic ray and solar-charged particle telescope	To measure ion energy and spectra of cosmic rays and solar-charged particles		3.0	0.4
Planetary mass	To determine the mass of the planets		—[b]	—[b]
Topside sounder	To detect low-frequency spherics and radio emission that may contribute to microwave brightness temperature; and to study properties of the ionosphere (possibly giving altitude)	To study properties of the ionosphere	10	5
Bistatic radar	To investigate surface characteristics and the diameters of the planets		5–10[c]	5
Low-energy proton telescope	To measure the energy spectrum of low-energy solar protons		12.0	1.0

[a] For a simple experiment, no added equipment will be necessary; if changes at two additional frequencies are to be measured, perhaps 6-lb added equipment will be required.

[b] Not applicable.

[c] Dependent upon flyby distance.

UNCLASSIFIED

UNCLASSIFIED

Table 1. Typical scientific experiments for a Venus/Mercury swingby mission (cont'd)

Experiment	Scientific objectives		Weight, lb	Power, w
	Venus	Mercury		
Fast neutron and gamma ray detector	To measure the energy spectrum of fast neutrons and gamma rays (gamma ray data for Mercury could show the degree of concentration of radiative material in the crustal rocks)		10.0	1.5
Microwave spectrometer (surface imager)	To obtain a thermal map of a traverse of the Venusian surface at a wavelength longer than 3 cm; and, from these data, to possibly obtain information on planetary thermal abnormalities and an estimate of surface composition and structure	To obtain a thermal map of a traverse of the surface of Mercury at one wavelength; and, from these data, to possibly interpret the thermal and electrical properties of the planetary surface in terms of such qualities as geological processes and structure	25	10
Microwave spectrometer (combined multifrequency instrument and surface imager)	To obtain limb-to-limb brightness temperature at several wavelengths from 3 mm to 3 cm; and, from these data, to possibly obtain information about the atmosphere, including composition, three-dimensional physical and thermal structure, circulation, and density	To obtain a three-dimensional thermal map of the planetary surface/subsurface; and, at shorter wavelengths, to possibly obtain information on temperature, pressure, and density of the planetary atmosphere	50	40

Table 2. Typical scientific instruments for a Venus capsule

Instrument	Measurement capabilities	Approximate weight	Approximate power, w	Bits/sample and total information (Venus)
Aerometeorometer	Static temperature: 180–800° (measurement accuracy = ±1% of ambient temperature)	10 oz	0.07	9 bits/sample every 500 m
	Static pressure: 10 mbar to 100 atm (measurement accuracy = approximately 2%)	10 oz	0.10	15 bits/sample every 500 m
	Density: 2×10^{-4} to 30 kg/m^3 (measurement accuracy = ±1% of ambient)	15 oz	0.25	10 bits/sample every 500 m
	Velocity of sound: 250 to 380 m/sec (measurement accuracy = 1% of ambient)	10 oz	0.30	10 bits/sample every 500 m
Mass spectrometer	Determination of the composition of the atmosphere in the mass range of 12 to 50 atomic mass units	5 lb	6	1100 bits/sample; 550 bits total for complete analog spectra (bit rate can be reduced to 100 bits/sample)
Visual or ultraviolet photometer	Determination of the cloud tops and base and the optical properties of the planet's atmosphere	2 lb	1.0	7 bits/sample every 5 sec
Impactometer	Determination of a hard versus soft surface (e.g., unconsolidated sand-like material versus any consolidated surface)	3 lb	1.0	2-μsec pulses on the capsule carrier frequency
Three-axis accelerometer	Provision of data for determination of pressure-density-RT product as a function of altitude	3 lb[a]	1.0	40 bits/sample every 1-sec interval during supersonic flight and every 500 m during subsonic flight

[a] Including 5000-bit storage unit.

UNCLASSIFIED

UNCLASSIFIED

Table 3. Scientific experiments for a minimum swingby–capsule mission

Experiment	Scientific objectives		Weight, lb	Power, w
	Venus	Mercury		
Photo-imaging experiment	To provide information about the nature and structure of an atmosphere of Venus (similar to data from early U.S. weather satellites for Earth)	To obtain television pictures of the planetary surface to a resolution of about 150 m/TV line; to photograph entire visible disk of planet to obtain diameter; and, from this information in conjunction with mass from trajectory, to obtain an order-of-magnitude density determination	15	20
Microwave spectrometer	To obtain the limb-to-limb brightness temperature at a wavelength of 3 cm	To obtain a thermal map of the planetary surface	—[a]	—[a]
RF occultation	To obtain atmospheric scale heights for Venus and Mercury and the planetary diameter of Mercury		—[a]	—[a]
Micrometeoroid detector	To measure local dust density		2.5	0.2
Relativity experiment	To measure changes in range signal between space probe and Earth resulting from relativistic effect when range signal passes near the Sun		—[a]	—[a]
Planetary mass	To determine the masses of the planets		—[a]	—[a]
Magnetometer	To investigate planetary and interplanetary magnetic fields		5	5
Solar plasma probe	To measure quantity, rate, and energy of the positive-ion solar wind		5	2
Trapped radiation detector	To determine intensity, direction, and spatial distribution of planetary trapped radiation and interplanetary cosmic rays		2.5	0.7
Particle flux/ionization chamber	To monitor total ionizing radiation, including energy and particle type, with time and position in interplanetary space		2.5	0.5
Topside sounder	To detect low-frequency spherics and radio emission that may contribute to microwave brightness temperature; and to study properties of the ionosphere (possibly giving altitude)	To measure electron density of the ionosphere	2.5 to 10	5

[a] Not applicable.

Muhleman (*SPS 37-31*, Vol. IV, pp. 342–345) has suggested the possibility that Einstein's Theory of Gravitation may be tested by measuring the range between the Earth and a spacecraft when the range signal passes near the Sun. The effect is one of propagation somewhat related to the bending of star light by the solar gravitational field. Both instrumentation and trajectory considerations suggest that this is a feasible experiment for the Venus/Mercury mission. Since this is a fundamental experiment of great interest to the entire scientific community, it has a high priority in the list of experiments to be accomplished on this mission.

Nearly all of the constraints previously discussed for the swingby-only mission can be applied to the swingby–capsule mission; however, now the scientific payload must be divided between swingby science experiments that can provide meaningful information about both Venus and Mercury and the Venus capsule. Also, the total capsule weight, including the power supply, heat shielding, attitude stabilization (if required), retropropulsion (if required), and other required systems, must be considered as a part of the science payload. For the 1700-lb spacecraft, this combination mission would appear to be both feasible and very desirable in terms of scientific return. A typical combination here could consist of the first 14 swingby experiments in Table 1 plus the Venus capsule.

For the 1000-lb spacecraft, the combination mission appears to be very marginal, for the total scientific payload weight of, say, 125 lb must now be divided between

UNCLASSIFIED

UNCLASSIFIED

swingby experiments that are meaningful for both Venus and Mercury and the Venus capsule. The absolute minimum swingby science payload is given in Table 3. The total weight of the science payload is about 50 lb, leaving 75 lb for the capsule.

The capsule or drop sound can be instrumented to provide first-hand information on some of the environmental properties of the atmosphere of Venus. A sound of this type, although not designed to survive the ballistic impact on the planet's surface, should carry some kind of accelerometer to distinguish between solid and liquid surfaces. It is also desirable to include a method for determining the environmental measurements as a function of altitude. Methods to accomplish this could vary from a lightweight and simple three-axis accelerometer technique, where the capsule altitude would be interpretive as a function of the deceleration curve, to techniques using radar for precision capsule-altitude measurements.

If additional weight, power, and data capabilities are available, then it would also be desirable to incorporate an atmospheric aerosols detector or disdrometer. An instrument commercially available through Bausch and Lomb used for counting dust particles ranging in size from 0.3 to 10 μ at concentrations between 10^3 and 10^6 particles/ft^3 may be suitably modified for this usage.

A suggested capsule scientific payload is given in Table 2. This payload should consist of a thermodynamic variables package, which includes experiments to examine the density, temperature, pressure, and velocity of sound of the atmosphere; an atmospheric composition experiment; an impact accelerometer; a visual or ultraviolet photometer to determine the cloud layers and the scattering properties of the atmosphere; and a triaxial accelerometer. The total science payload weight is only about 17 lb.

References

1. Minovitch, M. A., *The Determination and Characteristics of Ballistic Interplanetary Trajectories Under the Influence of Multiple Planetary Attractions,* Technical Report No. 32-464, Jet Propulsion Laboratory, Pasadena, California, 1963.
2. Hunter, M. W., "Future Unmanned Exploration of the Solar System," *Astronautics and Aeronautics,* Vol. 2, No. 5, May 1964.
3. Cutting, E., and Sturms, F. M., *Trajectory Analysis of a 1970 Mission to Mercury Via a Close Encounter with Venus,* Interoffice Technical Memorandum No. 312-505, Jet Propulsion Laboratory, Pasadena, California, 1964.

UNCLASSIFIED